# Reconnection-driven Dynamics at Ganymede's Upstream Magnetosphere: 3D Global Hall MHD and MHD-EPIC Simulations

**Hongyang Zhou[1], Gábor Tóth[1], Xianzhe Jia[1], Yuxi Chen[1]**

[1]Department of Climate and Space Sciences and Engineering, University of Michigan, Ann Arbor, Michigan, USA

**Key Points:**

- Simulated flux rope of the length of Ganymede's radius forms at a rate of $\sim 2$/minute at the upstream magnetopause
- Ion and electron scale kinetic physics near the reconnection site are revealed with coupled kinetic model
- Developed general and robust method to measure global reconnection rate.





Corresponding author: Hongyang Zhou, hyzhou@umich.edu

**Abstract**

The largest moon in the solar system, Ganymede, is the only moon known to possess a strong intrinsic magnetic field and a corresponding magnetosphere. Using the latest version of Space Weather Modeling Framework (SWMF), we study the upstream plasma interactions and dynamics in this sub-Alfvénic system. Results from the Hall MHD and the coupled MHD with embedded Particle-in-Cell (MHD-EPIC) models are compared. We find that under steady upstream conditions, magnetopause reconnection occurs in a non-steady manner, and the energy partition between electrons and ions is different in the two models. Flux ropes of Ganymede's radius in length form on the magnetopause at a rate about 3/minute and create spatiotemporal variations in plasma and field properties. Upon reaching proper grid resolutions, the MHD-EPIC model can resolve both electron and ion kinetics at the magnetopause and show localized non-gyrotropic behavior inside the diffusion region. The estimated global reconnection rate from the models is about 80 kV with 60% efficiency, and there is weak evidence of $\sim 1$ minute periodicity in the temporal variations due to the dynamic reconnection process.

## 1 Introduction

The exploration of Ganymede's magnetosphere has made huge progress since the mid-1990s thanks to the Galileo mission. The Galileo spacecraft made six close flybys of Ganymede from 1995-2000 (G1, G2, G7, G8, G28 and G29) and discovered that Ganymede has a permanent magnetic moment (M. G. Kivelson et al., 1997). In addition to the intrinsic magnetic moment, Ganymede has an induced dipole magnetic field, the existence of which is connected with the variation of the Jovian magnetic field near the moon's orbit (M. G. Kivelson et al., 2002). The magnetic field at Ganymede and its interaction with the Jovian system forms a mini-magnetosphere around the moon. Given the sub-Alfvénic, sub-sonic Jovian upstream plasma flow at Ganymede's orbit, there is no bow shock but instead an Alfvén wing structure forms around the magnetopause.

Ganymede's mini-magnetosphere embedded inside Jupiter's large magnetosphere is an ideal system for comparative magnetospheric studies, especially for reconnection physics and its influence on the global system. The kinetic scales at which reconnection happens are relatively large compared to the size of the magnetosphere. For example, during Galileo G8 flyby the Jovian wind has a mass density $\approx 56\, m_p/\mathrm{cm}^{-3}$ consisting of a mixture of $O^+$ and $H^+$ ions with an average ion mass $M_i = 14\, m_p$, resulting in the ion inertial length $d_i = 0.16\, R_G$, where $R_G = 2634$ km is the mean radius of the moon (M. G. Kivelson et al., 2004). There may also be a substantial proportion of $S^{++}$ ions, but they have the same mass-to-charge ratio as the $O^+$ so it won't affect the ion gyro-radius. In comparison, the diameter of the magnetosphere is about $4\, R_G$ in the equatorial plane. In the past decades, tremendous effort and progress have been made. Even though there is no direct evidence of reconnection at Ganymede, the discovery of magnetosphere from magnetometer (MAG), Plasma Wave Subsystem (PWS) and Energetic Particles Detector (EPD) data (M. Kivelson et al., 1996; Gurnett et al., 1996; Williams et al., 1997) and the quasi-antiparallel Jovian magnetic field to the closed field lines with both ends connected to Ganymede's magnetic poles strongly suggest the existence of upstream magnetic reconnection. From observations, M. G. Kivelson et al. (1998, 2002) did a comprehensive analysis on the magnetometer data from multiple Galileo flybys. An unusually high global reconnection efficiency was estimated from the limited G2 flyby data.

Through numerical simulations, many of the reconnection related findings have been confirmed and well explained. Kopp and Ip (2002) presented the first 3D resistive MHD model for Ganymede's magnetosphere, and described how the magnetic field configuration of Ganymede's magnetosphere could change under different external plasma conditions. A different resistive MHD model was applied to Ganymede by Jia et al. (2008),

where they coupled, for the first time, the moon's interior to the global magnetosphere. Later they refined their MHD model by developing improved inner boundary conditions and incorporating an anomalous resistivity model that allows for simulating fast reconnection (Jia et al., 2009). The new model not only yields satisfactory agreement with the Galileo observations but also predicts that Ganymede's magnetopause reconnection occurs in a non-steady manner under fixed upstream conditions (Jia et al., 2010). Later, Dorelli et al. (2015) extended the MHD model to include Hall effect, which allows asymmetries and ion drifts inside the magnetosphere. Recently, Wang et al. (2018) have employed a 10-moment closure model for Ganymede with electron kinetics included, which is shown to have the potential of capturing local electron and ion kinetics within global magnetosphere simulations. The coupled fluid-kinetic model (Tóth et al., 2016; Zhou et al., 2019), which are the predecessors of the current model used in this study, embed a local kinetic Particle-in-Cell (PIC) region inside the global Hall MHD domain. This approach allows resolving potentially important kinetic process near the reconnection site, which is of great interest to magnetosphere study.

However, despite the great efforts and progress, there are still many unanswered questions:

1. What are the signatures of reconnection at Ganymede's magnetopause?
2. What are the properties of the flux transfer events (FTEs) at the upstream magnetopause?
3. How efficient is the upstream reconnection process quantitatively?
4. Are there any intrinsic periodicities in the interaction between Jovian plasma and Ganymede's magnetosphere?

We have attempted to answer the above questions using the latest coupled fluid-kinetic numerical simulation model. A brief overview and recent updates to the model are presented in section 2. The simulation results are described in section 3, followed by the discussion of our model results in section 4 and the summary in section 5.

## 2 Model Description

The simulations presented in this paper are performed with the Space Weather Modeling Framework (SWMF) (Tóth et al., 2012). Two models are used in this study: the Hall MHD (Tóth et al., 2008) model with electron pressure equation and the semi-implicit particle-in-cell kinetic model iPIC3D (Markidis et al., 2010; Chen & Toth, 2019). These two models are coupled together through SWMF and form the MHD-EPIC fluid-kinetic model (Daldorff et al., 2014) that has been successfully applied to Mercury (Chen et al., 2019), Earth (Chen et al., 2017), Mars (Ma et al., 2018), and Ganymede (Tóth et al., 2016; Zhou et al., 2019).

We run both time-dependent Hall MHD and MHD-EPIC simulations of Ganymede's magnetosphere using the same fixed upstream conditions in order to examine the differences and similarities in reconnection-driven dynamics as simulated by different global models. The models and setups, including the equation set, selection of upstream and inner boundary conditions and running procedures are described in detail by Zhou et al. (2019). In the present study we have used the latest version of the in-house iPIC3D model, which has been improved with better stability, energy and charge conservation, and particle splitting-merging algorithm, as been described by Chen and Toth (2019).

Since the main focus of this paper is the magnetopause reconnection, we have chosen to use a set of simulation parameters (including both the external and internal boundary conditions) that correspond to those of the Galileo G8 flyby, during which the spacecraft passed through the low-latitude, upstream magnetopause where reconnection is expected to be active. We set the upstream ion number density $n_i = 4\,\mathrm{cm}^{-3}$, plasma ve-

locity $V_x = 140$ km/s, magnetic field $\mathbf{B} = [-10, -6, -86]$ nT, and thermal pressure $P_i = 3.6$ nPa, $P_e = 0.2$ nPa. Both the Hall MHD and MHD-EPIC simulations have been run for a total duration of 20 minutes, which is several times the typical time it takes the ambient flow to pass the magnetosphere. The time-dependent Hall MHD simulation starts from the quasi-steady state solution and the time-dependent MHD-EPIC simulations start from $t = 300$s after the Hall MHD run. The time lag is chosen such that the solution has been fully settled into time-dependent Hall MHD that does not drastically change with time. The computational domain is defined in the GphiO coordinate system, where x is along the flow direction, y is along the Ganymede-Jupiter vector with positive direction pointing towards Jupiter, and z is along the spin axis. Compared with the previously published work (Zhou et al., 2019), we have further increased the grid resolution for both fluid and kinetic models. We doubled the resolution inside the magnetosphere to reach an average of $1/120R_G \sim 0.05d_i$ in the radial direction, 0.7° in the azimuthal direction and 0.35° in the polar direction for the stretched spherical MHD grid and $[1/64, 1/32, 1/64]R_G \sim [0.09, 0.19, 0.09]d_i$ for the Cartesian PIC grid. These result in a total number of 27 million cells in MHD and 2.5 million cells in PIC with 1.2 billion particles (256 particles per cell per species). The Hall MHD time-dependent run starts from the quasi-steady state after $80,000$ steps, and the PIC simulation starts after 300s of the Hall MHD run. The sharp transition period represented by the beginning $\sim 60s$ time in Hall MHD simulation is ignored in the analysis.

In order to resolve further to electron scales near the upstream magnetopause, we have performed another short-duration higher-resolution MHD-EPIC run with PIC grid size $[1/128, 1/64, 1/128]R_G \sim [0.05, 0.1, 0.05]d_i$. Given the proton-electron mass ratio of 100 used in the simulation, this corresponds to $\Delta x = \Delta y = 0.05d_i = 0.5d_e$, $\Delta y = 0.1d_i = d_e$ inside the PIC domain, with 2.4 billion particles for each species (125 particles/cell). Such high resolution in a global magnetosphere model requires significant computing resources: 1 second simulation in physical time requires 750 core hours running with 4480 cores on Intel Xeon Platinum 8280 computing nodes. Therefore we only run at this resolution for $\sim 100s$ physical time demonstrating the fully resolved electron and ion kinetics.

## 3 Results

The 20 min simulations cover the entire G8 flyby magnetosphere crossing. We start with comparing the magnetic field with Galileo observations, and then continue to demonstrate the magnetopause dynamics, diffusion region properties, and reconnection rate estimations.

### 3.1 Magnetic Field Comparison

Given that we have 20 min of simulation for both models with a 1s cadence output and the time between inbound/outbound magnetopause crossing by Galileo is about 10 min, we have identified the best fit to observations by shifting the starting time in the simulations. Figure 1 shows the magnetic field comparison with the G8 flyby close encounter observation (black) for Hall MHD (blue) and MHD-EPIC (orange). We align the simulation outputs from 15:45 ULT to 16:05 ULT, during which the magnetic field along the Galileo trajectory is extracted from different snapshots. The field data before 15:45 ULT and after 16:05 ULT are extracted from the first and last snapshot, respectively. Both models have in general nice agreements with the observation, even though we cannot fully reproduce the sharp transitions during the magnetopause crossings. With doubled grid resolution compared to our previous work (Zhou et al., 2019), small scale spatiotemporal perturbations start to show up. Hall MHD behaves more dynamic than the coupled MHD-EPIC model near the upstream reconnection regions. As have been shown in our previous study, the fluctuations during the inbound and outbound cross-

163 ings are related to the magnetopause surface motion as well as flux rope generation. These
164 will be discussed further in later sections. Note that the Galileo magnetometer data were
165 collected at a rate of 3 samples/s during the close flybys, which means that the pertur-
166 bations with frequencies between 0.5 and 1.5 Hz are missing from the simulation due to
167 the choice of 1s output cadence.

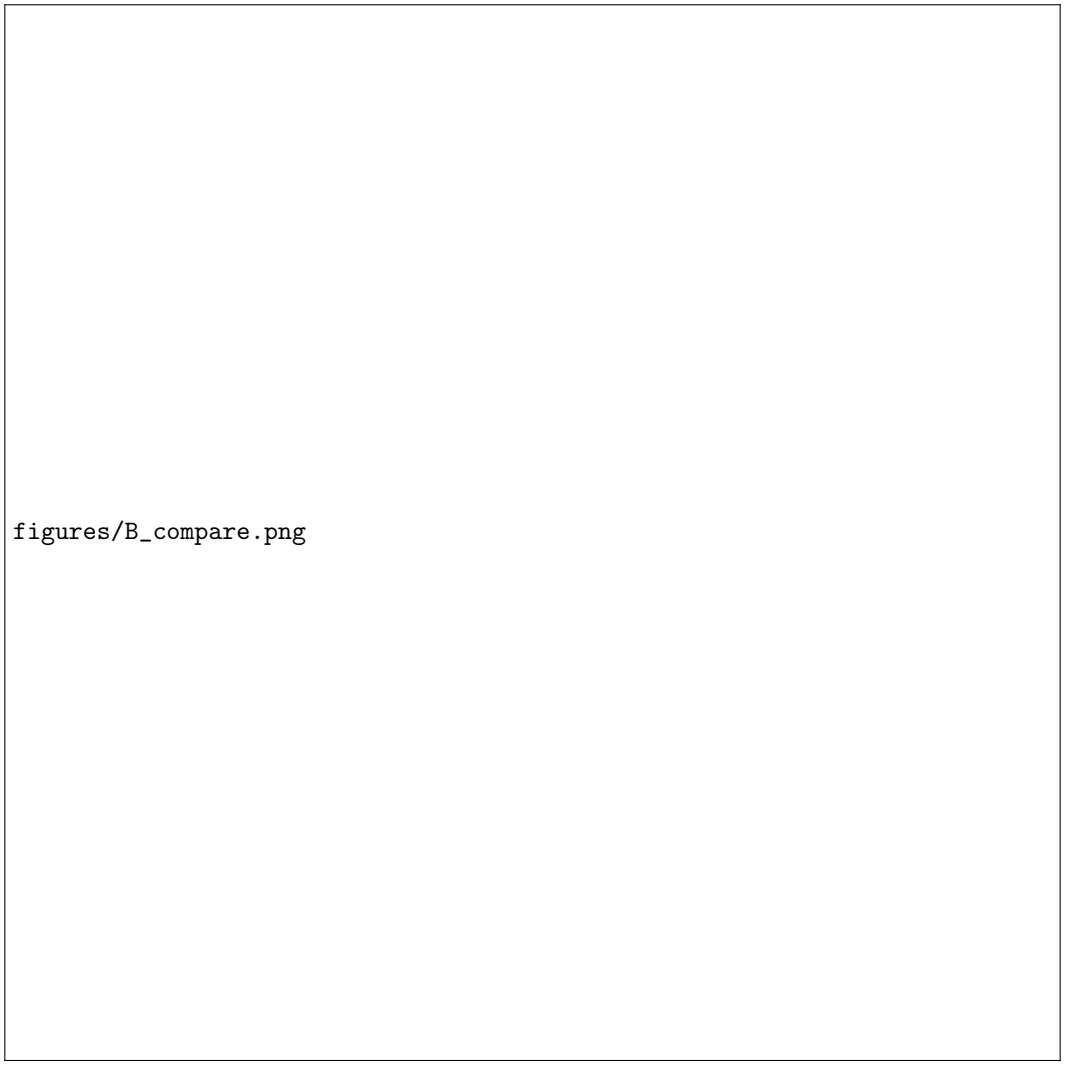


**Figure 1.** Magnetic field comparisons with Galileo observation during G8 flyby close encounter (black) for Hall MHD (blue) and MHD-EPIC (orange) simulations.

168 ### 3.2 Plasma Pressure and Total Current Density

169 Although Hall MHD and MHD-EPIC runs show many similarities, such as the quadrap-
170 olar $B_y$ magnetic field, we find certain quantities that are different especially around the
171 upstream magnetopause. We select one snapshot from each model where FTEs do not
172 exist and the reconnection X-line is roughly along the equator. Figure 2 shows the ion
173 and electron pressures in the meridional cut from the two models. While the total plasma
174 pressure is about the same, the energy partitions between ions and electrons are differ-
175 ent: the kinetic PIC model shows more heated electrons than the Hall MHD model near
176 the upstream magnetopause. The Hall MHD equations we solve (Zhou et al., 2019) do

not include physical terms for controling electron pressure except adiabatic heating, thus we have much cooler electrons near the magnetopause in the Hall MHD results.

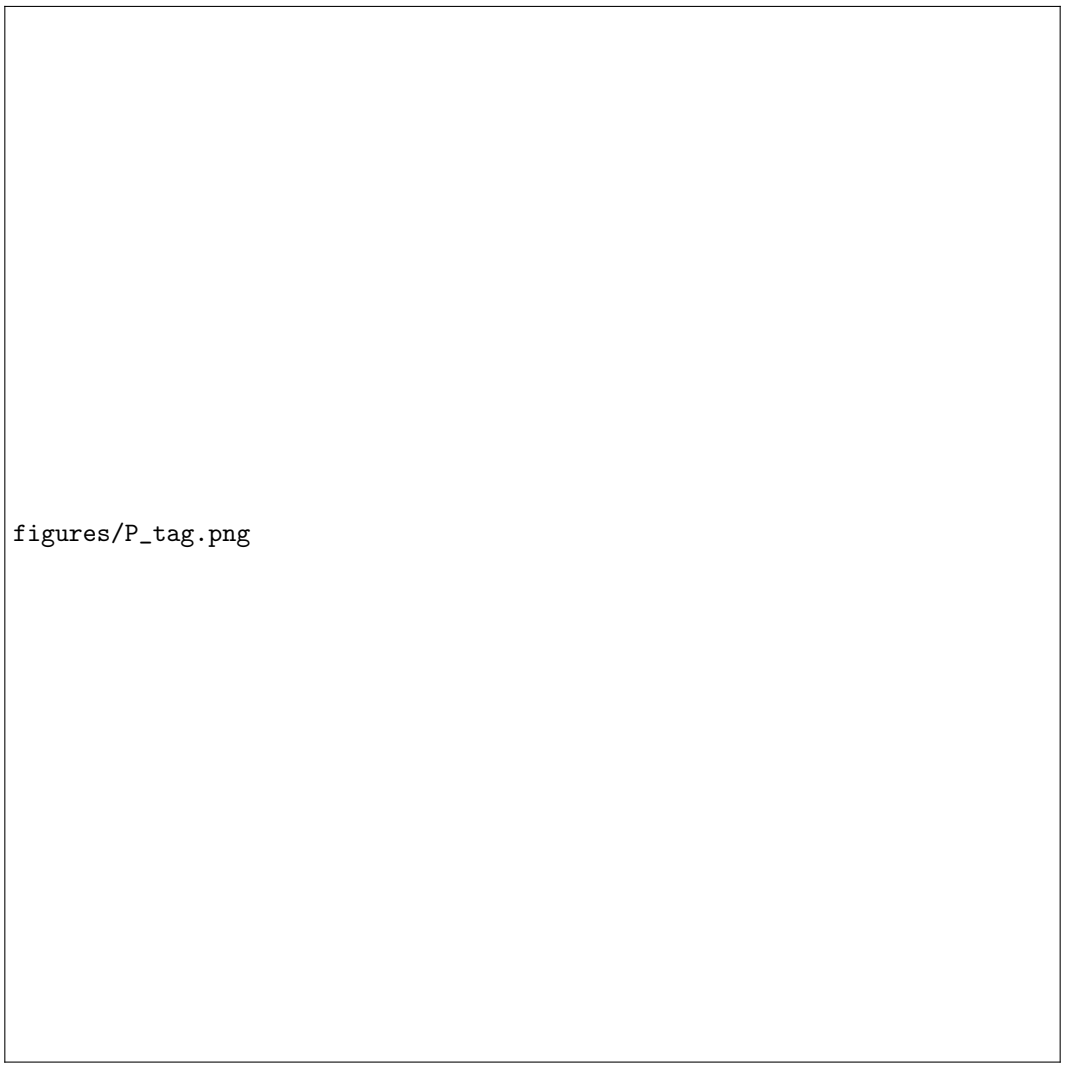


**Figure 2.** Ion and electron pressures in the meridional cut in (a,c) Hall MHD at $t = 595\,s$ and (b,d) MHD-EPIC at $t = 650\,s$.

Figure 3 shows the total current densities in the meridional and equatorial cuts from the two models. While the location, magnitude and general shape of the current sheet look similar, it is thicker in the Hall MHD than in the MHD-EPIC model. In the meridional cut Figure 3b, the current density near the reconnection site extends more in the z-direction. Note that in the tail reconnection site we only have Hall MHD, so it serves as a nice reference between the upstream and tail reconnection regions in the two models.

### 3.3 Magnetopause Dynamics and FTEs

The magnetopause motion can be directly visualized with the movies in the supporting materials made from 3D data outputs. Figure 4 shows selected frames from the movie where the magnetopause surface is defined approximately by the $B_z = 0$ isosur-

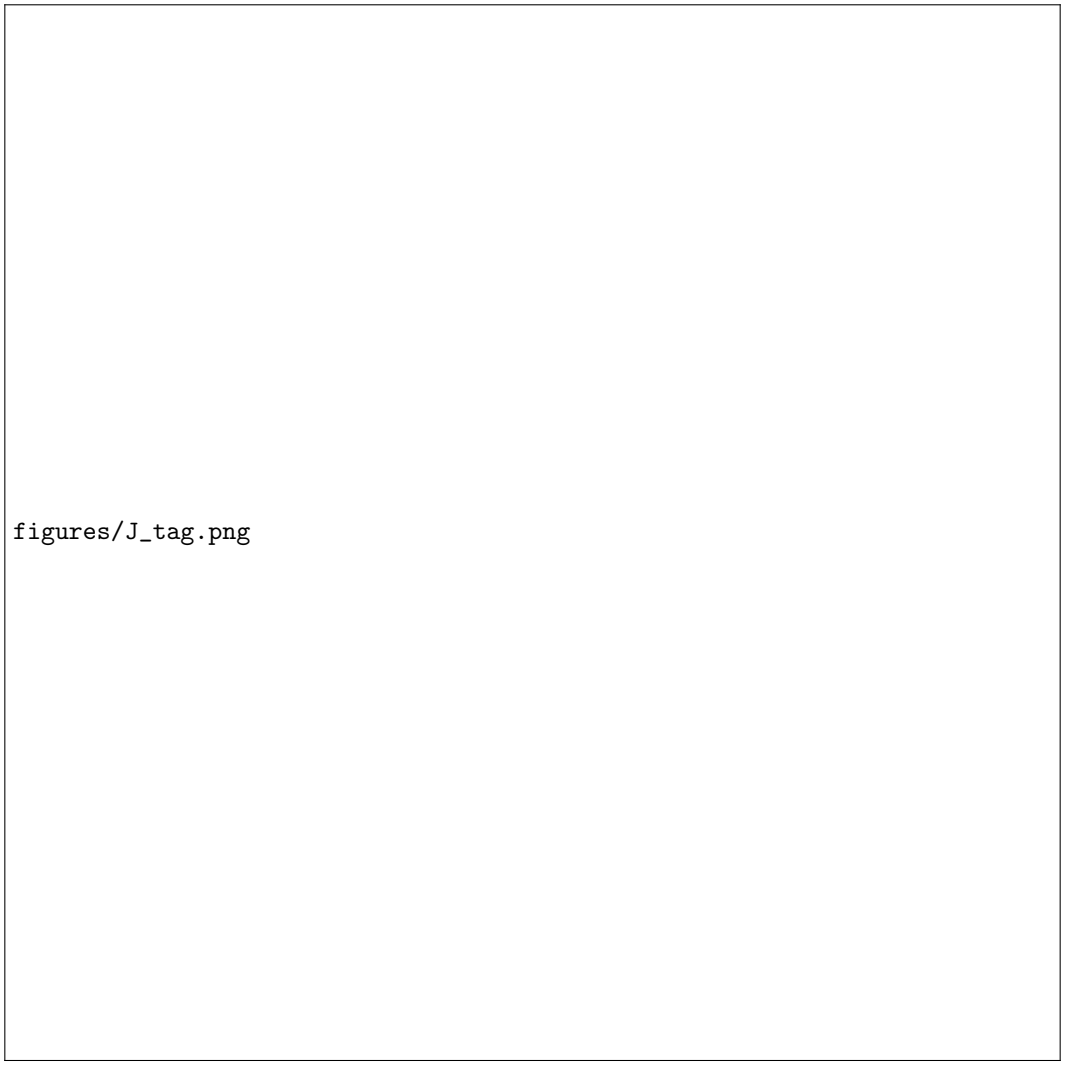


**Figure 3.** Total current density in the meridional and equatorial cut in (a,c) Hall MHD at $t = 595\,s$ and (b,d) MHD-EPIC at $t = 650\,s$.

face. Because of the small guide field $B_y$ during the G8 flyby, we find $B_z = 0$ is a good approximation for the magnetopause surface. We select one quasi-steady snapshot and one highly-perturbed snapshot with flux ropes from each model and convert the vectors into the local LMN coordinates, where N points normal to the magnetopause outward into the upstream, L lies along the projection of the dipole axis onto the magnetopause (positive northward), and M completes the triad by pointing towards sub-Jovian side. The colored contour of ion pressure and velocity component $u_L$ are displayed in the top and bottom rows, respectively.

The X-lines, shown by the white region where $u_L$ diverges around zero, extend along the M direction on the magnetopause. The formation of long X-lines in both models is consistent with the prediction of onset conditions over the majority of Ganymede's magnetopause from an analytical model (Kaweeyanun et al., 2020). Plasma bulk flow on the flanks, as shown by Figure 7 in (Zhou et al., 2019) for the G2 flyby, also suggests the extended reconnection sites across the upstream magnetopause. The intermittently generated flux ropes alter the long X-line near the equatorial plane and have high thermal

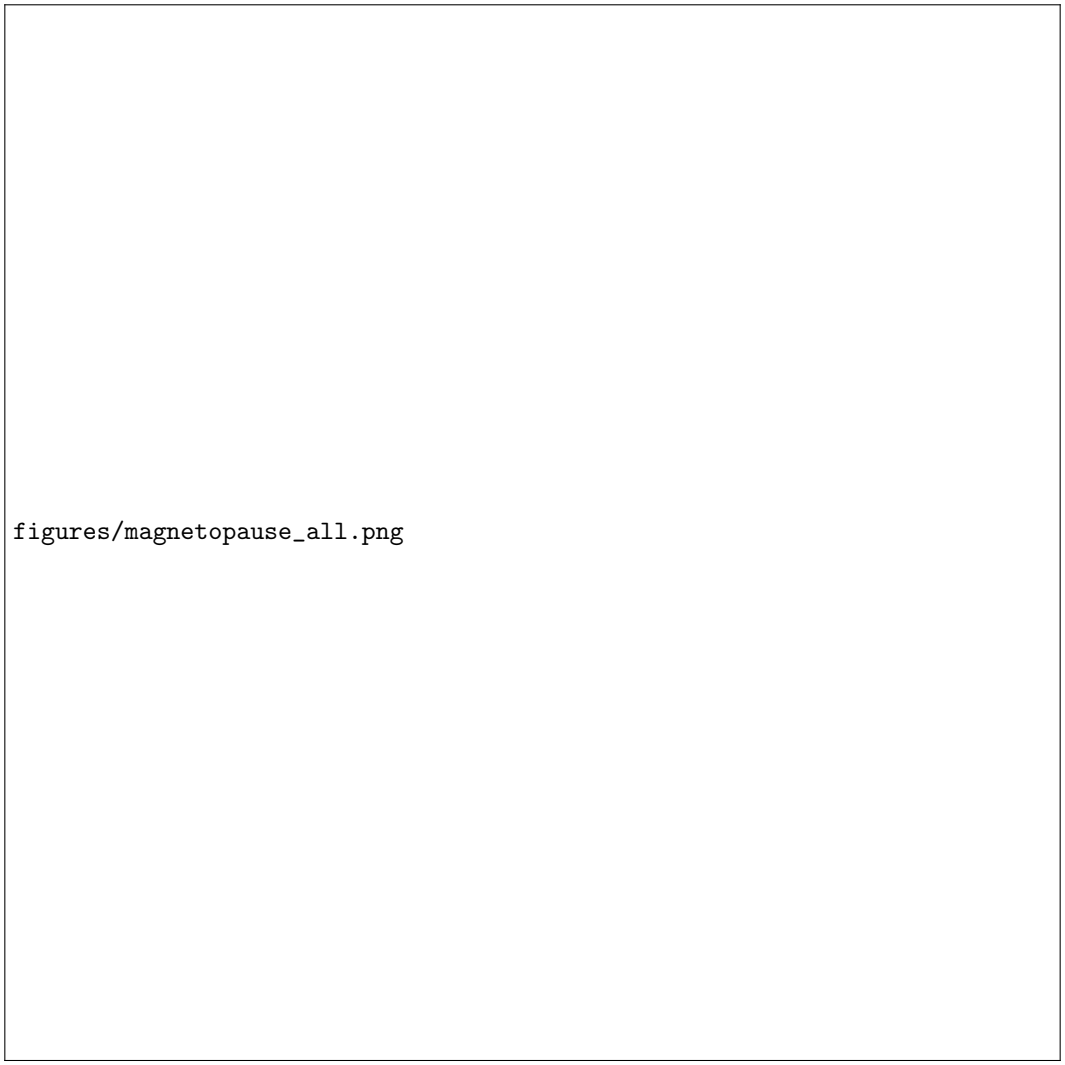


**Figure 4.** Magnetopause surface defined by $B_z = 0$ viewed from the upstream direction in (a) Hall MHD and (b) MHD-EPIC simulations. For each model, the plasma pressure is shown in the first row, and the plasma velocity $u_L$ component in the local LMN coordinates is shown in the second row. The quasi-steady snapshots are shown on the left, and the snapshots with large flux ropes are shown on the right.

pressure inside the core regions. At a later stage when large flux ropes are well developed, an enhancement of the core field $B_y$ is observed (Figure 5), and the high thermal pressure persists in the core region. However, we note that from the simulations core fields are not always present in the identified flux ropes. This suggests that the classical force-free model can only explain part of the flux ropes being observed from simulations.

There is a more dynamic magnetopause surface in the Hall MHD simulation with larger magnitudes of plasma pressure and outflow velocity than in the MHD-EPIC simulation. The dark dip on the $B_z = 0$ illuminated contour surface along the velocity stagnation region in the Hall MHD does not show up in the MHD-EPIC simulations. Figure 3a-b in the meridional cut show that the X-line is thicker in Hall MHD results and there is a relatively sharp dip near the center. Thus this visual effect is related to the instrinsic differences of the X-line resolved by MHD and PIC. Full animations for the

20 min runs can be seen in the supplementary materials. In Ganymede's G8 flyby simulations with constant Jovian upstream driving, we consistently observe magnetopause motion as well as flux rope generation in an intermittent manner. This suggests that there's no truly steady state in Ganymede's sub-Alfvénic magnetospheric plasma interaction.

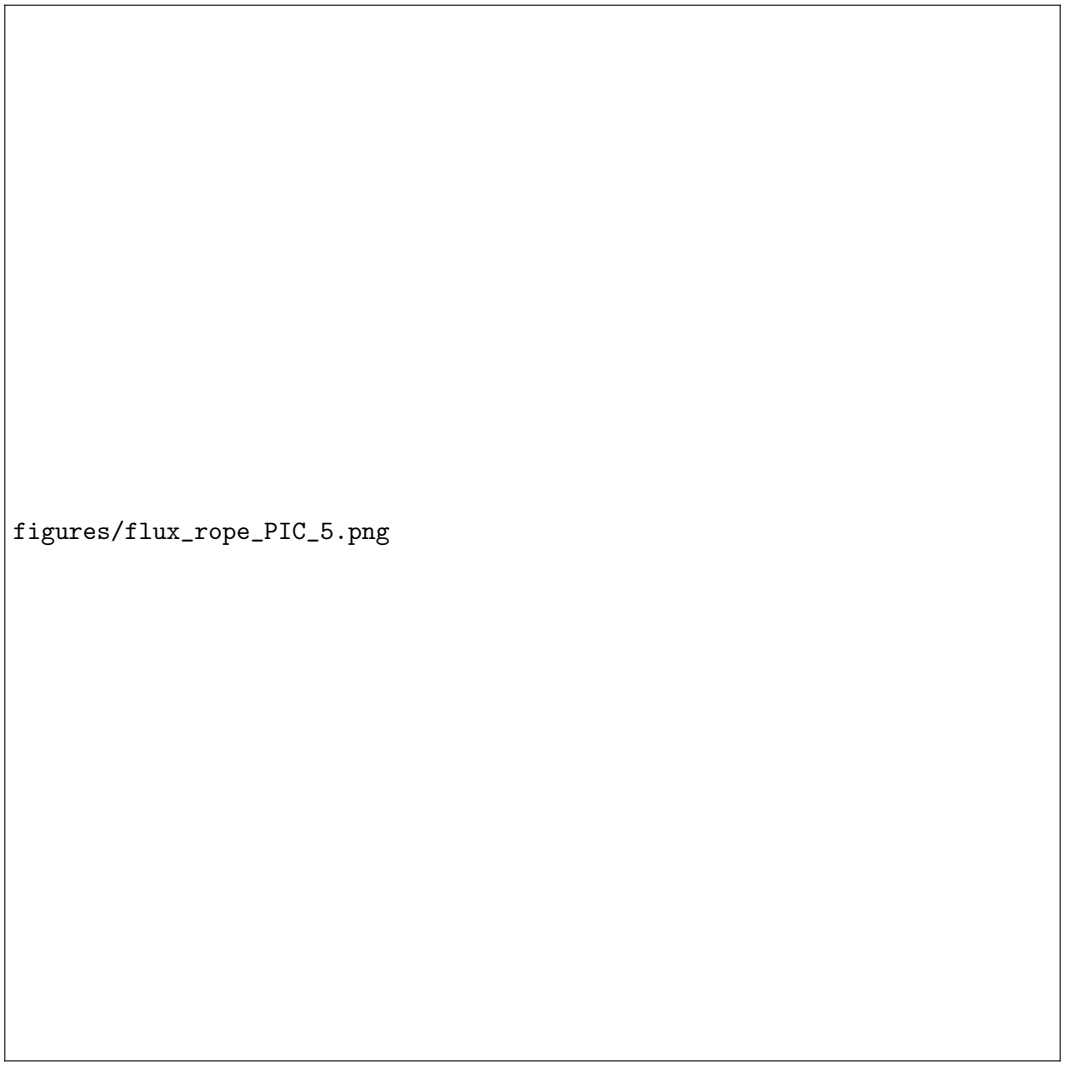


**Figure 5.** Example of well developed flux rope from MHD-EPIC simulation. The $B_y$ colored contours in units of nT are shown in $z = 0.1R_G$ and $y = 0R_G$ cut planes. A core field is clearly present at the center.

By selecting a series of static satellites located on the average positions of the magnetopause, we are able to quantitatively characterize the generation of flux ropes from simulations. First we extract the average $B_z = 0$ locations on the meridional and equatorial plane from the simulation runs, which form two curved lines along the center of the magnetopause. Then we interpolate the states onto these fixed locations over the simulation times. The thermal pressure perturbations with respect to the average pressure over a $\pm 100$ s sliding window are shown as a function of spatial location and simulation time in Figure 6. A tilted red strip in the contour plots corresponds to a flux rope with increased thermal pressure in the core region moving across the meridional (a,b) and equatorial plane plane (c,d). Negative slopes in (a,b) represent downward propagating flux

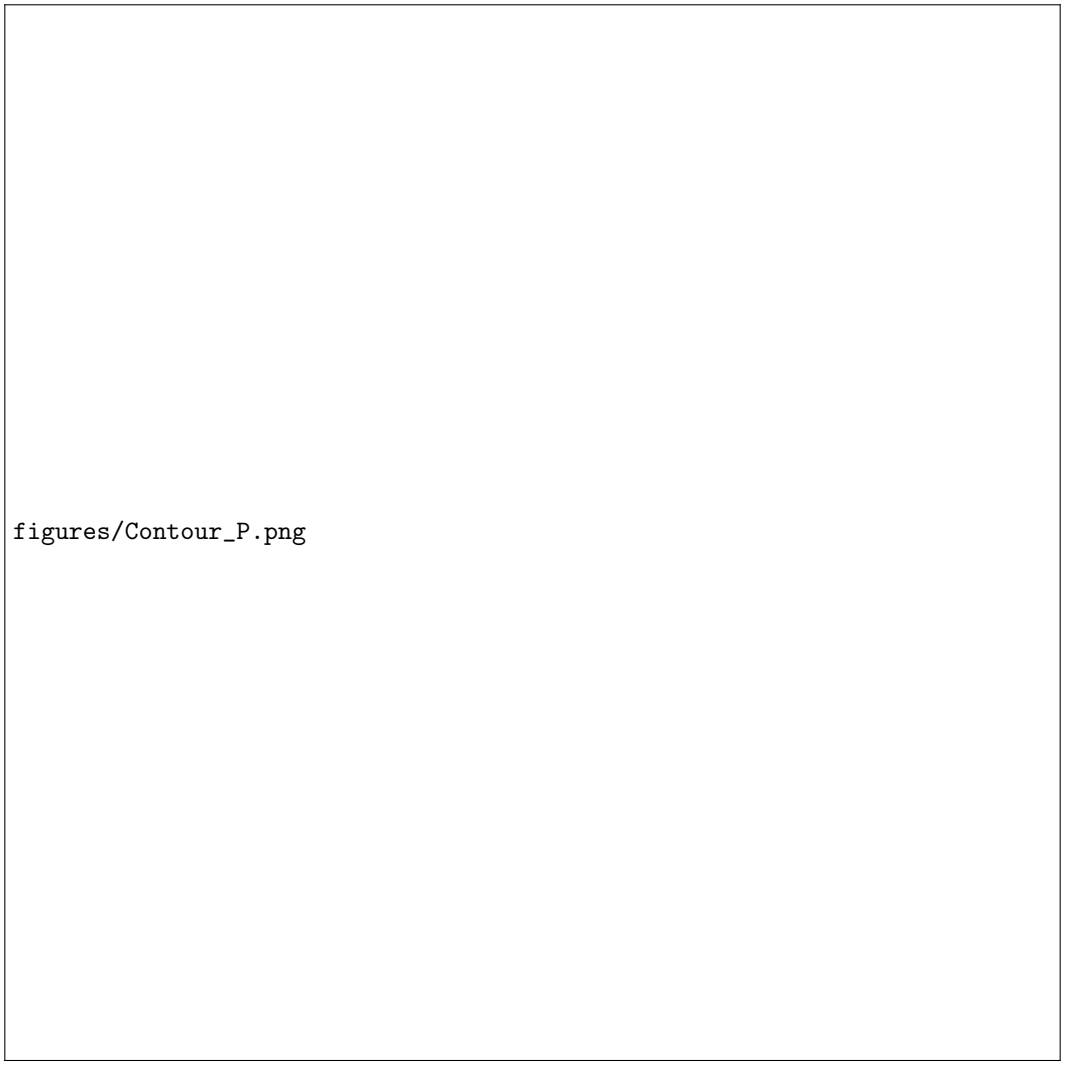


**Figure 6.** Motion of thermal pressure perturbations along the intersection lines of the magnetopause (defined as $B_z = 0$) and the meridional (a and b panels) or equatorial planes (c and d). The colors show the pressure perturbation relative to the mean pressure taken over a sliding $\pm 100\,\mathrm{s}$ interval. Panels (a) and (c) show Hall MHD results, while (b) and (d) are from MHD-EPIC. The gray and black + sign represent identified FTEs at $z = \pm 0.5\,R_G$, respectively.

ropes and positive slopes represent upward propagating flux ropes on the magnetopause. The upper right part of (b) is zoomed in to show the positive slopes. There is no clear asymmetry in the initial location or propagation direction.

We have checked that there is a one-to-one correspondence between a flux rope generated on the magnetopause (as can be seen from the movies) and a bright red strip in Figure 6. For example, the largest FTE in the Hall MHD and MHD-EPIC simulations happen at $\sim 700$s and $\sim 400$s, respectively, each corresponding to the brightest strips in Figure 6. Estimation on the slopes shows that the flux ropes in both Hall MHD and MHD-EPIC move at roughly the upstream Alfvén velocity $V_{A0} = 253\,\mathrm{km/s}$ along the L direction on the magnetopause, consistent with theoretical expectation.

In the meridional cuts, we pick the total plasma pressure perturbations 1 standard deviation larger than the mean value at that location, and set it as the criterion for identifying an FTE. If there are multiple pressure peaks exceeding this threshold within a 10s duration, only one FTE is counted. These thresholds are somewhat ad hoc due the the lack of a precise definition of FTEs. The identifications are shown with plus signs in Figure 6a-b at $z = -0.5R_G$ (black) and $z = 0.5R_G$ (gray). We find 73 and 51 FTEs from Hall MHD and MHD-EPIC simulations, respectively, which gives an average occurrence rate of $\sim 3$ FTEs per minute. Note that by counting FTEs in this way, we may miss those that never pass through the meridional cut. However, this is still a reasonable estimation given that most flux ropes initiate from the low latitude region, extend in the y direction, and move in the z direction.

From the equatorial cuts in Figure 6c-d, the average length of the flux ropes is about $0.8R_G$ in the y direction, which corresponds to roughly $1R_G$ in total length considering the curvature of the magnetopause in the x-y plane. Additionally, many of the flux ropes have one side tilted towards higher latitudes (e.g. Figure 5), so the average length may be even larger.

### 3.4 Kinetic Signatures near the Diffusion Region

With the embedded PIC model using grid resolution comparable to the electron skin depth, we are able to obtain detailed information about electrons and ions directly by looking at kinetic particles and their velocity distributions near the reconnection sites. At low latitudes in the GPhiO Cartesian coordinates during the G8 flyby with dominantly north-south magnetic field, the LMN coordinate system of a reconnection site is approximately aligned with the GPhiO system. Therefore, approximately $u_x \sim u_N$ is the inflow velocity, $u_z \sim u_L$ is the outflow velocity, and $u_y \sim u_M$ is the out-of-plane velocity. Note that the positive x direction in the GPhiO coordinate system is pointing toward the moon, which is the opposite of that in the GSE coordinate system.

Figure 7 shows one snapshot from the highest resolution simulation in the meridional plane near the reconnection site for the magnetic and electric fields, electron and ion bulk velocities, current density, plasma density, and different measures of the violation of the ion and electron frozen-in conditions. Magnetic field, particle number densities and velocities are normalized to the upstream field strength $B_0 = 86.8$ nT, number density $n_0 = 4$ cm$^{-3}$ and Alfvén velocity $V_{A0} = 253$ km/s, respectively. Electric field is normalized to $E_0 = V_{A0}B_0 = 22$ mV/m, and current densities are normalized to $J_0 = en_0V_{A0} = 0.16\,\mu A/m^2$. The quadrupolar out-of-plane magnetic field $B_y$ in Figure 7b extends from the electron diffusion region, and the Hall electric field $E_x$ in Figure 7c shows strong peaks along the separatrices. Ions are accelerated to $\sim V_{A0}$ in the exhaust region, with a drift in the -y direction (Figure 7d-e) peaked on the magnetospheric side and small counter streaming portion on the Jovian side. Electrons move into the diffusion region around the X-line and are accelerated to $\sim 5V_{A0}$ (the electron/ion mass ratio in the PIC model is 100) in the outflow region, with a large drift in the +y direction (Figure 7f-h). Figure 7f shows the non-colocation of X-line center (along the dotted line) and flow stagnation point (indicated by the white color), where the latter is on the magnetospheric side of the X-line (Cassak & Shay, 2007).

#### *3.4.1 Violations of Frozen-in Condition*

Figure 7m-p show the x and y components of $\mathbf{E} + \mathbf{V} \times \mathbf{B}$ for ions and electrons, respectively. These represent the violation of the frozen-in condition, or in other words, the deviation of the model from ideal MHD and Hall MHD, respectively. No clear signatures can be identified solely for the diffusion region, although the x component of $\mathbf{E}+\mathbf{V}_e \times \mathbf{B}$ show dipolar peaks near the center.

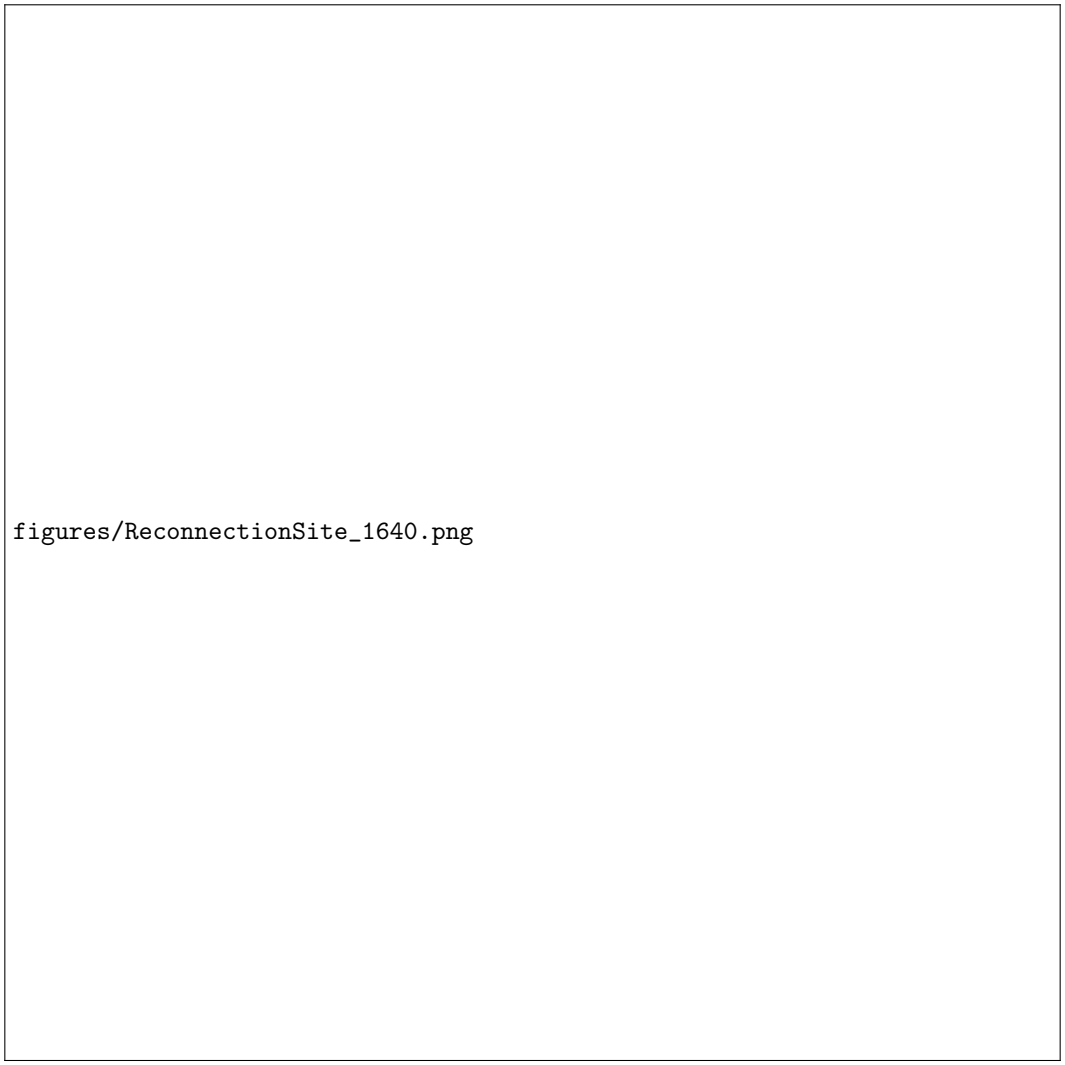


**Figure 7.** Normalized quantities in meridional plane from MHD-EPIC G8 flyby simulation near the reconnection site. $A\emptyset, D_{ng}, Q$ are three non-gyrotropy measures (Scudder & Daughton, 2008; Aunai et al., 2013; Swisdak, 2016) and $D_e$ is a dissipation measure (Zenitani et al., 2011). Solid black lines are the mapped magnetic field and dotted lines show the locations where $B_z = 0$. Values with signs are colored with red-white-blue colormaps centered at 0.

#### *3.4.2 Non-gyrotropy Measures*

Three different scalar non-gyrotropy measures $A\emptyset, D_{ng}$, and $Q$ (Scudder & Daughton, 2008; Aunai et al., 2013; Swisdak, 2016) for electrons are shown in Figure 7q-s. The frame-independent diagnostic formulas are given in Appendix A. $A\emptyset$ shows the non-gyrotropy in the plane perpendicular to the magnetic field, which peaks at the electron diffusion region and gets enhanced along the separatrices, especially on the magnetospheric side. It behaves similarly to the later proposed $\sqrt{Q}$ which is based on the property of positive semi-definite matrix and takes the full pressure tensor into account. The other non-gyrotropy measure $D_{ng}$, which scales with the ratio between the Frobenius norm of the non-diagonal terms and the trace of the pressure tensor, peaks near the X-line along the separatrices but is not localized at the central electron diffusion region. As with the math-

ematical counter examples proposed in (Swisdak, 2016), we also found that $\sqrt{Q}$ is more accurate in describing the non-gyrotropy effect near the reconnection site.

### *3.4.3 Dissipation Measure*

Finally, a frame independent dissipation measure derived from energy conversion $D_e = \mathbf{J}' \cdot \mathbf{E}' = \mathbf{J} \cdot (\mathbf{E} + \mathbf{V}_e \times \mathbf{B}) - (n_i - n_e)\mathbf{V}_e \cdot \mathbf{E}$ (Zenitani et al., 2011) is shown in Figure 7t. $D_e$ peaks at the reconnection site, and is also enhanced along the separatrices.

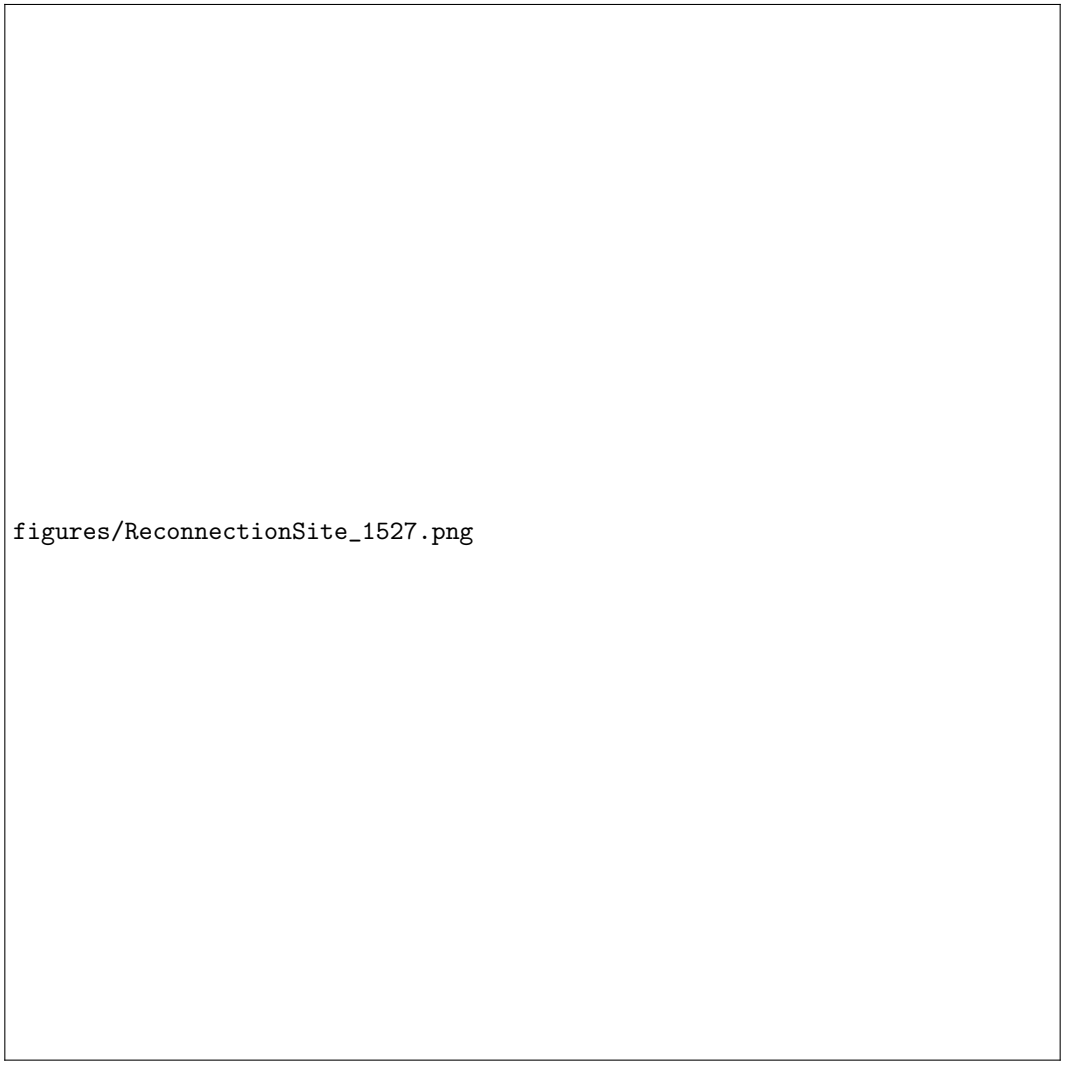


**Figure 8.** Same quantities as in Figure 7, but at a time when a flux rope is present in the MHD-EPIC simulation.

### *3.4.4 Reconnection Site with a Flux Rope*

It is interesting to see how these quantities look like near a flux rope formed between two reconnection sites. A snapshot with a flux rope is shown in Figure 8. The original X-line is near $z = 0.25R_G$, and the subsequently formed one is near $z = -0.35R_G$. Inside the flux rope, we observe an increase of normal electric field $E_x$ on the Jovian side, oppositely drifting ions in Figure 8d-e, perturbations of electron velocities in Figure 8f-

h, enhancement of density in Figure 8i, and the expansion of core current $J_y$ in Figure 8k. The ion outflow in the z direction from the new X-line encounters the stronger outflow in negative z direction from the original X-line, thus turns into a drift in the y direction. The non-gyrotropy measures (Figure 8q-s) decreases inside the flux rope, but the diffusion measure (Figure 8r) gets enhanced.

During the simulation, flux ropes inside the exhaust region do not always show all the corresponding kinetic signatures in the meridional cut: we have seen snapshots (not shown) of small flux ropes with little influence of ion outflow velocity and currents. In general, none of the presented quantities can uniquely identify the electron diffusion region, even though some measures perform better than others. The presence of flux ropes makes the detection even more complicated, both in observations and simulations. As suggested by Shay et al. (2016), one should rely on complementary approaches for identification.

#### *3.4.5 Phase Space Distributions*

The selected electron and ion phase space distribution functions (boxes 1-4 for electrons, boxes 5-8 for ions) around the reconnection site (at the same simulation time as in Figure 7) are plotted in Figure 9. For electrons, the sampled box regions have a width of $0.005R_G \sim 0.3d_e$ in the x direction and $0.04R_G \sim 2.6d_e$ in the z direction; for ions, the sampled box regions have a width of $0.01R_G \sim 0.064d_i$ in the x direction and $0.04\,R_G \sim 0.3d_i$ in the z direction. In the y direction all the boxes extend from $-0.08\,R_G$ to $0.08\,R_G$. In the electron diffusion region, the crescent shape distributions can be observed close to the peak location of $E_x$ and $B_z = 0$ midplane, which is referred to as the "shoulder" region by Shay et al. (2016). Moving farther away from the X-line (Box 2-3), the electrons coming from the Jovian side get further accelerated by $E_x$, which creates the clear gap from the magnetospheric electrons. We can observe a shift of the stagnation point towards the magnetospheric side, consistent with Figure 7f. In Box 4 at about $2.2d_e$ away from the X-line center, the penetration of electrons from Jovian upstream into the Ganymede's magnetosphere nearly vanishes.

For ions, in boxes 5 and 6 along the separatrices near the exhaust region, the $u_y - u_z$ velocity distribution cuts are nearly symmetric. In similar regions of Earth-like simulations (Broll et al., 2017) and observations (Smith & Rodgers, 1991), the so-called "D-shaped" ion distributions have been found. However, no clear signatures of ion "D-shaped" distribution is found here in our simulation. On the upstream side (box 7), the majority of ions are moving towards the X-line with positive $u_x$, but there are also reflected ions with negative $u_x$. On the magnetospheric side, ion crescent shape distributions can be found in a wide region $\sim 1d_i$ away from the X-line center (e.g. box 8).

The series of distribution functions can give us an estimation of the size of diffusion regions in reality, using the fact that electron isotropy breaks inside the electron diffusion region. Note that the proton-electron mass ratio is set to 100 in the simulations, therefore we need to convert the length in the simulations back to the real physical units. Along the center cut through the X-line in the x direction, the distributions become isotropic at about $1.5d_e$ and $2.5d_e$ away from the center on the Jovian upstream side and magnetospheric side, respectively. From Figure 7, the diffusion region extension in the z direction is about $0.1R_G \sim 6d_e$ in the simulation. As a result, the actual upstream electron diffusion region in nature is about $4\,d_e \sim 11$ km wide in x and $6\,d_e \sim 16$ km wide in z.

The results here have many similar features as in the asymmetric local 2D explicit PIC simulation with grid resolution 20 cells per $d_i$ and 4 cells per $d_e$ by Shay et al. (2016). In the normalized unit length, the ion resolutions in these two simulations are the same and the electron resolutions in MHD-EPIC is half of that in the local 2D PIC simulation. We note that in the implicit PIC simulation $\sim 2$ cells per $d_e$ is the minimum re-

quirement to accurately resolve electron kinetic signatures, and the coupled MHD-EPIC model has the capability of capturing both local ion and electron kinetic physics in a global magnetosphere simulation with adequate resolution. However, one must be cautious in comparing the results with the local PIC simulation. The key differences are: (1) in the Ganymede simulations we are adopting upstream magnetic fields with all three components and measured tilted dipole field, compared with an idealized, pure $B_z$ setup in the local PIC simulation; (2) our Ganymede simulations do not show a large density jump across the magnetopause (Figure 7i), and there is a large electron drift along the M (approximately y) direction due to the curvature of **B** and the Hall effect (Zhou et al., 2019). In Shay et al. (2016), the density between the sheath and magnetosphere differs by a factor of 10.

### 3.5 Reconnection Efficiency

In order to understand the global effects of magnetopause reconnection in this sub-Alfvénic system and compare the predictions between two different global models that contain different approximations of physics, we need to come up with a quantitative description of the reconnection rate and efficiency. One approach is to calculate the global reconnection efficiency defined by the ratio of the imposed electric field integral on the magnetopause to the full possible convective electric field integral across the width of the magnetosphere. Physically, this quantity represents how much magnetic flux get passed into the magnetosphere through upstream reconnection. M. G. Kivelson et al. (1997) first applied this idea to the G2 flyby observation and found an upper limit of nearly 100% reconnection efficiency, indicating a highly efficient reconnection process. Hu et al. (2007) described in detail about various methods of computing the electric field integral, or total reconnection rate, in global MHD simulations. As pointed out in their estimation, the convectional electric field dominates in the upstream half of the equatorial plane, whereas the interplanetary magnetic field lines nearby the upstream half of the reconnection layer are almost equipotential.

In a time-varying dynamical reconnection system with intermittent FTEs, it is very difficult to get all the local reconnection sites at the right locations and do the electric field integral in a proper manner. We pursue a different approach based on the fact that the upstream reconnection corresponds to a topological change: an open magnetic field line with both ends connected to the Jovian field and a fully-closed field line connected to Ganymede at both ends reconnect into half-open field lines connected to Ganymede at one end. We can measure total reconnection rate as the change in the total half-open magnetic flux. For the Jovian field aligned approximately with the Z direction, taking a plane at $Z = 2\,R_G$, for example, will cut through all the open field lines on the northern hemisphere as shown in Figure 10. Figure 10a shows the 3D view of the field lines that connects to the upstream and tail reconnection regions in red and green, respectively. Figure 10b shows the field line topology on the slice, with $B_z$ contours representing the sampled magnetosphere region, red line representing the upstream boundary $U$ and blue line representing the middle cut $M$ that closes the surface $A$.

The Leibniz integral rule for a two dimensional surface moving in three dimensional space is (Flanders, 1973):

$$\frac{d}{dt}\iint_{A(t)} \mathbf{F}(\mathbf{r},t)\cdot d\mathbf{A} = \iint_{A(t)} \left(\frac{\partial}{\partial t}\mathbf{F}(\mathbf{r},t) + \left[\nabla\cdot\mathbf{F}(\mathbf{r},t)\right]\mathbf{v}_A\right)\cdot d\mathbf{A} - \oint_{\partial A(t)} \left[\mathbf{v}_A\times\mathbf{F}(\mathbf{r},t)\right]\cdot d\mathbf{l}, \tag{1}$$

where

$\mathbf{F}(\mathbf{r},t)$ is a vector field at the spatial position $\mathbf{r}$ at time t,
$A$ is a surface bounded by the closed curve $\partial A$,
$d\mathbf{A}$ is a vector element of the surface $A$,
$d\mathbf{l}$ is a vector element of the curve $\partial A$,
$\mathbf{v}_A$ is the velocity of movement of the region $A$.

In our case, the vector field $\mathbf{F}$ is the magnetic field $\mathbf{B}$. Due to the divergence-free property of $\mathbf{B}$, we have

$$\frac{d}{dt}\iint_{A(t)} \mathbf{B}(\mathbf{r},t)\cdot d\mathbf{A} = \iint_{A(t)} \frac{\partial}{\partial t}\mathbf{B}(\mathbf{r},t)\cdot d\mathbf{A} - \oint_{\partial A(t)} \mathbf{v}_A \times \mathbf{B}(\mathbf{r},t)\cdot d\mathbf{l} \tag{2}$$

The time derivative of magnetic field can be expressed as the curl of electric field from Faraday's law of induction:

$$\frac{\partial \mathbf{B}}{\partial t} = -\nabla \times \mathbf{E} \tag{3}$$

With the help of Stokes' theorem, Equation 2 can be written as

$$\begin{aligned}\frac{d}{dt}\iint_{A(t)} \mathbf{B}(\mathbf{r},t)\cdot d\mathbf{A} &= -\iint_{A(t)} \nabla \times \mathbf{E}(\mathbf{r},t)\cdot d\mathbf{A} - \oint_{\partial A(t)} \mathbf{v}_A \times \mathbf{B}(\mathbf{r},t)\cdot d\mathbf{l} \\ &= \oint_{\partial A(t)} -\left[\mathbf{E} + \mathbf{v}_A \times \mathbf{B}\right]\cdot d\mathbf{l}\end{aligned} \tag{4}$$

Therefore, the time derivative of the magnetic flux passing through a closed surface equals the opposite of the electric field integral along the boundary *in the comoving frame of the boundary curve*. As shown in Figure 10b, the upstream reconnection corresponds to the flux passing through the boundary $U$ on the left where the velocity points inward to the surface. As it is difficult to accurately estimate the motion of the boundary, we replace the integral of the electric field along the moving boundary with the mathematically equivalent time derivative of magnetic flux plus the electric field integral along the rest of the boundary curve $M$ where the flow points to the +x direction and can be regarded as stationary by choosing a fixed line enclosing the surface $A$. We note that the results don't depend on the choice of $M$ as long as the flow points outward of surface $A$ along it.

With $\partial A = U + M$, Equation 4 can be rearranged to get the total upstream reconnection rate as

$$R_t \equiv \int_U \left[\mathbf{E} + \mathbf{v}_A \times \mathbf{B}\right]\cdot d\mathbf{l} = -\frac{d}{dt}\iint_{A(t)} \mathbf{B}(\mathbf{r},t)\cdot d\mathbf{A} - \int_M \left[\mathbf{E} + \mathbf{v}_A \times \mathbf{B}\right]\cdot d\mathbf{l} \tag{5}$$

Since the middle line is stationary, $\mathbf{v}_M \equiv 0$. In Hall MHD, electric field can be expressed as

$$\mathbf{E} = -\mathbf{V}_e \times \mathbf{B}, \tag{6}$$

where $\mathbf{V}_e$ is the electron bulk velocity. Therefore we have

$$\begin{aligned}R_t &= -\frac{d}{dt}\iint_{A(t)} \mathbf{B}(\mathbf{r},t)\cdot d\mathbf{A} - \int_M \mathbf{E}\cdot d\mathbf{l} \\ &= -\frac{d}{dt}\iint_{A(t)} \mathbf{B}(\mathbf{r},t)\cdot d\mathbf{A} + \int_M \mathbf{V}_e \times \mathbf{B}\cdot d\mathbf{l}\end{aligned} \tag{7}$$

We thus calculate the upstream reconnection rate by computing the two terms on the right-hand-side of Equation 7 numerically. We cut a slice plane at $z = 2R_G$, trace the field lines that pass through the plane, and find the half-open field line boundary curve on the slice. The surface integral of $A$ and the line integral along $M$ are evaluated from the magnetic field and electron velocity interpolated to the fine grid. The time derivative of the flux is taken with simple finite differencing of the surface integrals at a 1s cadence. The middle line is picked at $x = 1.28\,R_G$, where its length is the largest along y, so the flow points inward along $U$ and outward along $M$.

The width of the magnetosphere $L$ is taken as the extent of the closed field line region parallel to the external convective electric field $-\mathbf{V}\times\mathbf{B}$. For the Jovian field $B$ approximately parallel to $Z$ axis, the width can be taken as $L \approx 4\,R_G$ in the $Y$ direction

and the upstream electric field integral $\Delta V = |V_x B_z| L \approx 130$ kV. The global reconnection efficiency $\epsilon$ is then given by

$$\epsilon = R_t / \Delta V \tag{8}$$

The results are shown in Figure 11a-b for Hall MHD and MHD-EPIC simulations respectively. Regardless of the intrinsic differences between the two models, both give roughly $R_t = 83\,\mathrm{kV}$ or equivalently $\epsilon \approx 0.64$. This indicates about 60% of the plasma flowing onto Ganymede's magnetosphere crosses the magnetopause, which is quite efficient.

To identify if there is any connection between the FTEs and reconnection efficiency, we checked the correlation between FTEs occurrence time and changes of $\epsilon$. Because the field line tracing is done for each snapshot, the field line connectivity and the corresponding change of the open magnetic flux are passed from the upstream reconnection sites to the magnetic flux enclosed by the open-closed boundary curve in the $z = 2\,R_G$ plane immediately. The red and green dashed lines in Figure 11a-b represent the identified occurrence times from Figure 6 for FTEs with total plasma pressure perturbation larger than 1.5 standard deviation moving northward and southward, respectively. The majority of lines coincide with the local peaks of $\epsilon$, suggesting an increase of reconnection efficiency during the FTEs and a decrease of efficiency afterwards. However, we also found that even without relatively large FTEs (e.g. between $t = 700\,s$ and $t = 950\,s$), the reconnection rate is still fluctuating. Therefore we cannot confirm that the perturbation in upstream reconnection rate is purely related to FTEs.

For the sake of diagnosing if there are any periodicities related to the reconnection, we performed FFTs on the reconnection rates from the two models. The results are shown in Figure 11c. In general, the FFT spectra of the estimated reconnection rates from both models do not show any dominant periodicity, although there are multiple, relatively weak peaks around the 1 minute period (for Hall MHD, peaks at 26 s, 40 s, 55 s, 72 s and 110 s; for MHD-EPIC, peaks at 29 s and 57 s).

## 4 Discussion

Recently Carnielli et al. (2019, 2020) used a test particle Monte-Carlo approach to build an ionosphere model for Ganymede that provides the spatial distribution of multiple ion species originating from Ganymede's ionosphere. The magnetosphere models presented here used a relatively simplified approach to treating the ionosphere in that uniform, fixed plasma density and temperature are prescribed at the simulation boundary near Ganymede's surface (Zhou et al., 2019). In order to better understand the coupling between the magnetosphere and ionosphere, we may consider incorporating a realistic ionosphere model, such as that presented by Carnielli et al. (2020), into our global magnetosphere simulations in the future.

In the earlier study using a resistive MHD model with anomalous resistivity (Jia et al., 2010), essentially the same FTE occurrence rate of 20-50 seconds was predicted as in the Hall MHD and MHD-EPIC models. These three different models all show that reconnection is non-steady under steady upstream conditions, and the characteristic timescale for FTE formation is on the order of tens of seconds. Putting all these results together does seem to suggest that this may be an intrinsic timescale to Ganymede's magnetosphere dictated by the spatial size of the magnetosphere and the upstream plasma properties. However, developing quantitative relations still require further theoretical guidance and a series of carefully designed simulation runs to confirm.

The two models presented in this work predict a global reconnection efficiency of $\sim 60\%$ with flux ropes of $\sim R_G$ in length forming roughly 3 per minute at Ganymede's upstream magnetopause under the conditions of the Galileo G8 flyby. Compared with

the other Galileo flybys, G8 is the only one that occurred when Ganymede was inside Jupiter's central plasma sheet. Outside of the central plasma sheet, the Jovian plasma density is usually smaller and the ambient magnetic field strength is larger, which result in smaller $\beta$ and larger Alfvén velocity for the ambient plasma than for the G8 flyby. Because the ambient plasma and field conditions change periodically through each synodic rotation, it is of interest to examine how the properties of Ganymede's magnetopause reconnection vary depending on the location of the moon relative to Jupiter's plasma sheet. We have performed simulations for other relevant scenarios with different upstream Alfvén Mach number and external field orientation. Results from our preliminary runs suggest that larger Alfvén velocity and/or larger magnetic shear at the magnetopause boundary tend to produce larger reconnection efficiency. Detailed investigation of the dependence of reconnection-driven dynamics on the upstream conditions is beyond the scope of this paper, but will be conducted in our future work.

Despite the similarities of many quantities between the two models, there are also some differences worth mentioning. While the total plasma pressures in the Hall MHD and MHD-EPIC models are about the same, the perturbations of pressure and the upstream reconnection rate and FTE counts are larger in the Hall MHD results under the grid resolution we use. Tóth et al. (2016) compared the Hall MHD simulations with two different resolutions and found that the solution became much more dynamic at high grid resolution ($\sim 1/64\,R_G$) than the low grid resolution ($\sim 1/32\,R_G$), while PIC behaves more similar between the two resolutions. There are several possible reasons for the differences between our Hall MHD and MHD-EPIC results.. The larger plasma pressure perturbations as well as reconnection rate perturbations in Hall-MHD come from the fact that Hall-MHD produces more patchy perturbations at the magnetopause than MHD-EPIC, especially in small scale oscillations. The small perturbations in PIC compared to Hall MHD can be the intrinsic feature of either the physical models or the numerical solvers (i.e. semi-implicit Hall-MHD solver and the GL-ECSIM solver). However, we have not done a systematic study on this effect. Additionally, the comparison of electron and ion pressures between the Hall MHD and MHD-EPIC models in Figure 2 clearly shows that Hall MHD cannot handle the energy partition/conversion between the two species as in the kinetic PIC model, let alone the kinetic electron physics. The Hall MHD equations (Zhou et al., 2019) contain no explicit terms for controling electron pressure besides adiabatic heating.

From the particle distributions in phase space, we can see that kinetic physics only becomes important near the reconnection sites at the magnetopause boundary. In principle we can greatly speed up the simulation by embedding PIC regions only close to the magnetopause in the global Hall MHD runs. Many of the different measures for identifying the diffusion region are potentially useful for placing local PIC regions. However, this requires a more flexible configuration of the PIC domain, which will be the goal of future model development.

## 5 Conclusion

We have presented the results and predictions from Hall MHD and MHD-EPIC simulation of upstream reconnection dynamics. We find that under steady upstream conditions, magnetopause reconnection occurs in a non-steady manner. Flux ropes of $\sim R_G$ in length form on the magnetopause at a rate about 3/minute and produce spatiotemporal variations in plasma and field properties. Upon reaching grid resolution comparable to the electron inertial length, the MHD-EPIC model can resolve both electron and ion kinetics at the magnetopause and show localized non-gyrotropic behavior inside the diffusion region. We have developed a general and robust method to calculate the global reconnection rate that works for a highly dynamic reconnection process as present in Ganymede's upstream magnetosphere. The estimated global reconnection rate from the models is about

80 kV with 60% efficiency, and there is weak evidence of $\sim 1$ minute periodicity from the global reconnection efficiency fluctuation from the simulations.

The global Hall MHD and MHD-EPIC simulations presented in this paper allow us to study in detail how magnetic reconnection occurs at Ganymede's upstream magnetopause. Our simulation results provide predictions regarding the unsteadiness of reconnection, generation of FTEs, and the particle and field characteristics of the diffusion region around the X-lines. These predictions can be tested through and also be used to interpret new observations from future space missions, especially the upcoming Jupiter Icy Moon Explorer (JUICE) mission (Grasset et al., 2013).

## Appendix A Non-gyrotropy Measures

The three non-gyrotropy measures mentioned in the paper are all scalars independent of the coordinate. They can be computed efficiently point-wise with the following equations. Note that the electron subscripts are dropped in all the following equations.

The first measure $A\emptyset$ is defined as

$$A\emptyset = 2\frac{|P_{\perp 1} - P_{\perp 2}|}{P_{\perp 1} + P_{\perp 2}}, \tag{A1}$$

where the subscripts 1 and 2 represent the two orthogonal perpendicular directions to the magnetic field. It has been shown by Scudder and Daughton (2008) that in any frame $(x, y, z)$, if we define

$$\begin{aligned}
N_{xx} &= b_y b_y P_{zz} - 2b_y b_z P_{yz} + b_z b_z P_{yy}, \\
N_{xy} &= -b_y b_x P_{zz} + b_y b_z P_{xz} + b_z b_x P_{yz} - b_z b_z P_{xy}, \\
N_{xz} &= b_y b_x P_{yz} - b_y b_y P_{xz} - b_z b_x P_{yy} + b_z b_y P_{xy}, \\
N_{yy} &= b_x b_x P_{zz} - 2b_x b_z P_{xz} + b_z b_z P_{xx}, \\
N_{yz} &= -b_x b_x P_{yz} + b_x b_y P_{xz} + b_z b_x P_{xy} - b_z b_y P_{xx}, \\
N_{zz} &= b_x b_x P_{yy} - 2b_x b_y P_{xy} + b_y b_y P_{xx},
\end{aligned}$$

and

$$\begin{aligned}
\alpha &= N_{xx} + N_{yy} + N_{zz}, \\
\beta &= -(N_{xy}N_{xy} + N_{xz}N_{xz} + N_{yz}N_{yz} - N_{xx}N_{yy} - N_{xx}N_{zz} - N_{yy}N_{zz}),
\end{aligned}$$

then the agyrotropy can be expressed as

$$A\emptyset = 2\frac{\sqrt{\alpha^2 - 4\beta}}{\alpha}. \tag{A2}$$

The second measure of non-gyrotropy $D_{ng}$ suggested by Aunai et al. (2013) for electrons can be computed via

$$D_{ng} = 2\frac{\sqrt{P_{xy}^2 + P_{xz}^2 + P_{yz}^2}}{P_{xx} + P_{yy} + P_{zz}} \tag{A3}$$

The third measure proposed by Swisdak (2016) can be computed via

$$Q = 1 - 4\frac{I_2}{(I_1 - P_\parallel)(I_1 + 3P_\parallel)} \tag{A4}$$

where $I_1 = P_{xx}+P_{yy}+P_{zz}$ is the trace and $I_2 = P_{xx}P_{yy}+P_{xx}P_{zz}+P_{yy}P_{zz}-(P_{xy}P_{yx}+P_{xz}P_{zx}+P_{yz}P_{zy})$ is the principle minor.

## Acronyms

**SWMF** Space Weather Modeling Framework
**BATSRUS** Block Adaptive Tree Solarwind Roe Upwind Scheme
**PIC** Particle-in-Cell
**MHD** Magnetohydrodynamics
**MHD-EPIC** Magnetohydrodynamics with Embedded Particle-in-Cell
**FTE** Flux Transfer Event

## Acknowledgments

This research is supported by INSPIRE and NASA Solar System Workings program through grant NNX15AH28G. The authors acknowledge the Texas Advanced Computing Center (TACC) at The University of Texas at Austin for providing HPC and storage resources that have contributed to the research results reported within this paper. The simulation data can be accessed through Deep Blue at University of Michigan, `https://doi.org/10.7302/z5gd-0n53`.

The SWMF code (including BATS-R-US and iPIC3D) is publicly available through the `csem.engin.umich.edu/tools/swmf` web site after registration.

## References

Aunai, N., Hesse, M., & Kuznetsova, M. (2013). Electron nongyrotropy in the context of collisionless magnetic reconnection. *Physics of Plasmas*, *20*(9), 092903.

Broll, J., Fuselier, S., & Trattner, K. (2017). Locating dayside magnetopause reconnection with exhaust ion distributions. *Journal of Geophysical Research: Space Physics*, *122*(5), 5105–5113.

Carnielli, G., Galand, M., Leblanc, F., Leclercq, L., Modolo, R., Beth, A., ... Jia, X. (2019). First 3d test particle model of ganymede's ionosphere. *Icarus*, *330*, 42–59.

Carnielli, G., Galand, M., Leblanc, F., Modolo, R., Beth, A., & Jia, X. (2020). Constraining ganymede's neutral and plasma environments through simulations of its ionosphere and galileo observations. *Icarus*, 113691.

Cassak, P., & Shay, M. (2007). Scaling of asymmetric magnetic reconnection: General theory and collisional simulations. *Physics of Plasmas*, *14*(10), 102114.

Chen, Y., & Toth, G. (2019). Gauss's law satisfying energy-conserving semi-implicit particle-in-cell method. *Journal of Computational Physics*, *386*, 632–652.

Chen, Y., Tóth, G., Cassak, P., Jia, X., Gombosi, T. I., Slavin, J. A., ... Henderson, M. G. (2017). Global three-dimensional simulation of earth's dayside reconnection using a two-way coupled magnetohydrodynamics with embedded particle-in-cell model: Initial results. *Journal of Geophysical Research: Space Physics*, *122*(10), 10–318.

Chen, Y., Toth, G., Jia, X., Slavin, J., Sun, W., Markidis, S., ... Raines, J. (2019). Studying dawn-dusk asymmetries of mercury's magnetotail using mhd-epic simulations. *arXiv preprint arXiv:1904.06753*.

Daldorff, L. K., Tóth, G., Gombosi, T. I., Lapenta, G., Amaya, J., Markidis, S., & Brackbill, J. U. (2014). Two-way coupling of a global hall magnetohydrodynamics model with a local implicit particle-in-cell model. *Journal of Computational Physics*, *268*, 236–254.

Dorelli, J. C., Glocer, A., Collinson, G., & Tóth, G. (2015). The role of the hall effect in the global structure and dynamics of planetary magnetospheres: Ganymede as a case study. *Journal of Geophysical Research: Space Physics*, *120*(7), 5377–5392.

Flanders, H. (1973). Differentiation under the integral sign. *The American Mathematical Monthly*, *80*(6), 615–627.

Grasset, O., Dougherty, M., Coustenis, A., Bunce, E., Erd, C., Titov, D., ... others (2013). Jupiter icy moons explorer (juice): An esa mission to orbit ganymede and to characterise the jupiter system. *Planetary and Space Science*, *78*, 1–21.

Gurnett, D., Kurth, W., Roux, A., Bolton, S., & Kennel, C. (1996). Evidence for a magnetosphere at ganymede from plasma-wave observations by the galileo spacecraft. *Nature*, *384*(6609), 535–537.

Hu, Y., Guo, X., & Wang, C. (2007). On the ionospheric and reconnection potentials of the earth: Results from global mhd simulations. *Journal of Geophysical Research: Space Physics*, *112*(A7).

Jia, X., Walker, R. J., Kivelson, M. G., Khurana, K. K., & Linker, J. A. (2008). Three-dimensional mhd simulations of ganymede's magnetosphere. *Journal of Geophysical Research: Space Physics*, *113*(A6).

Jia, X., Walker, R. J., Kivelson, M. G., Khurana, K. K., & Linker, J. A. (2009). Properties of ganymede's magnetosphere inferred from improved three-dimensional mhd simulations. *Journal of Geophysical Research: Space Physics*, *114*(A9).

Jia, X., Walker, R. J., Kivelson, M. G., Khurana, K. K., & Linker, J. A. (2010). Dynamics of ganymede's magnetopause: Intermittent reconnection under steady external conditions. *Journal of Geophysical Research: Space Physics*, *115*(A12).

Kaweeyanun, N., Masters, A., & Jia, X. (2020). Favorable conditions for magnetic reconnection at ganymede's upstream magnetopause. *Geophysical Research Letters*, e2019GL086228.

Kivelson, M., Khurana, K., Russell, C., Walker, R., Warnecke, J., Coroniti, F., ... Schubert, G. (1996). Discovery of ganymede's magnetic field by the galileo spacecraft. *Nature*, *384*(6609), 537–541.

Kivelson, M. G., Bagenal, F., Kurth, W. S., Neubauer, F. M., Paranicas, C., & Saur, J. (2004). Magnetospheric interactions with satellites. *Jupiter: The planet, satellites and magnetosphere*, 513–536.

Kivelson, M. G., Khurana, K., Coroniti, F., Joy, S., Russell, C., Walker, R., ... Polanskey, C. (1997). The magnetic field and magnetosphere of ganymede. *Geophysical Research Letters*, *24*(17), 2155–2158.

Kivelson, M. G., Khurana, K., & Volwerk, M. (2002). The permanent and inductive magnetic moments of ganymede. *Icarus*, *157*(2), 507–522.

Kivelson, M. G., Warnecke, J., Bennett, L., Joy, S., Khurana, K., Linker, J., ... Polanskey, C. (1998). Ganymede's magnetosphere: Magnetometer overview. *Journal of Geophysical Research: Planets*, *103*(E9), 19963–19972.

Kopp, A., & Ip, W.-H. (2002). Resistive mhd simulations of ganymede's magnetosphere 1. time variabilities of the magnetic field topology. *Journal of Geophysical Research: Space Physics*, *107*(A12), SMP–41.

Ma, Y., Russell, C. T., Toth, G., Chen, Y., Nagy, A. F., Harada, Y., ... others (2018). Reconnection in the martian magnetotail: Hall-mhd with embedded particle-in-cell simulations. *Journal of Geophysical Research: Space Physics*, *123*(5), 3742–3763.

Markidis, S., Lapenta, G., et al. (2010). Multi-scale simulations of plasma with ipic3d. *Mathematics and Computers in Simulation*, *80*(7), 1509–1519.

Scudder, J., & Daughton, W. (2008). "illuminating" electron diffusion regions of collisionless magnetic reconnection using electron agyrotropy. *Journal of Geophysical Research: Space Physics*, *113*(A6).

Shay, M., Phan, T., Haggerty, C., Fujimoto, M., Drake, J., Malakit, K., ... Swisdak, M. (2016). Kinetic signatures of the region surrounding the x line in asymmetric (magnetopause) reconnection. *Geophysical Research Letters*, *43*(9), 4145–4154.

Smith, M., & Rodgers, D. (1991). Ion distributions at the dayside magnetopause. *Journal of Geophysical Research: Space Physics*, *96*(A7), 11617–11624.

Swisdak, M. (2016). Quantifying gyrotropy in magnetic reconnection. *Geophysical Research Letters*, *43*(1), 43–49.

Tóth, G., Jia, X., Markidis, S., Peng, I. B., Chen, Y., Daldorff, L. K., ... others (2016). Extended magnetohydrodynamics with embedded particle-in-cell simulation of ganymede's magnetosphere. *Journal of Geophysical Research: Space Physics*, *121*(2), 1273–1293.

Tóth, G., Ma, Y., & Gombosi, T. I. (2008). Hall magnetohydrodynamics on block-adaptive grids. *Journal of Computational Physics*, *227*(14), 6967–6984.

Tóth, G., Van der Holst, B., Sokolov, I. V., De Zeeuw, D. L., Gombosi, T. I., Fang, F., ... others (2012). Adaptive numerical algorithms in space weather modeling. *Journal of Computational Physics*, *231*(3), 870–903.

Wang, L., Germaschewski, K., Hakim, A., Dong, C., Raeder, J., & Bhattacharjee, A. (2018). Electron physics in 3-d two-fluid 10-moment modeling of ganymede's magnetosphere. *Journal of Geophysical Research: Space Physics*, *123*(4), 2815–2830.

Williams, D., Mauk, B., McEntire, R., Roelof, E., Armstrong, T., Wilken, B., ... others (1997). Energetic particle signatures at ganymede: Implications for ganymede's magnetic field. *Geophysical research letters*, *24*(17), 2163–2166.

Zenitani, S., Hesse, M., Klimas, A., & Kuznetsova, M. (2011). New measure of the dissipation region in collisionless magnetic reconnection. *Physical review letters*, *106*(19), 195003.

Zhou, H., Tóth, G., Jia, X., Chen, Y., & Markidis, S. (2019). Embedded kinetic simulation of ganymede's magnetosphere: Improvements and inferences. *Journal of Geophysical Research: Space Physics*.

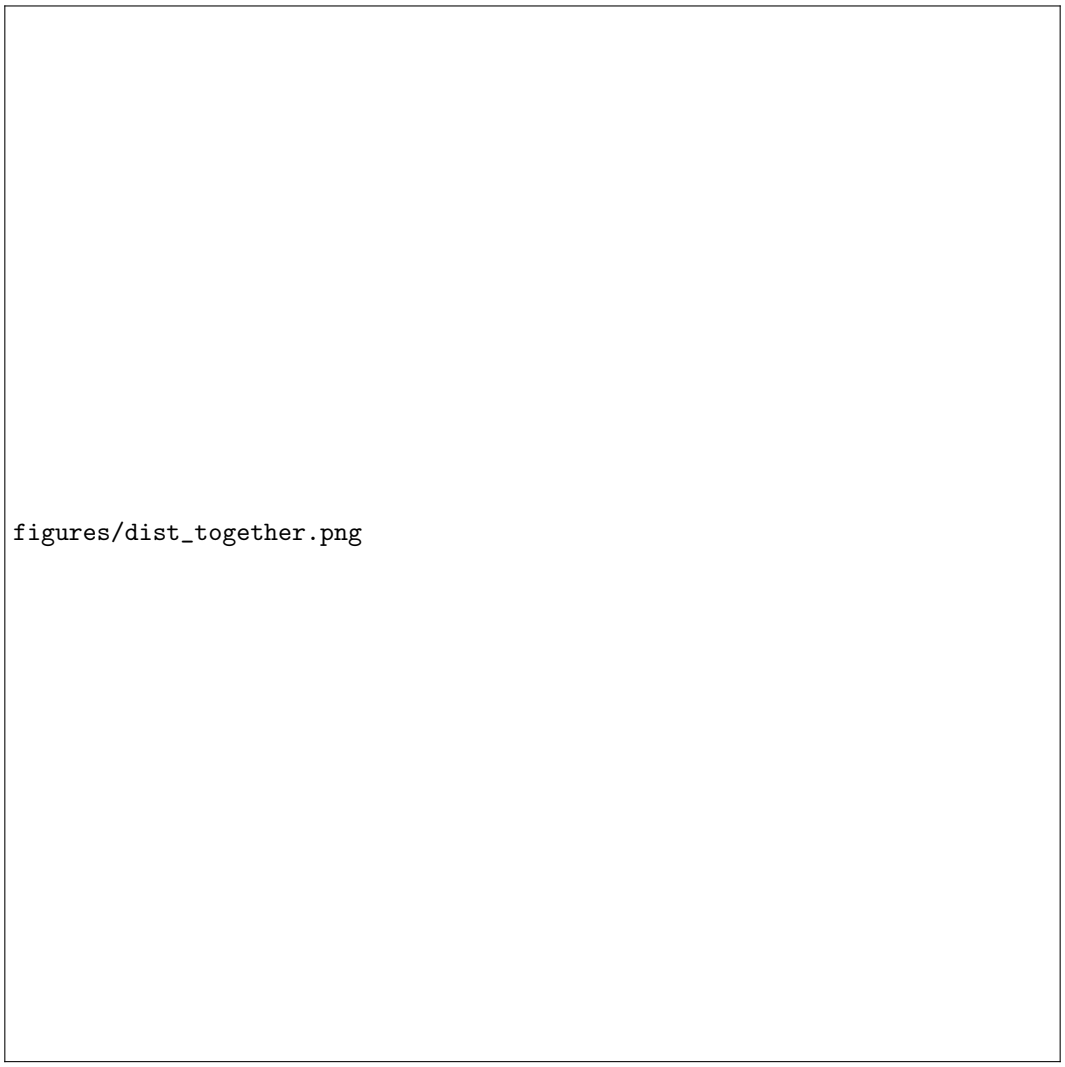


**Figure 9.** Top panels: normalized velocity distribution functions of electrons and ions near the meridional plane in selected boxes shown in the bottom plot. For each species, the integrated $u_y - u_x$ distributions are presented on the left, and the $u_y - u_z$ distributions is presented on the right. Bottom panel: $y = 0$ equatorial cut near the X-line with color contours of $E_z$, mapped magnetic field lines and a dotted line along the magnetopause of $B_z = 0$. Positive x direction points towards the moon. The selected electron box regions 1-4 are colored in red, and ion box regions 5-8 are colored in cyan.

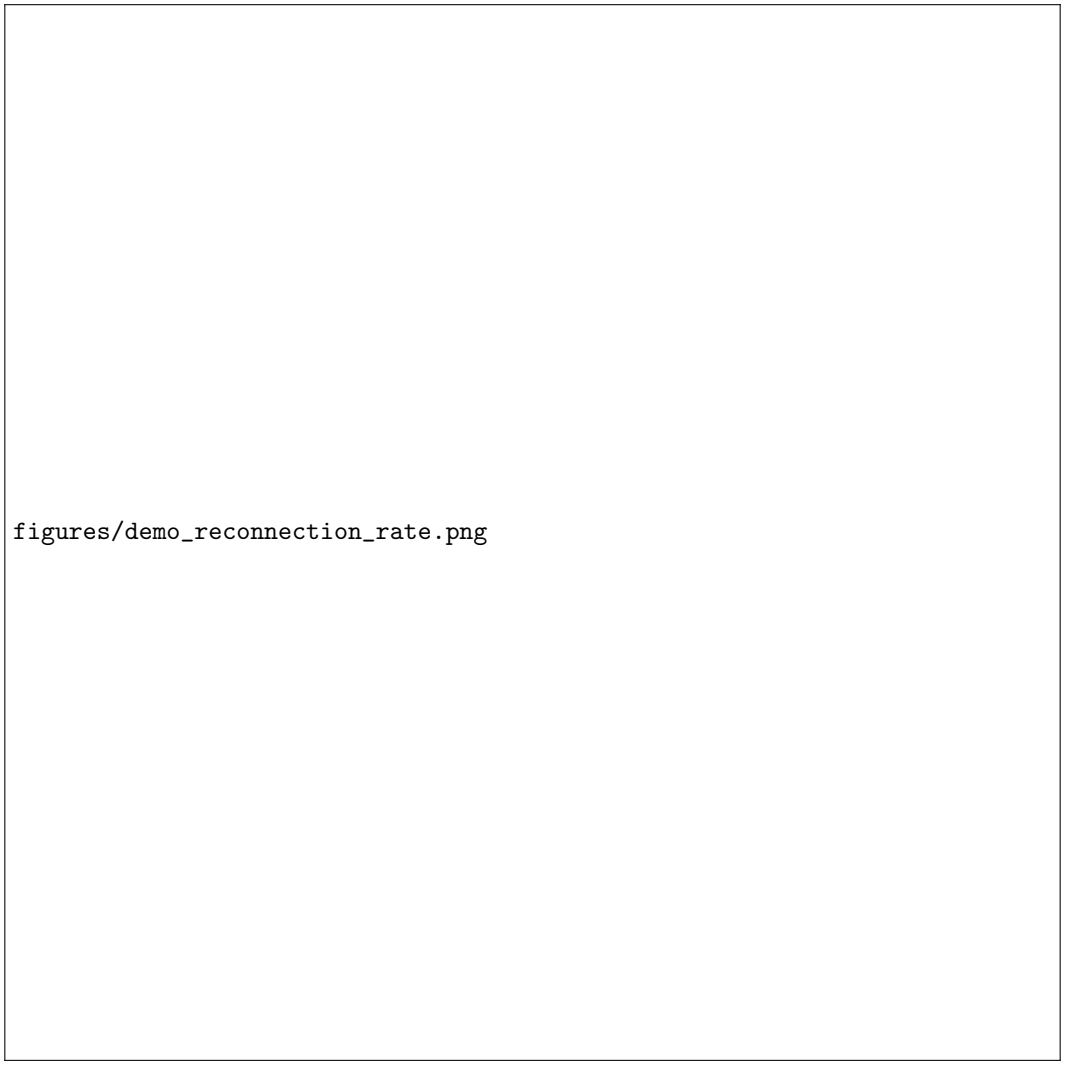


**Figure 10.** Illustration of reconnection efficiency calculation in GPhiO coordinates. (a) shows a 3D view of the magnetic field geometry near Ganymede (represented by a blue sphere). The black lines are magnetic field lines with starting points in the $y = 0$ plane, red lines are ones that just get reconnected at the upstream magnetopause, and green lines are those that connect to the tail reconnection site. (b) displays the upstream half of the half-closed field line region colored with $B_z$ in the $z = 2\,R_G$ plane corresponding to the cut plane in (a). The upstream boundary curve $U$ is shown by the red line. The middle straight line $M$ colored in blue closes the boundary of surface $A$.

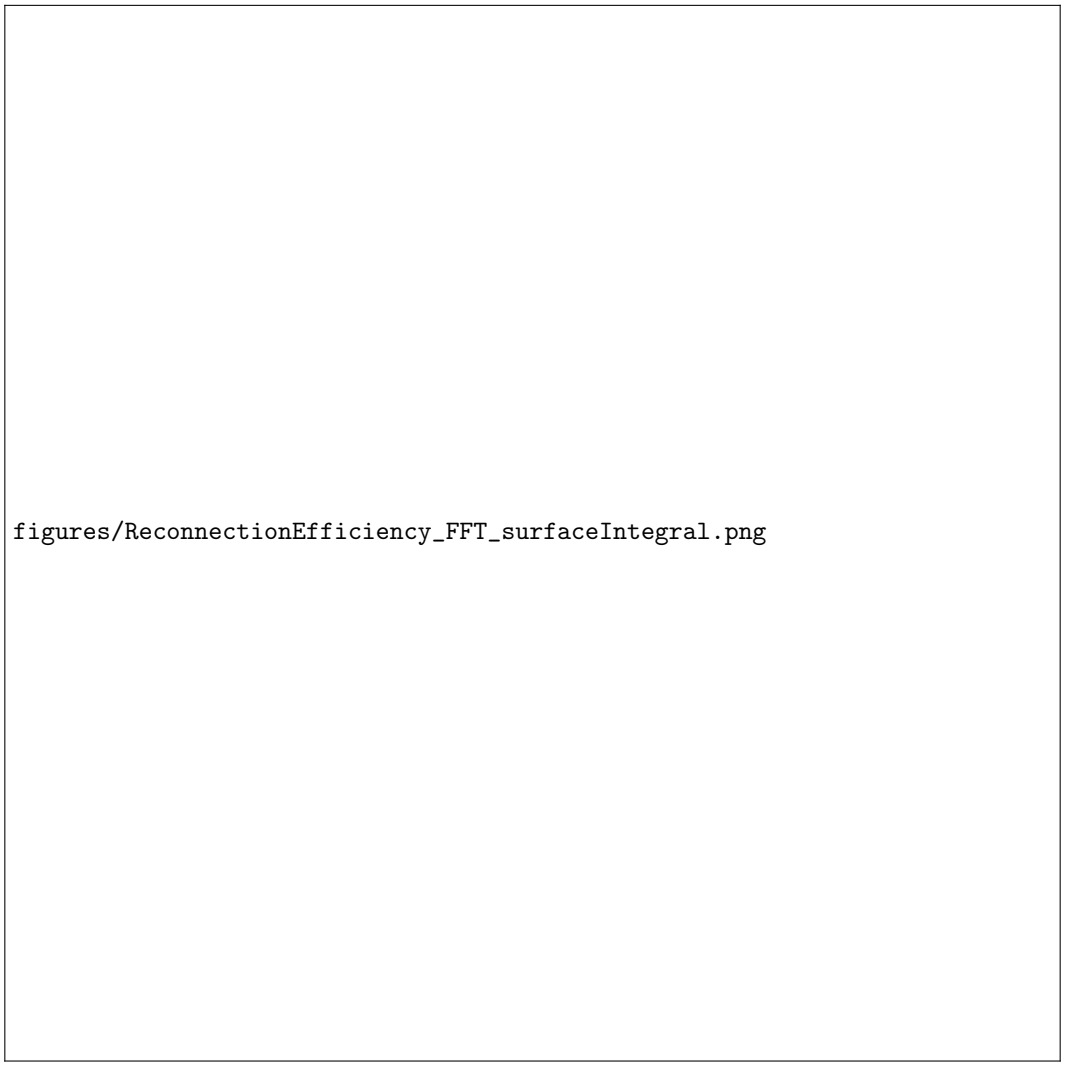


**Figure 11.** Global upstream reconnection rates from (a) Hall MHD in blue and (b) MHD-EPIC in orange throughout the 20-minute simulations. The average rate is $82.9 \pm 18.3$ kV for Hall MHD and $83.6 \pm 8.2$ kV for MHD-EPIC. Note that MHD-EPIC starts from $t = 300$ s of the Hall MHD run. The black dashed lines represent the means of the reconnection rate, with standard deviation bar on the right. The red and green dash-dotted lines represent sample FTEs identified from large thermal pressure perturbations on the magnetopause in Figure 6 at $z = \pm 0.5\, R_G$, respectively. (c) Periodograms of the global upstream reconnection rate from Hall MHD in blue and MHD-EPIC in orange. x axis is the period and y axis is the power spectrum density.

**Figure 1.**

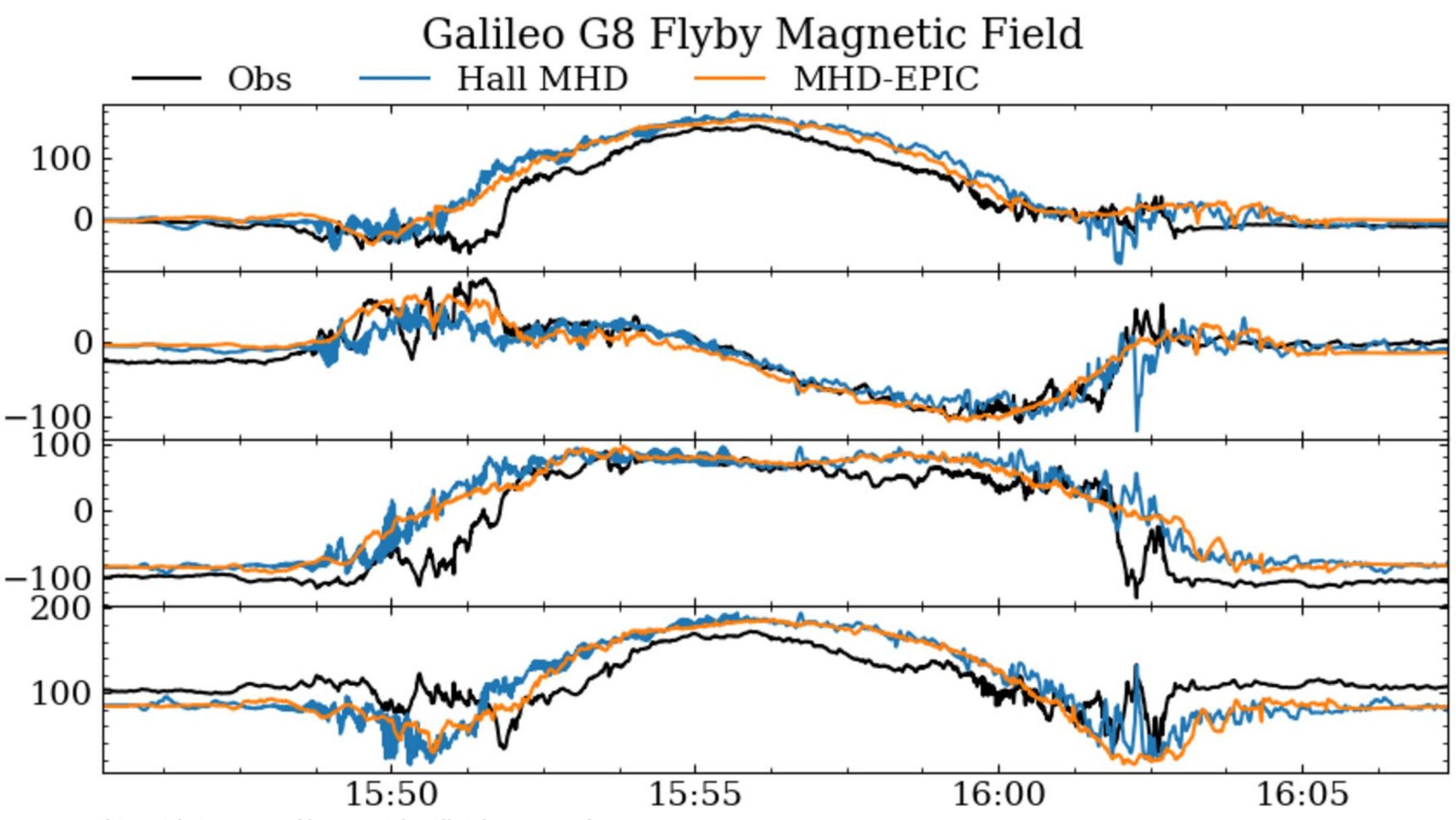

**Figure 2.**

(a)

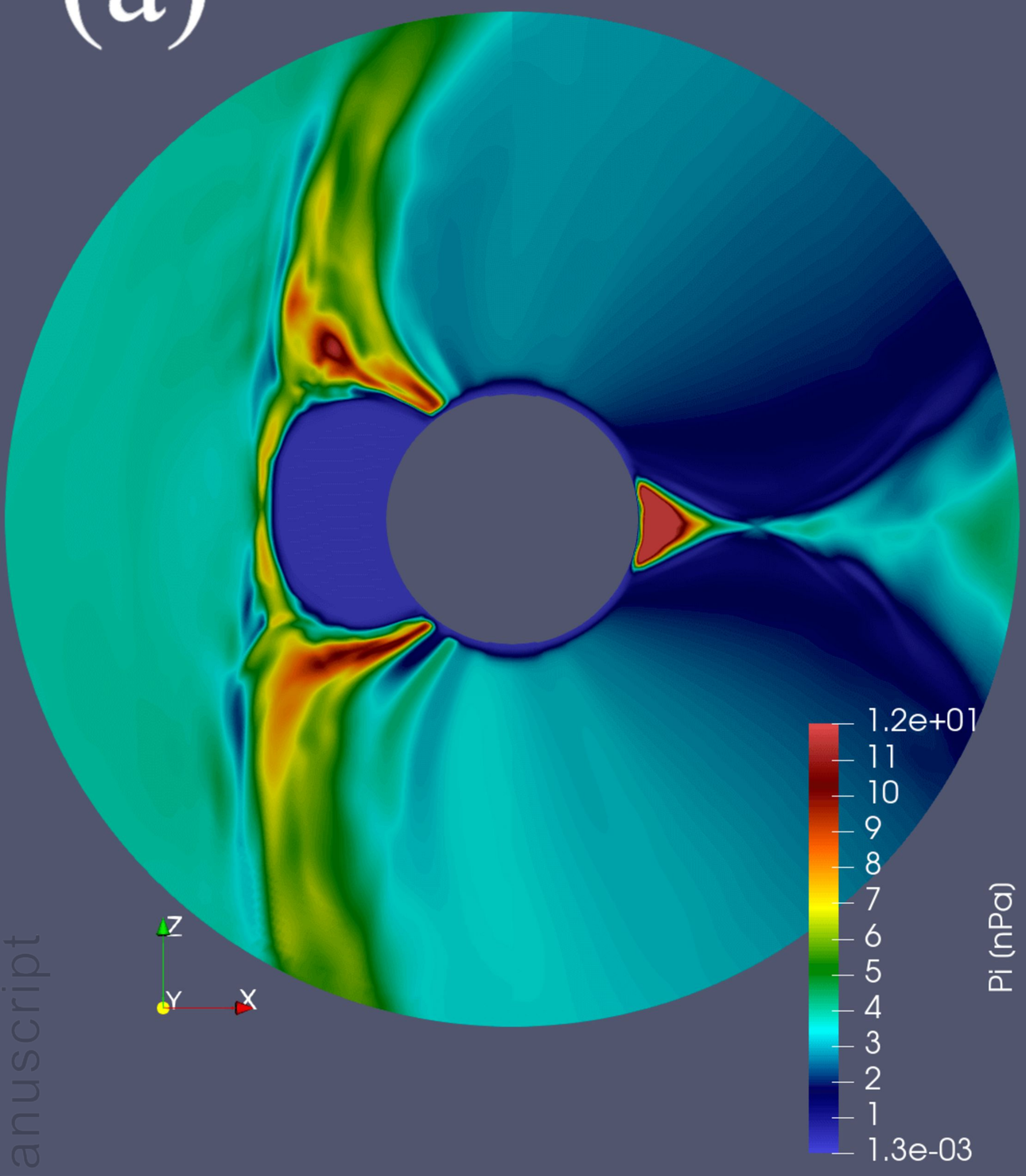


(b)

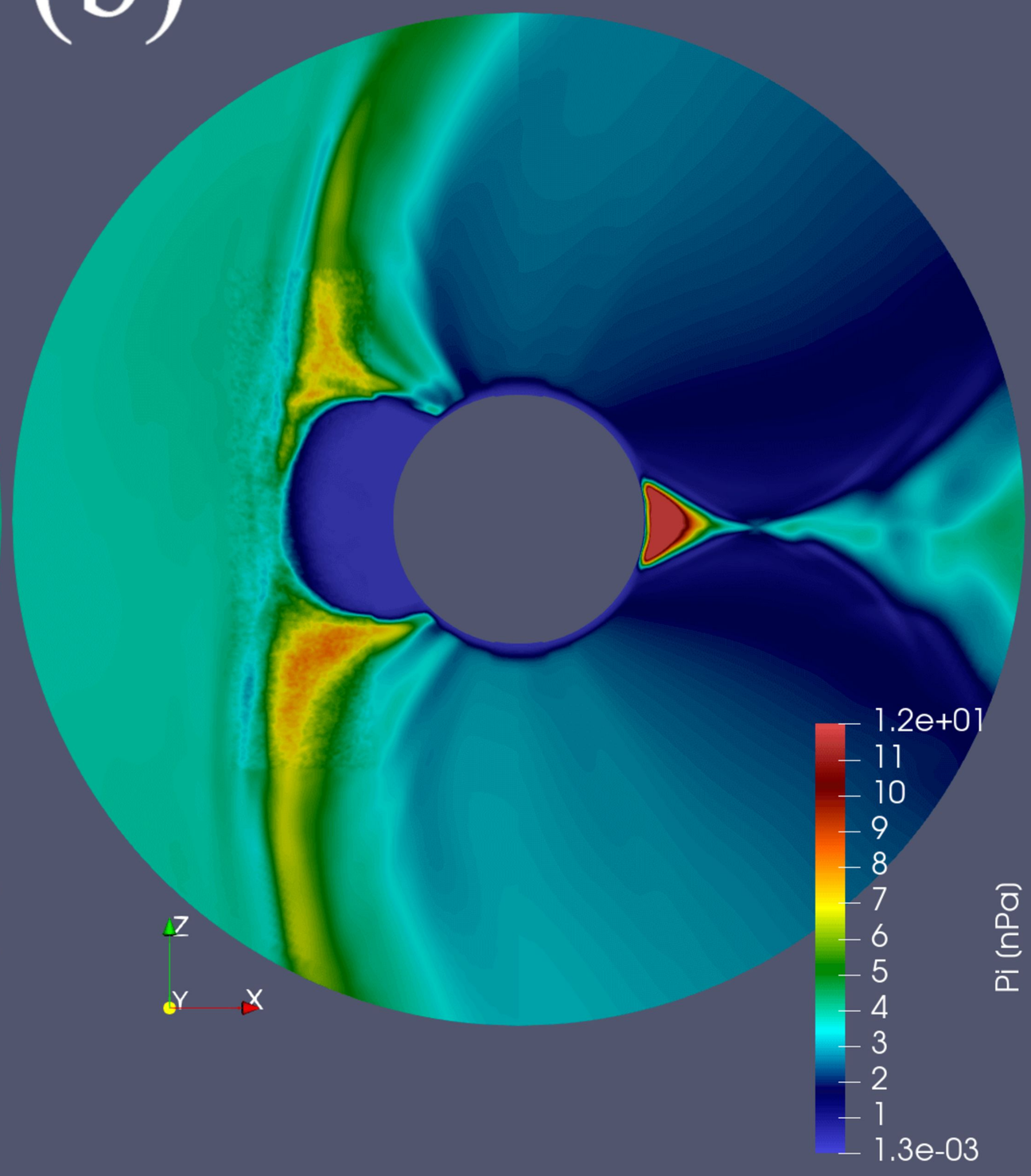


(c)

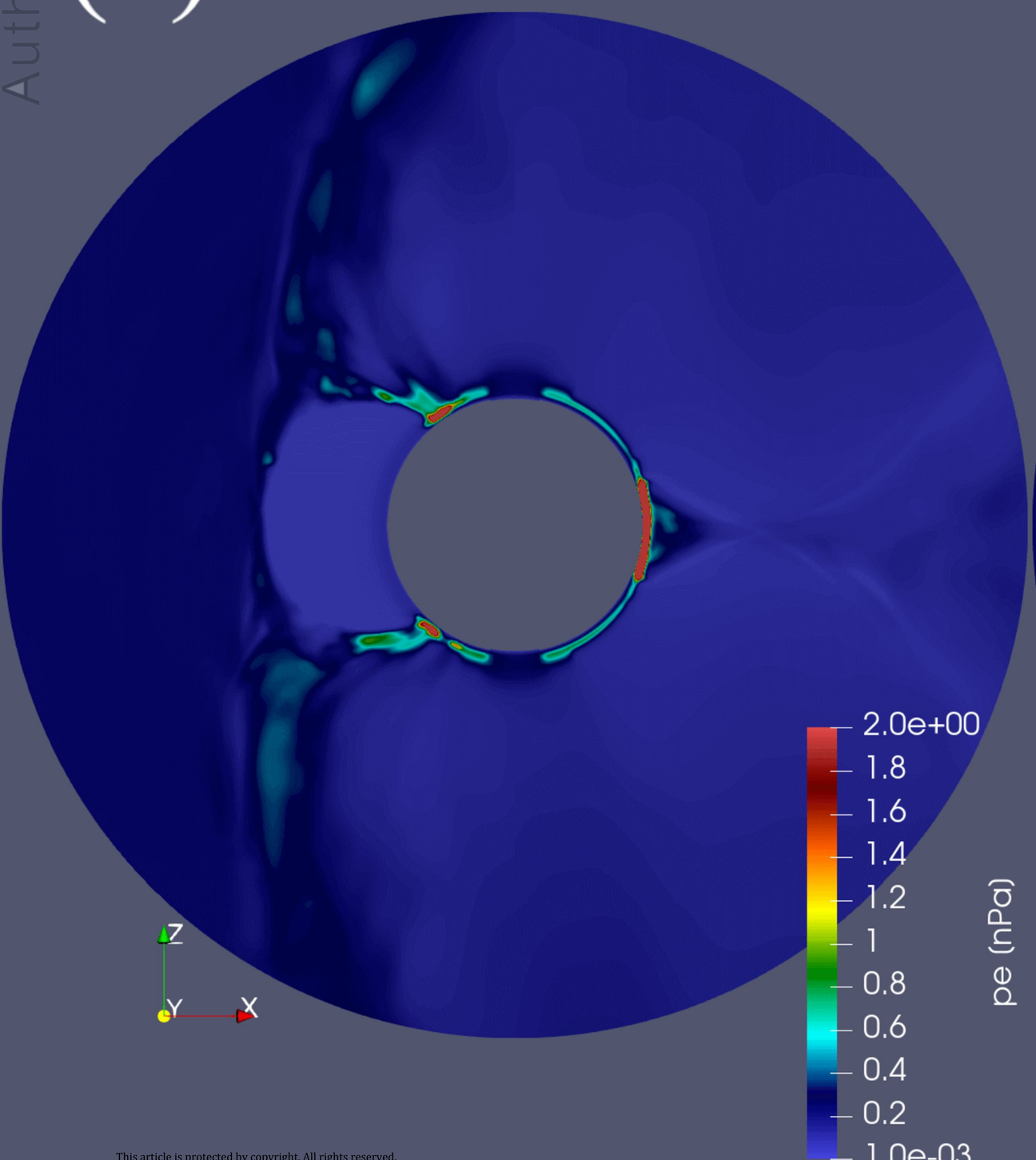


(d)

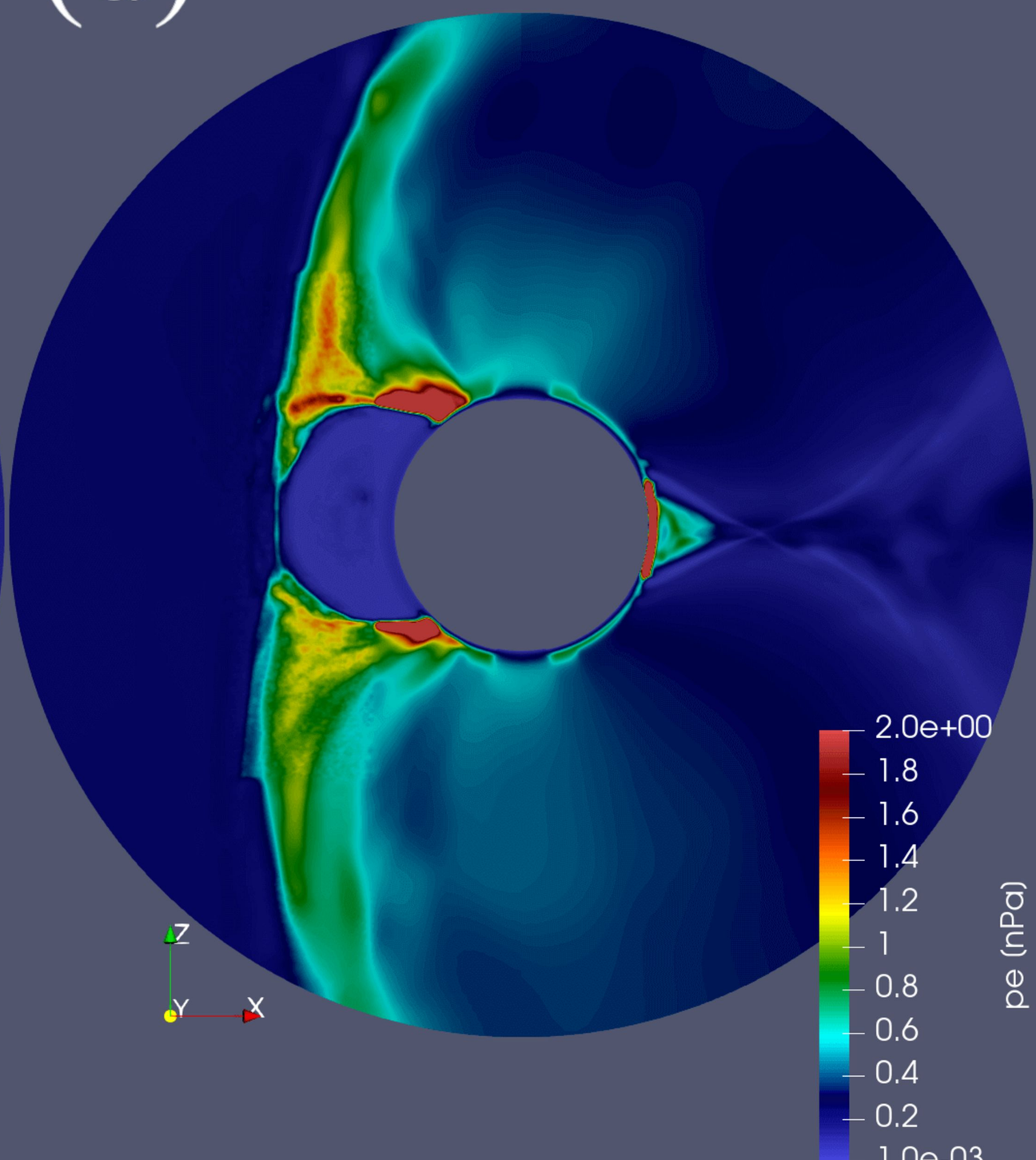

**Figure 3.**

(a)

(b)

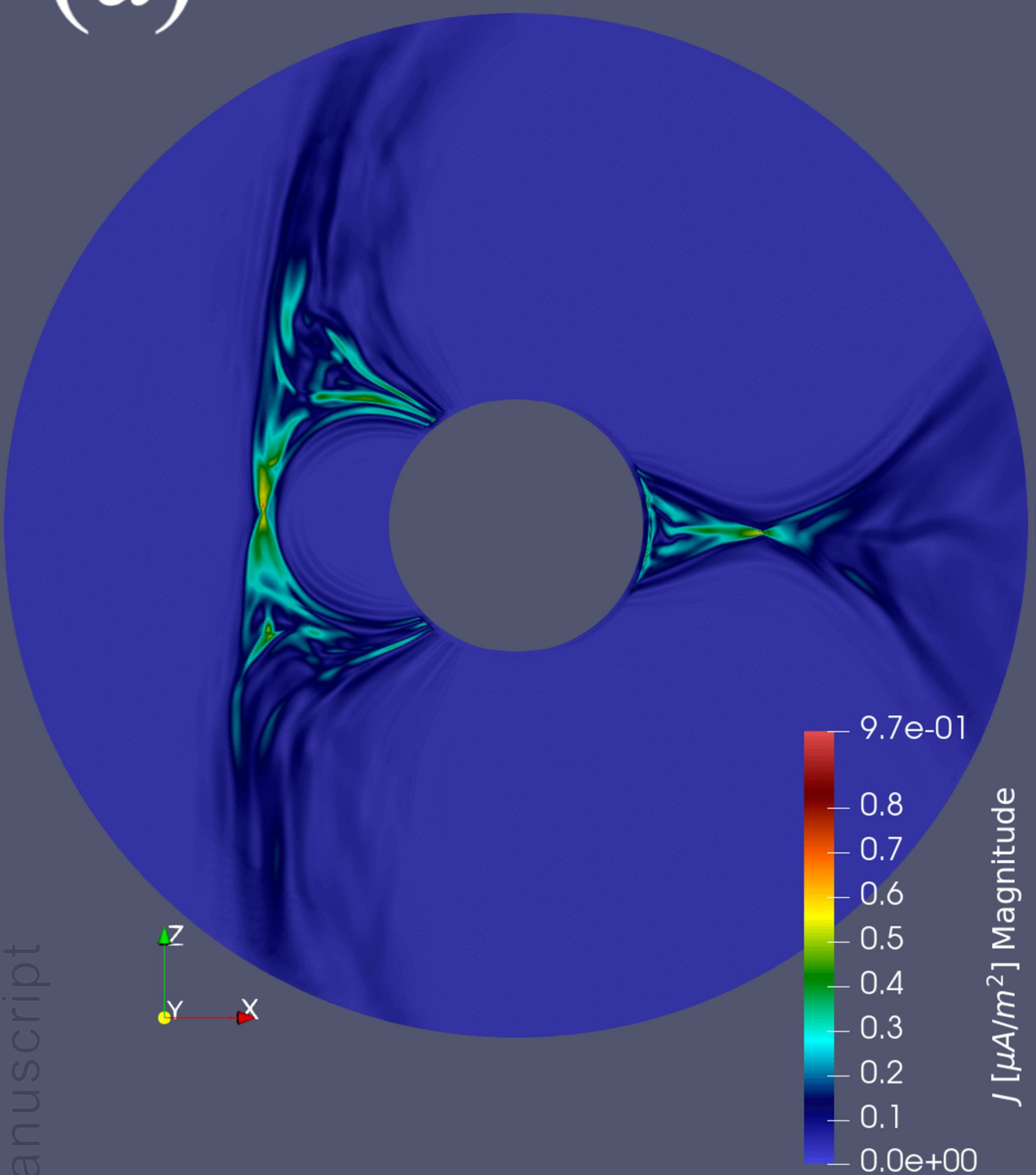


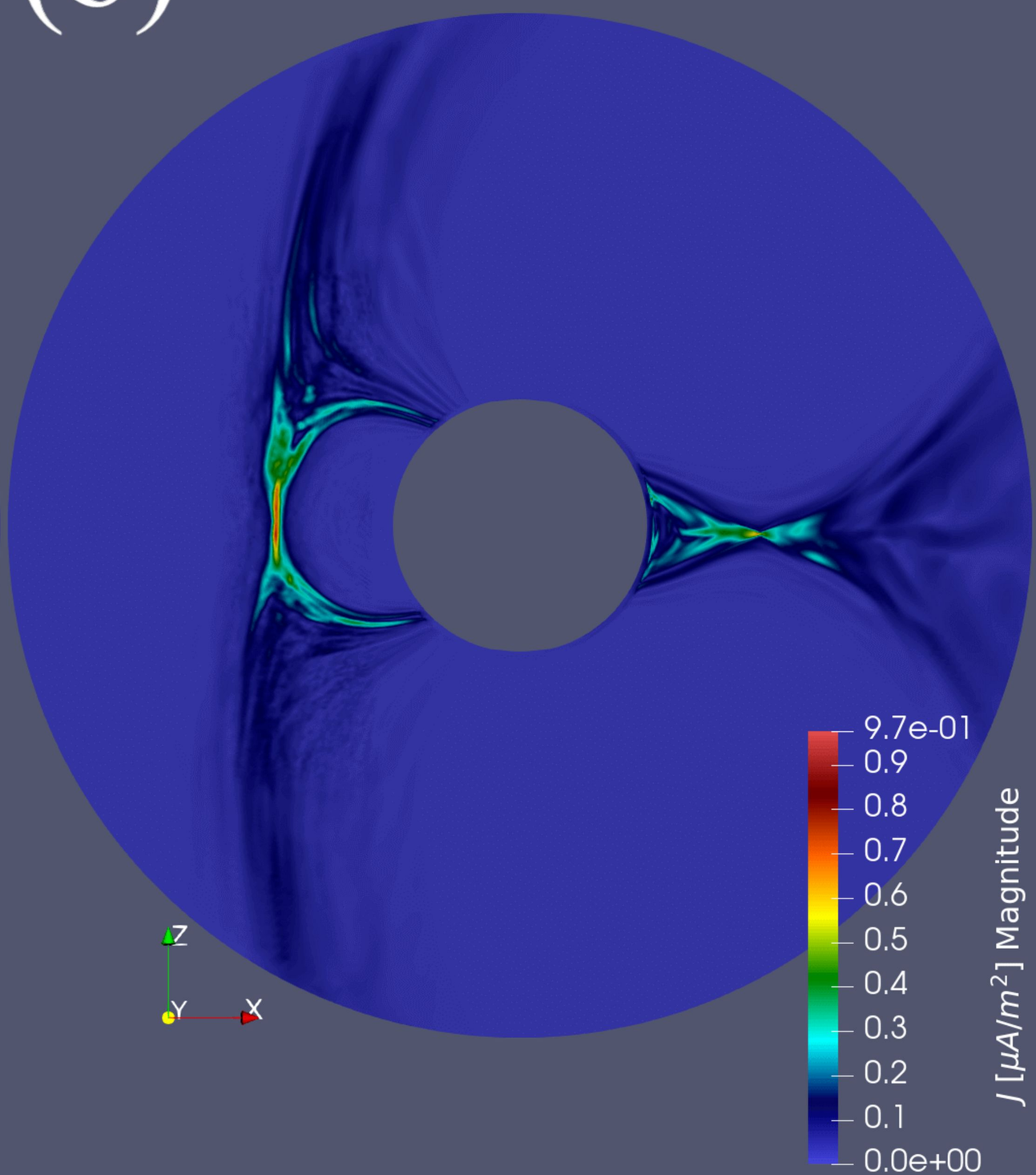


(c)

(d)

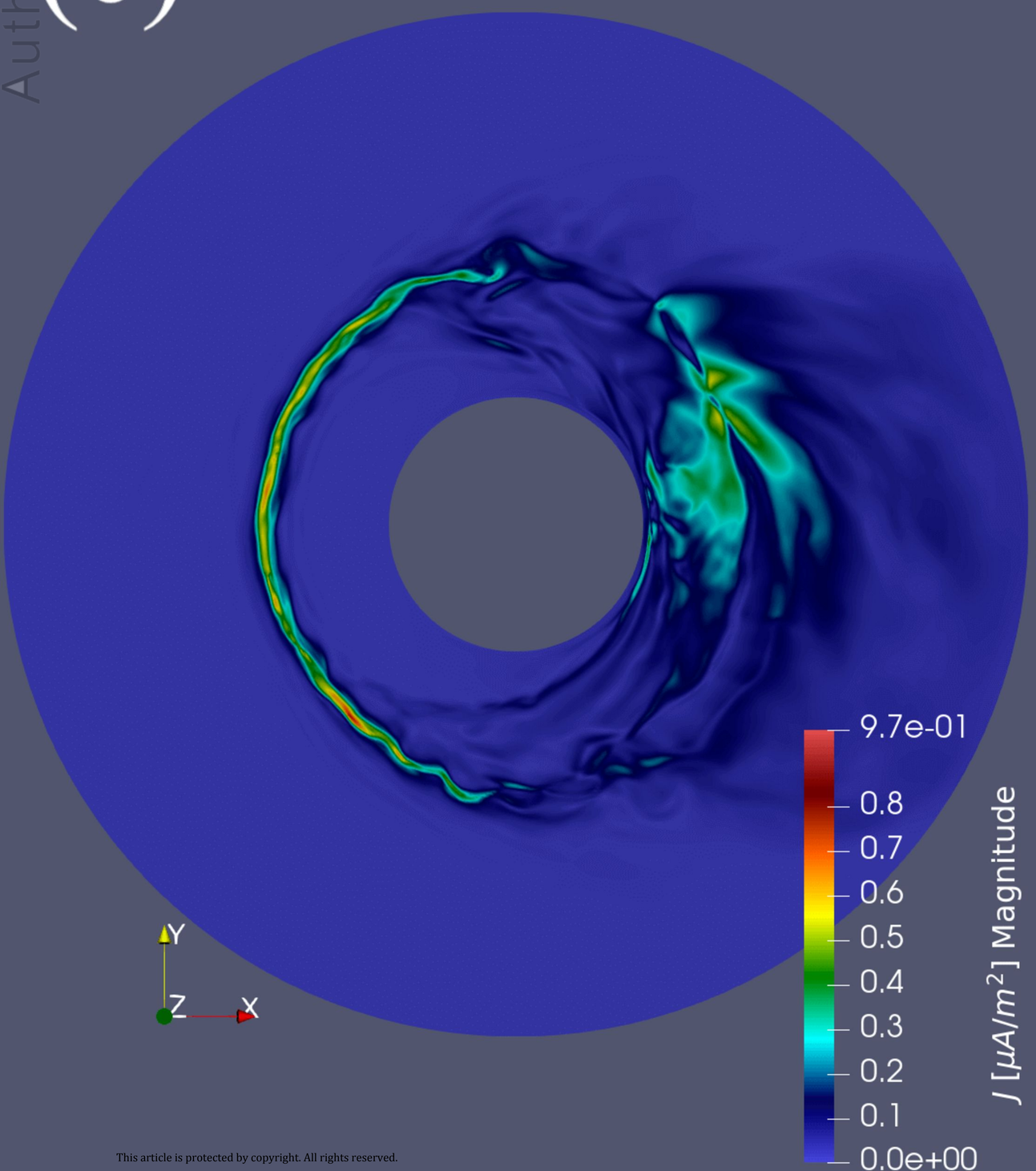


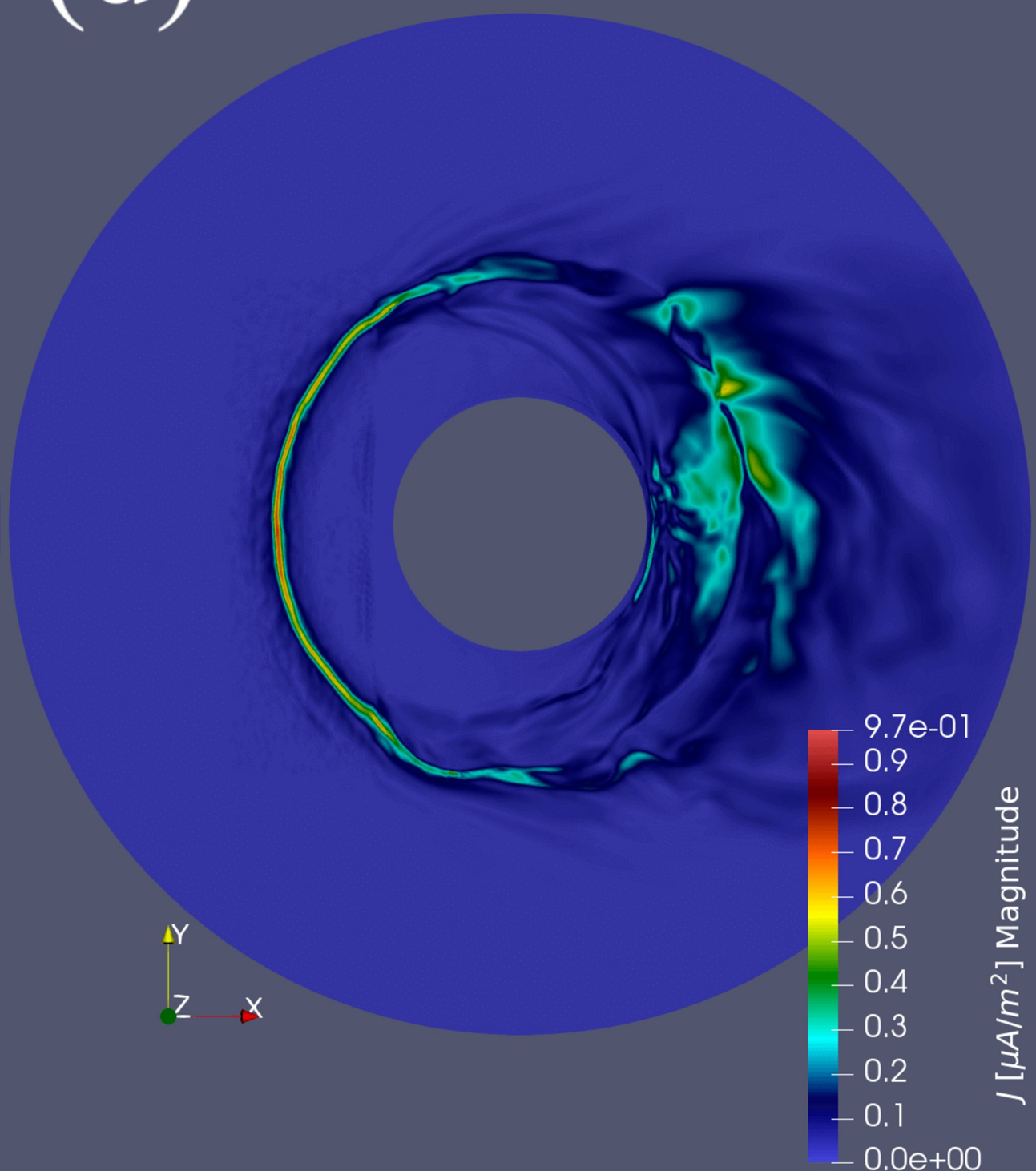

**Figure 4.**

(a)

t = 611s

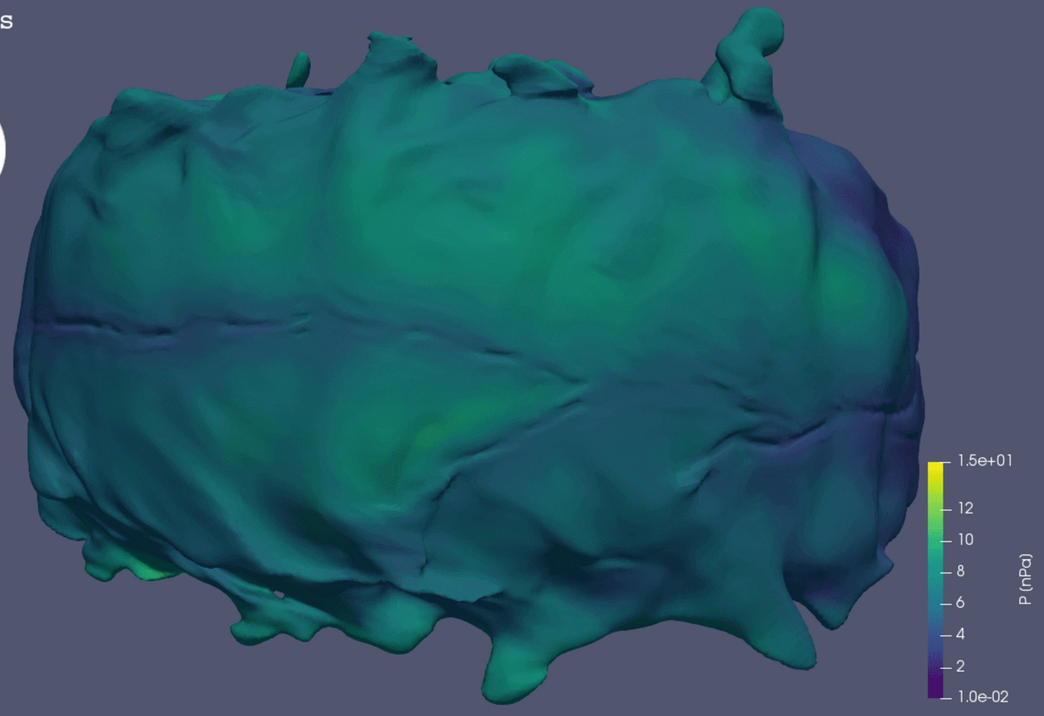


t = 695s

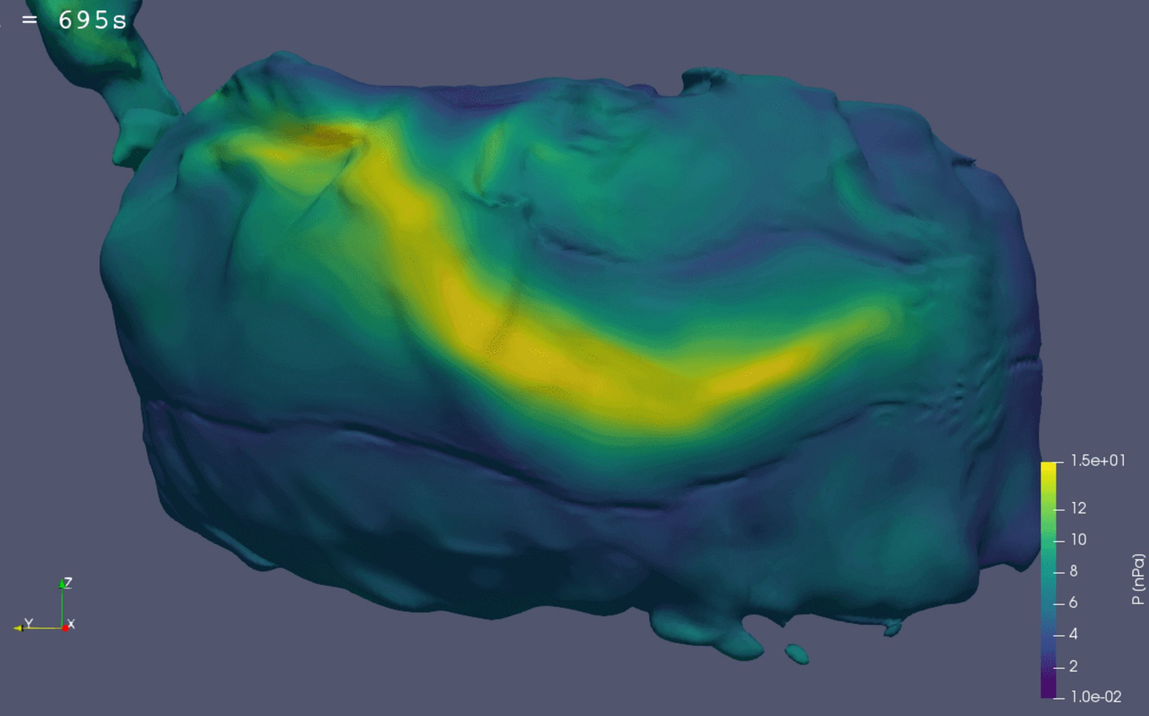


t = 611s

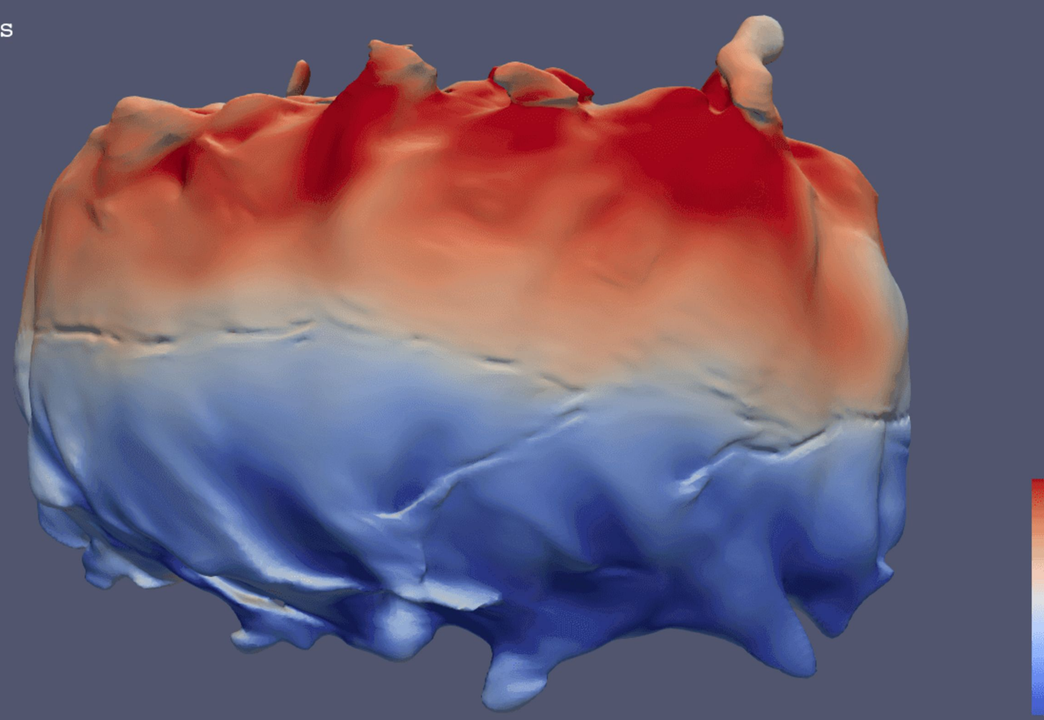


t = 695s

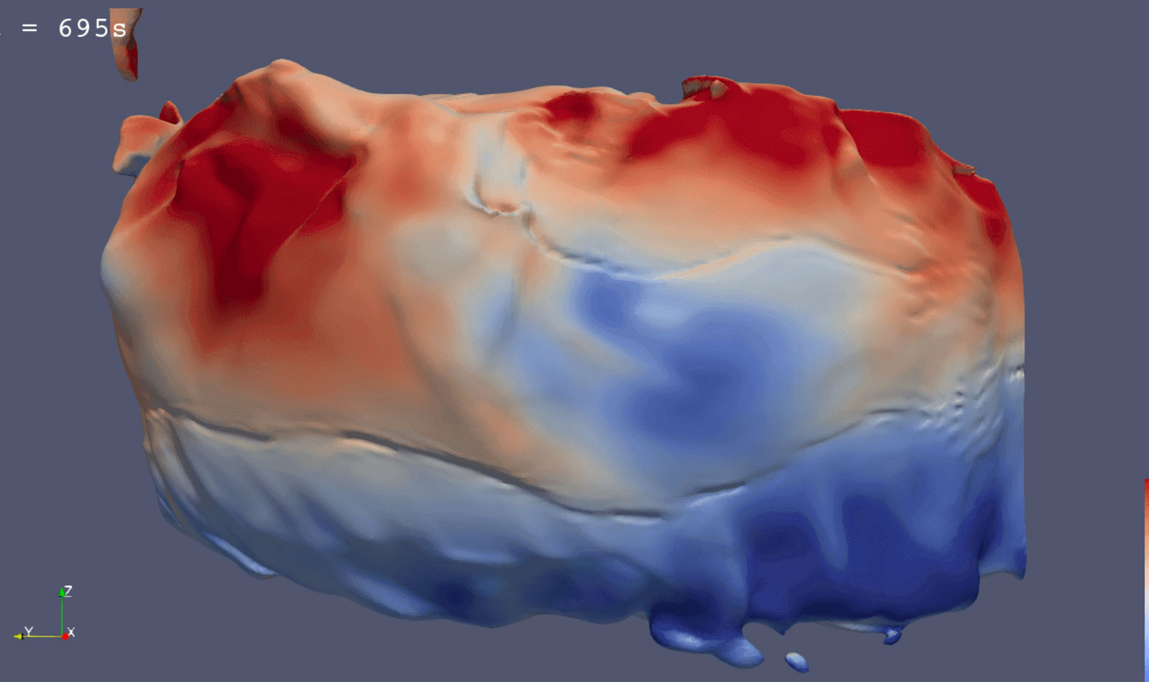


t = 703s

(b)

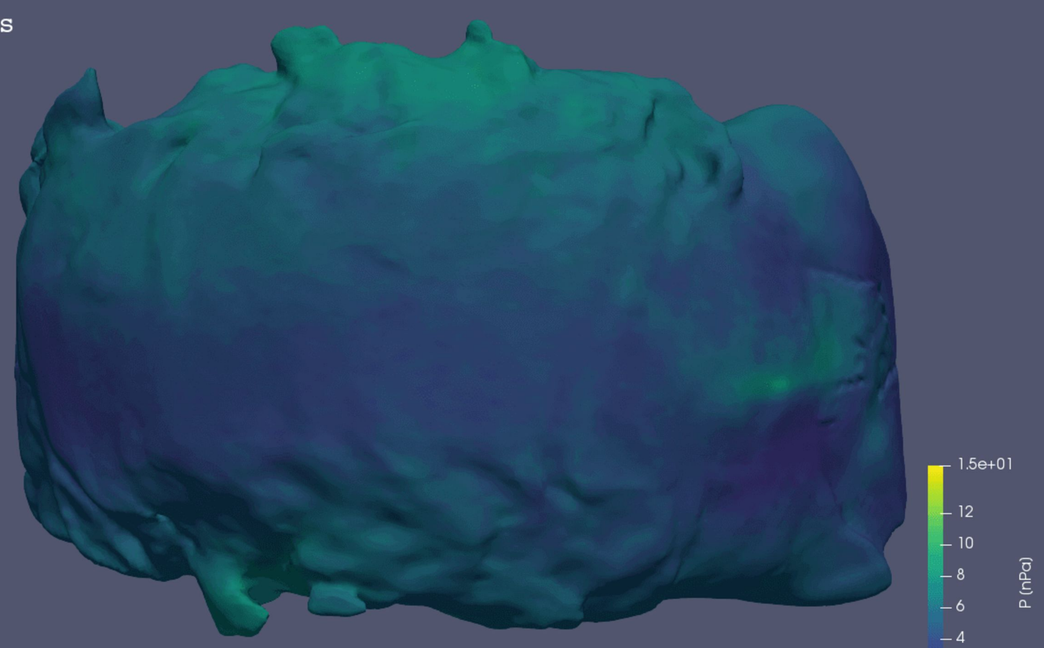


t = 725s

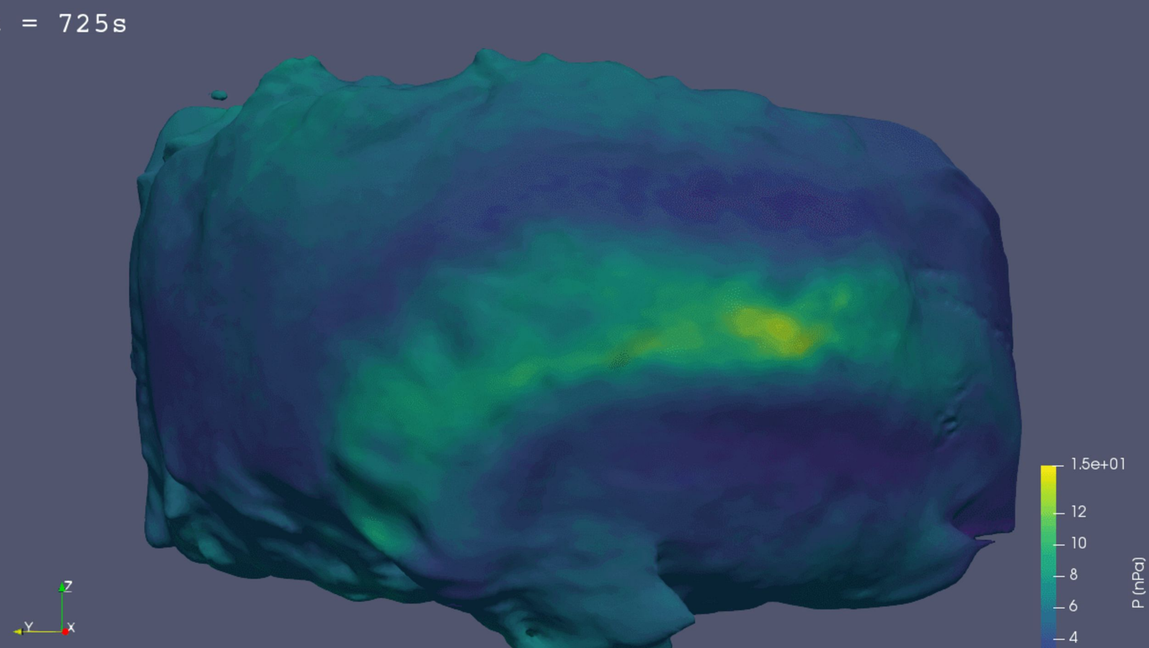


t = 703s

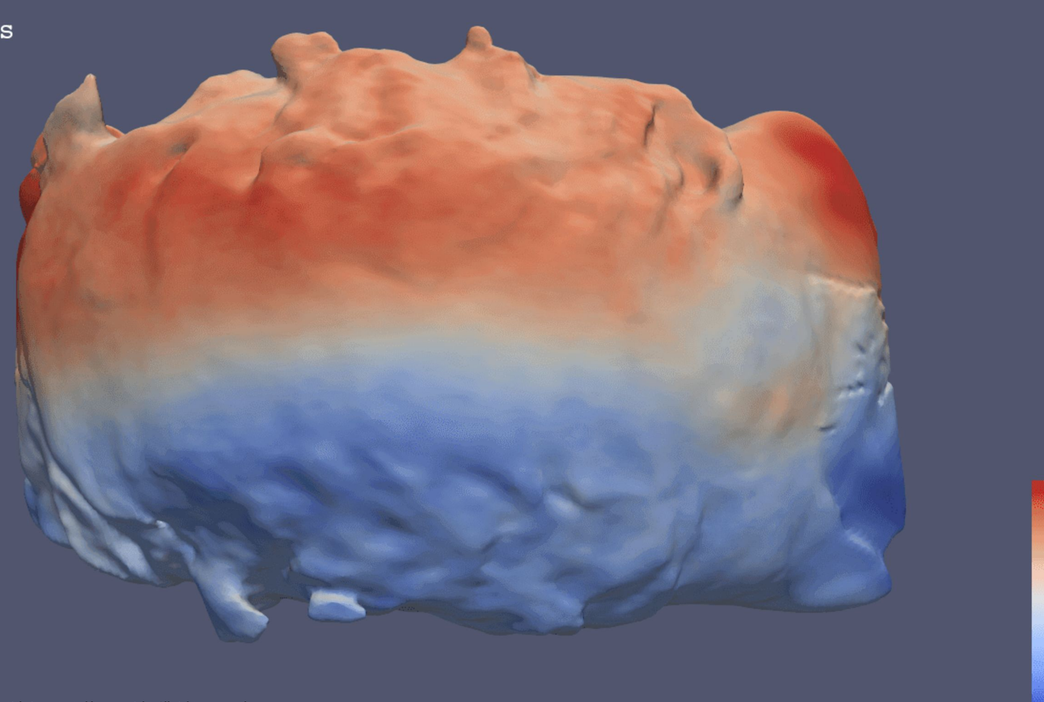


t = 725s

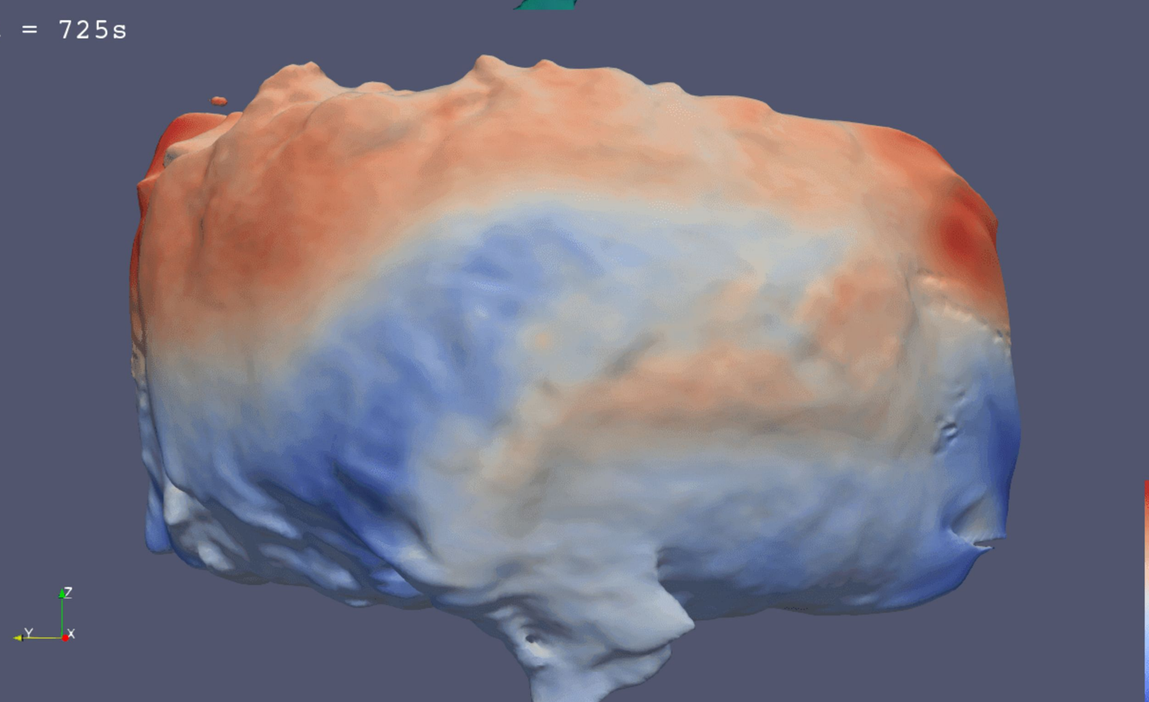

**Figure 5.**

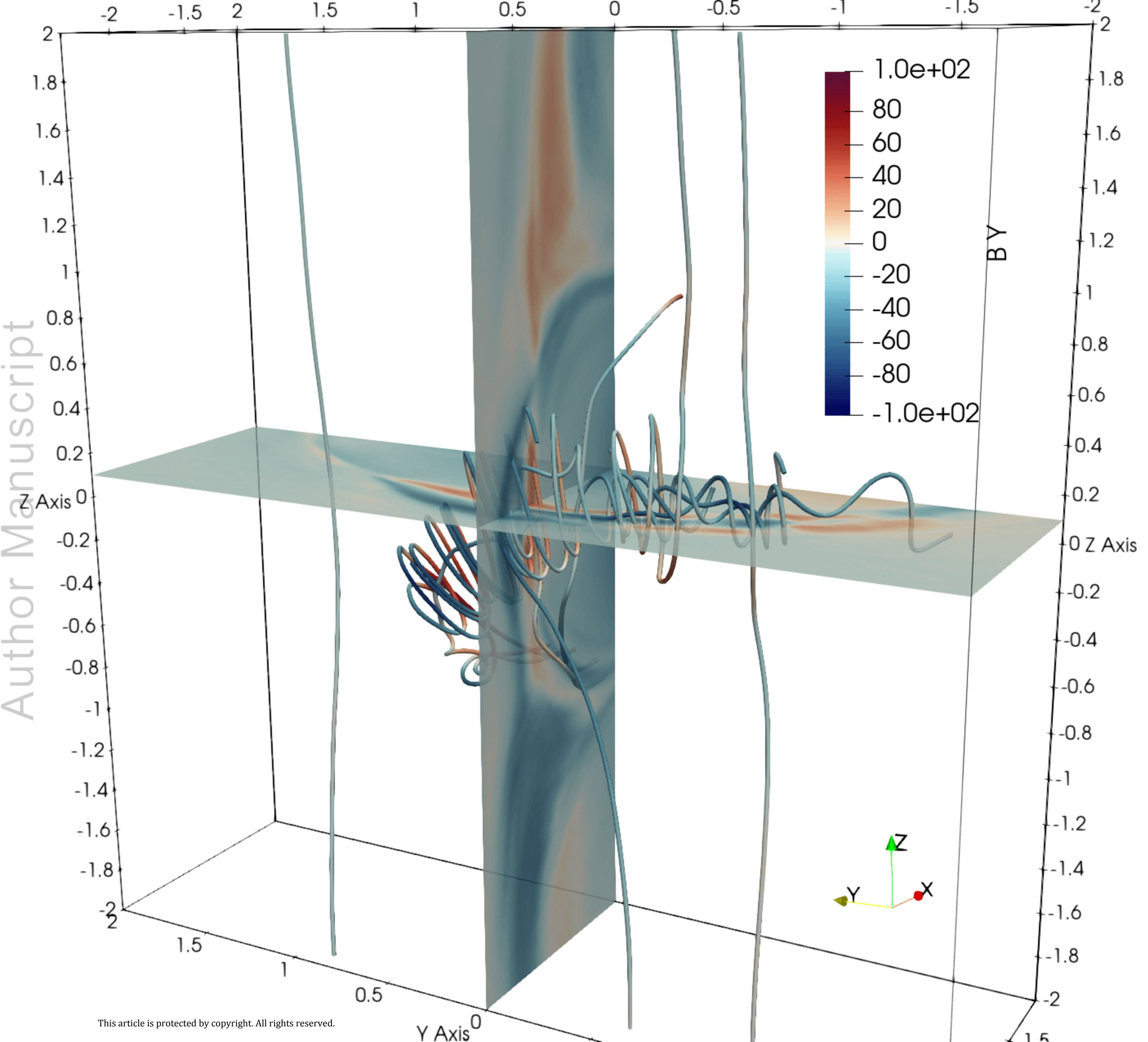

**Figure 6.**

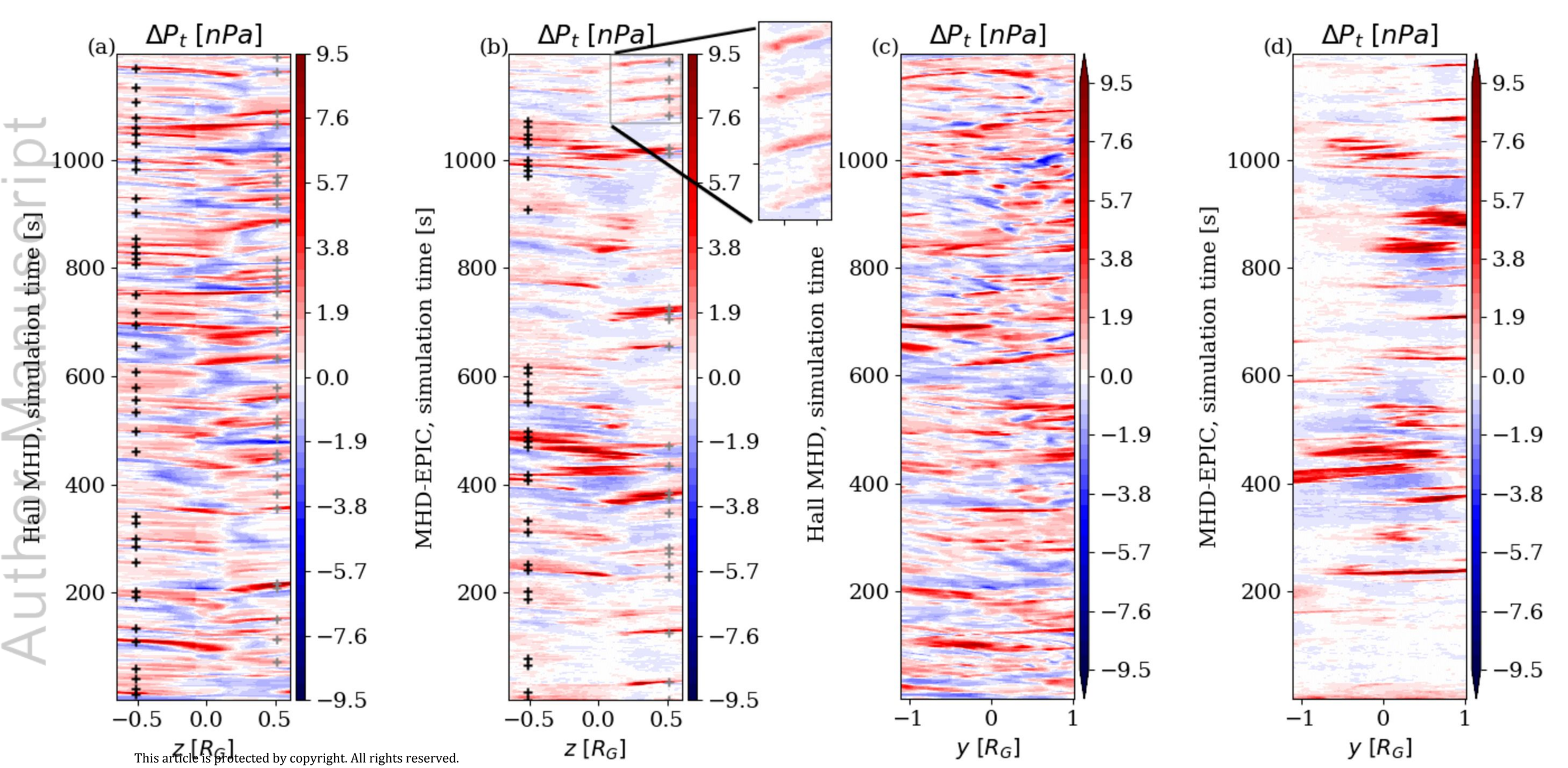

**Figure 7.**

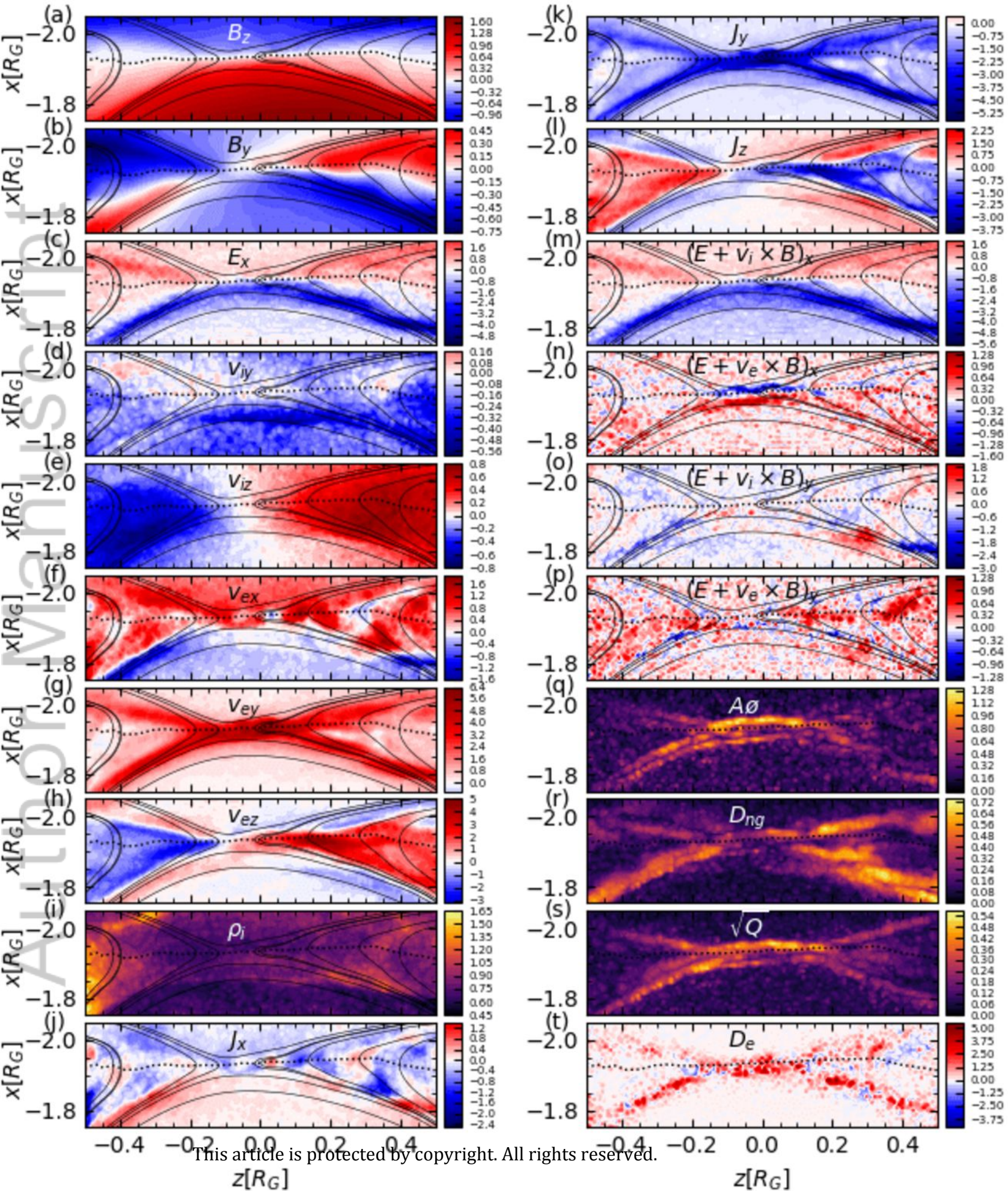

**Figure 8.**

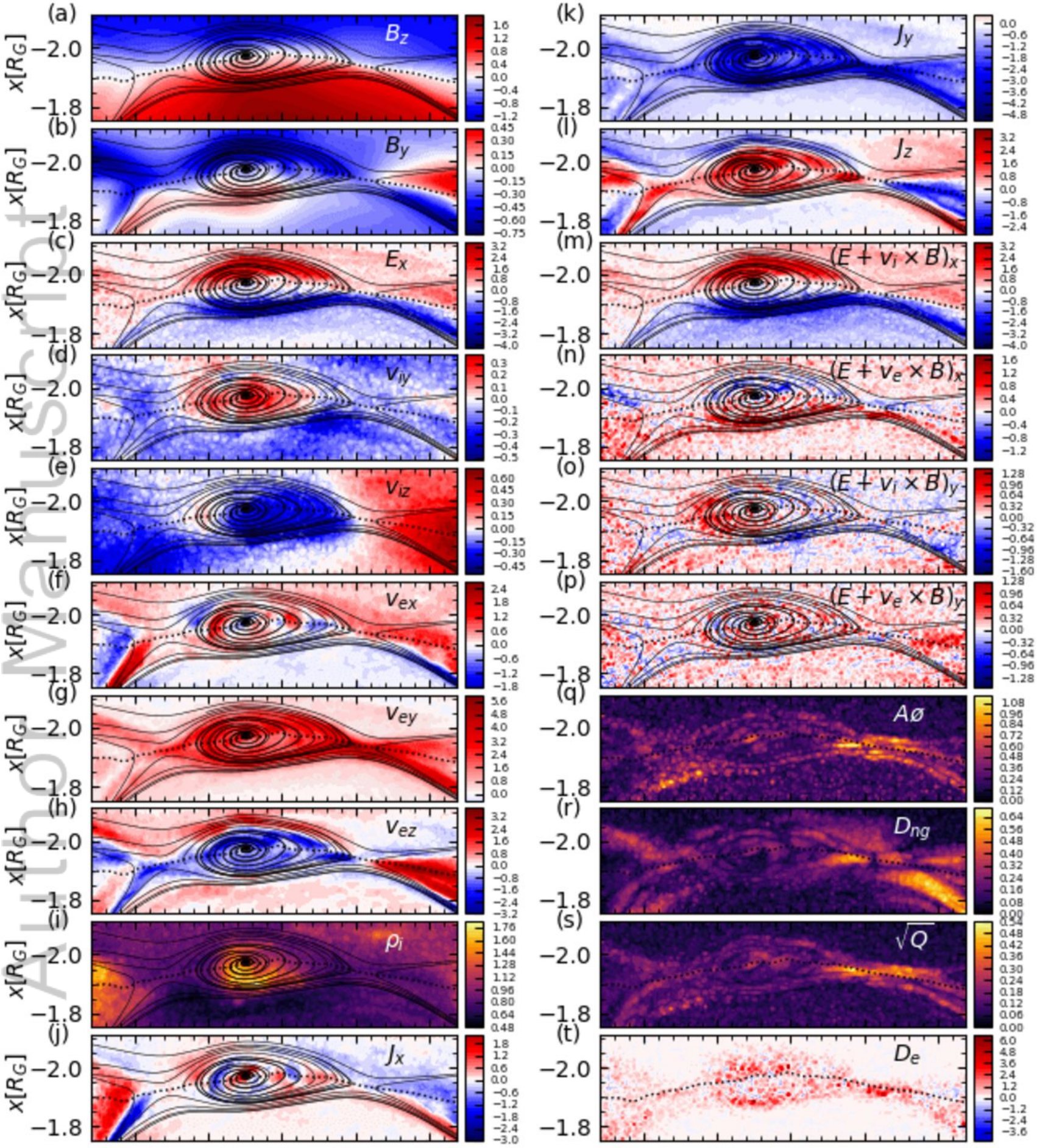

**Figure 9.**

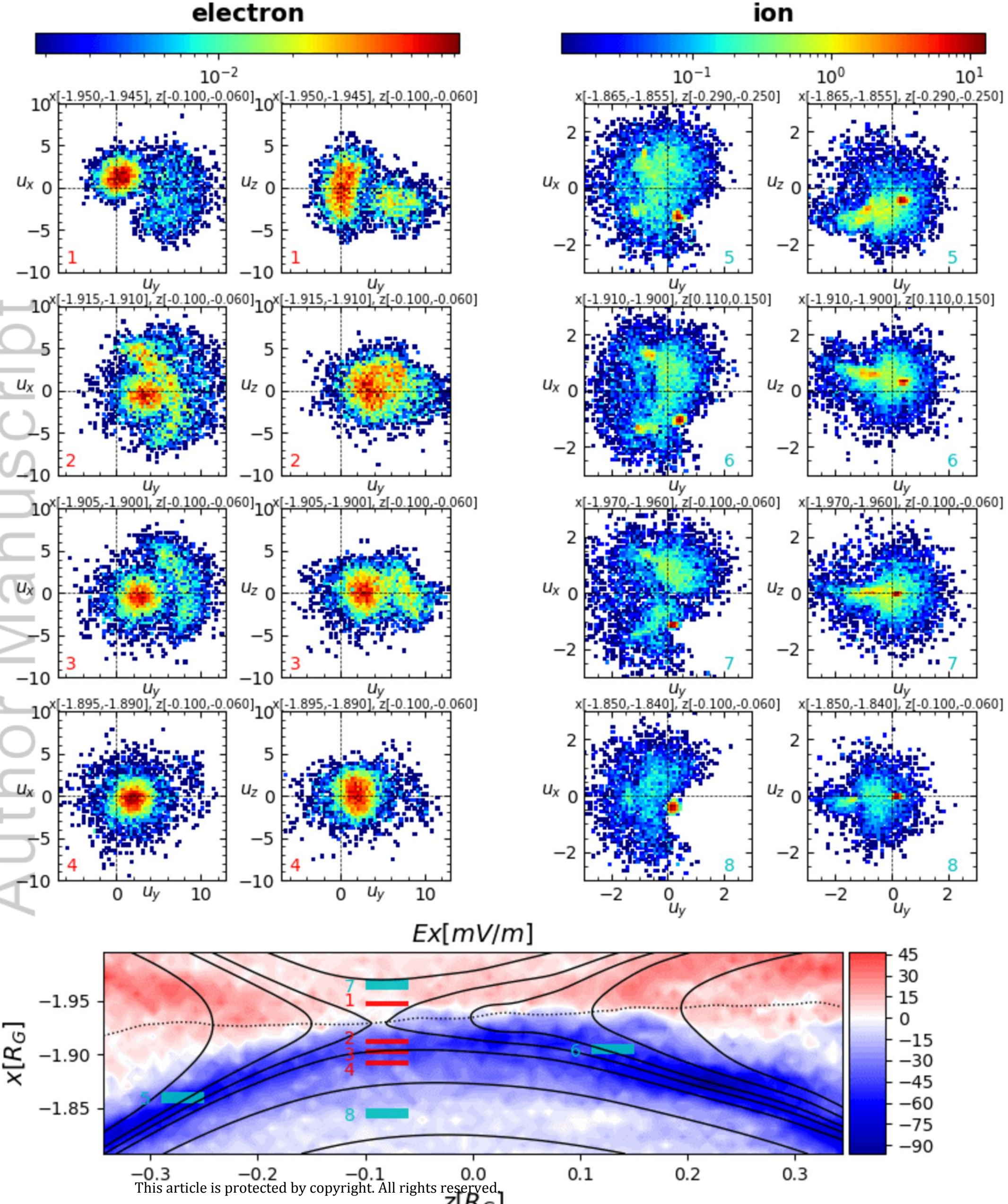

**Figure 10.**

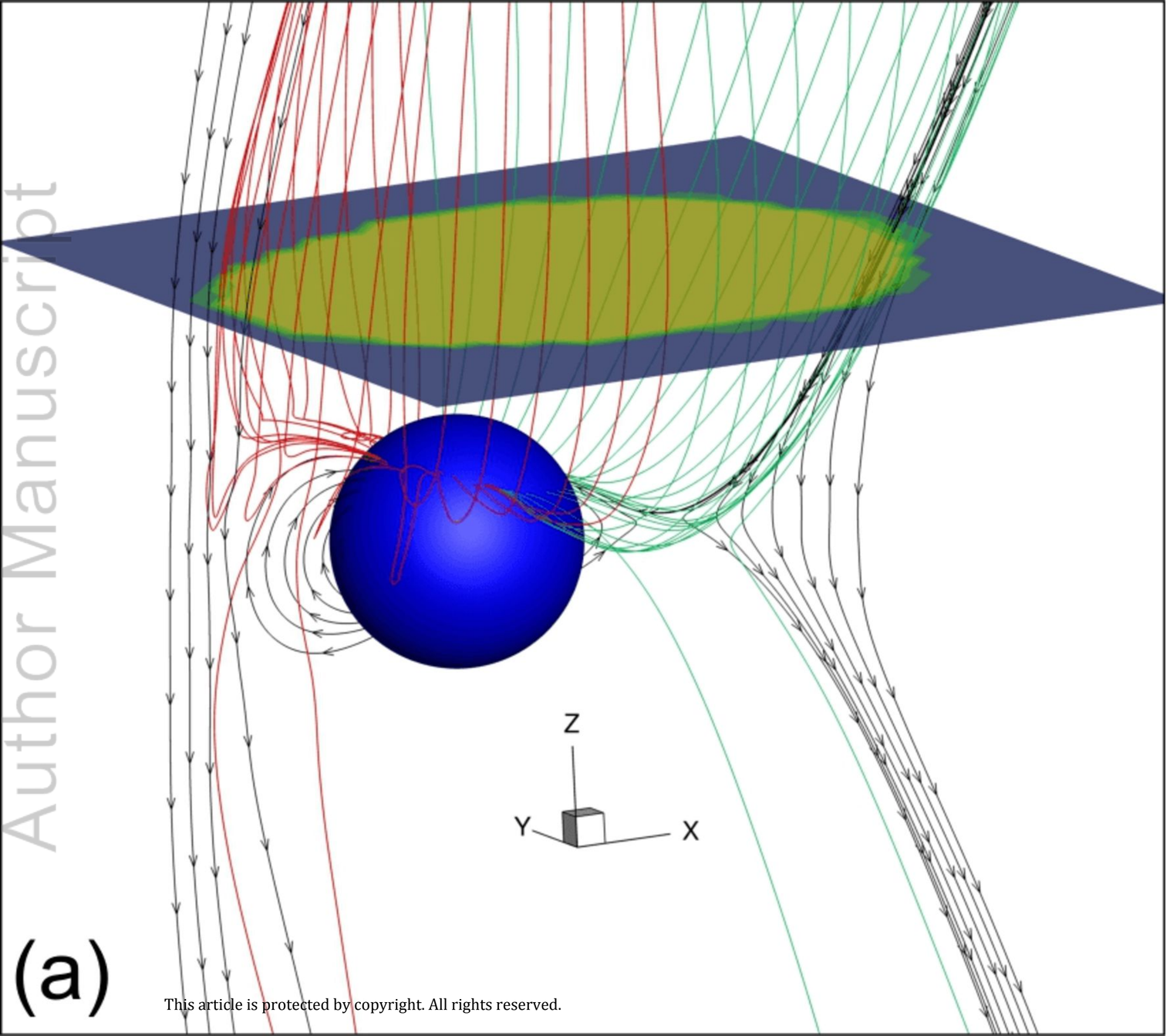


(a)

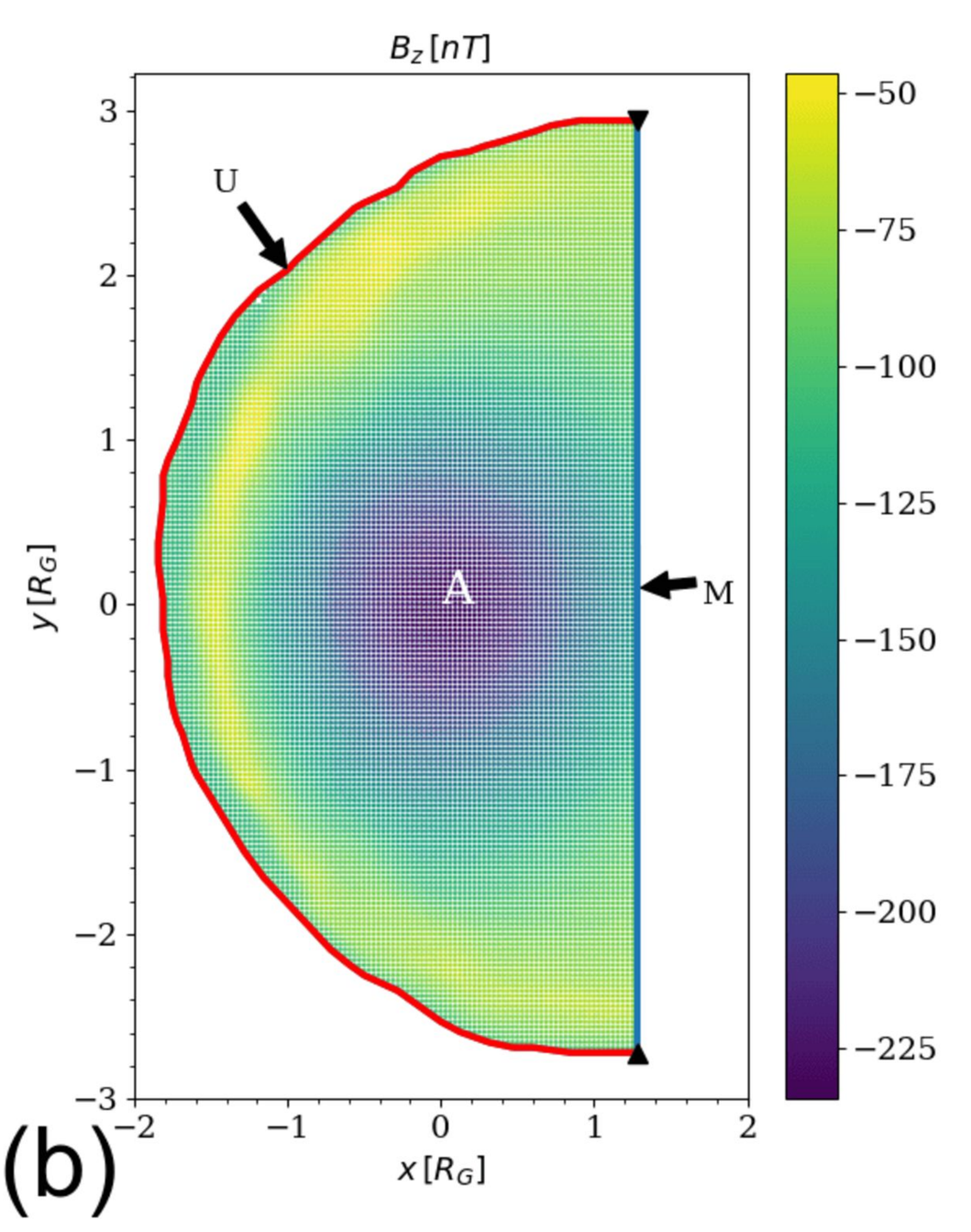


(b)

**Figure 11.**

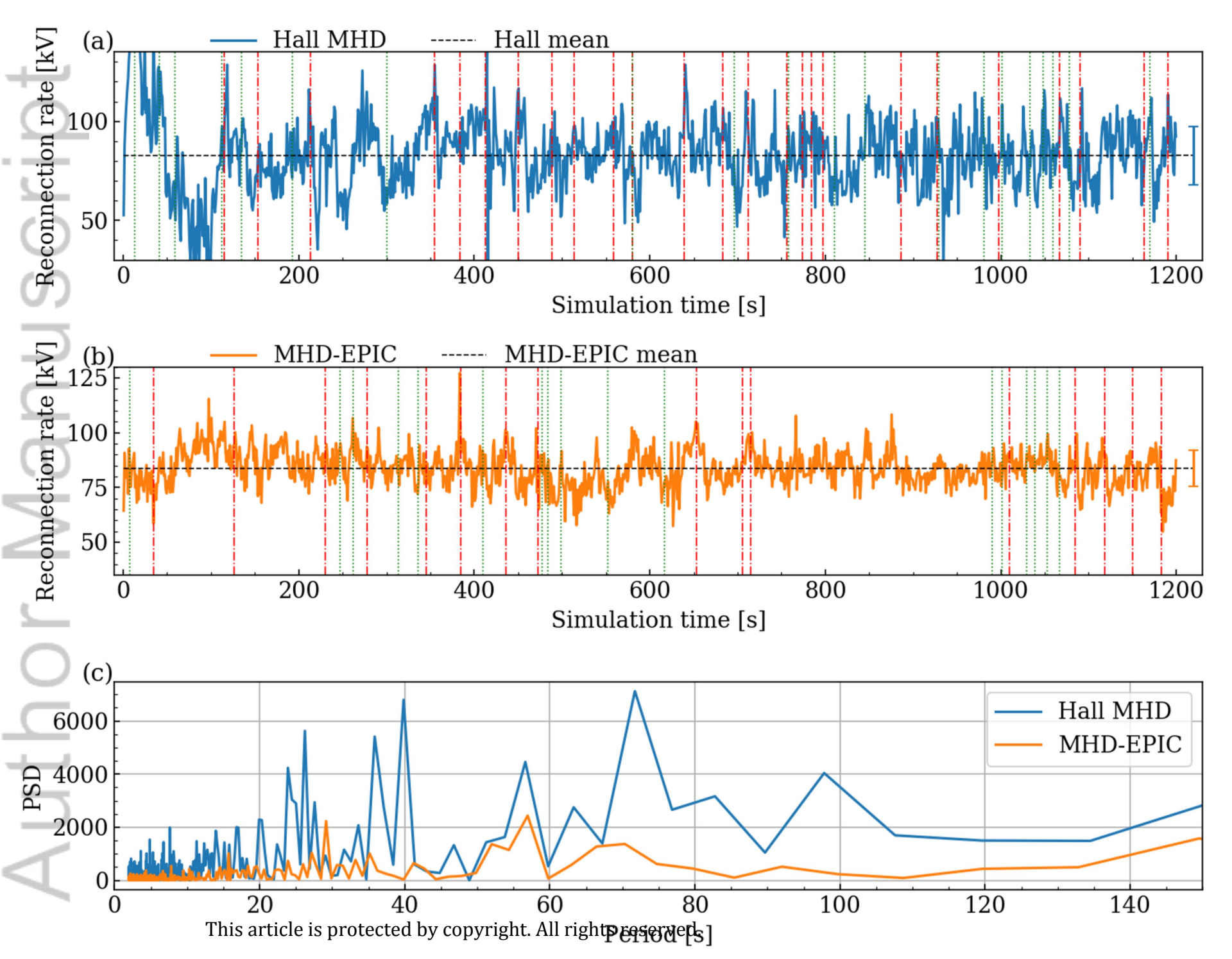

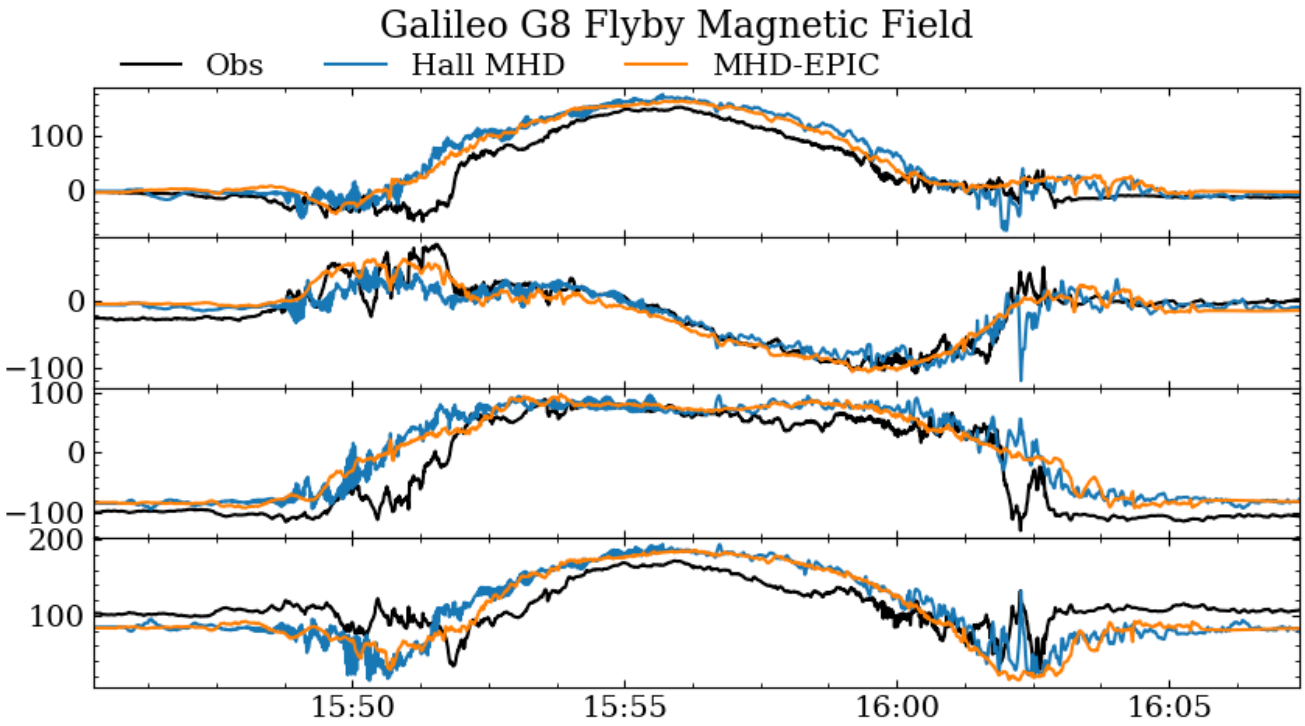


2020JA028162-f01-z-.png

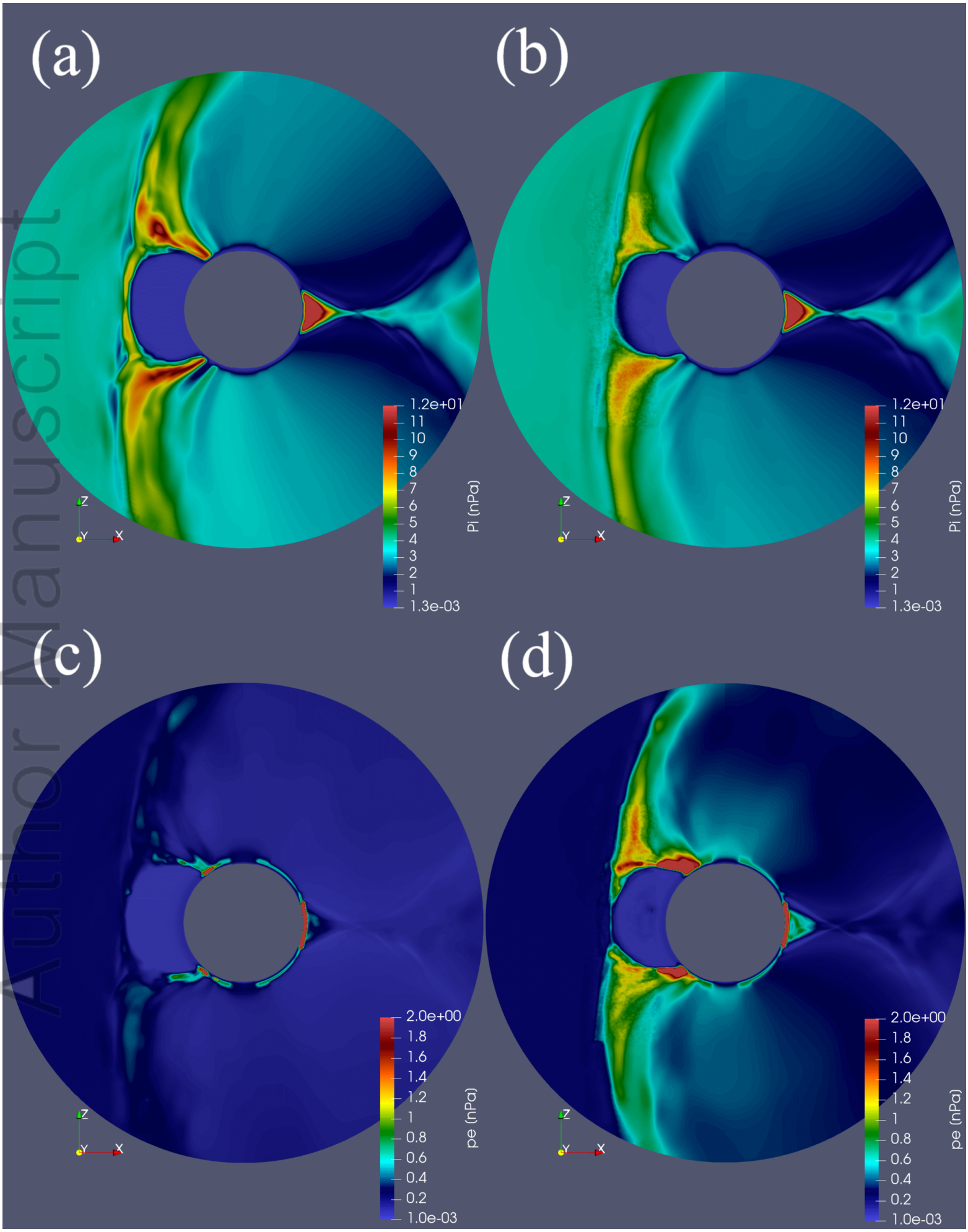




2020JA028162-f02-z-.png

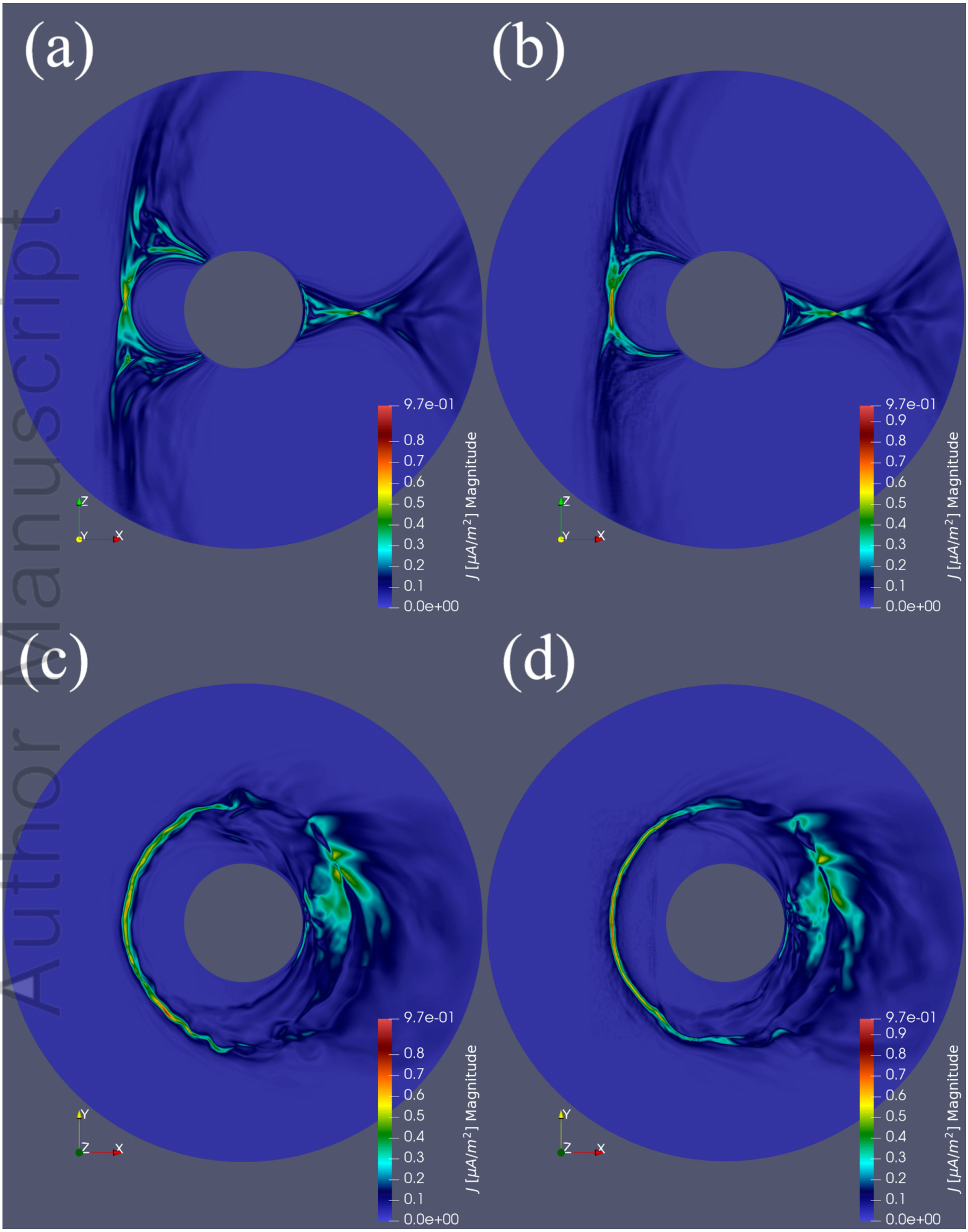




2020JA028162-f03-z-.png

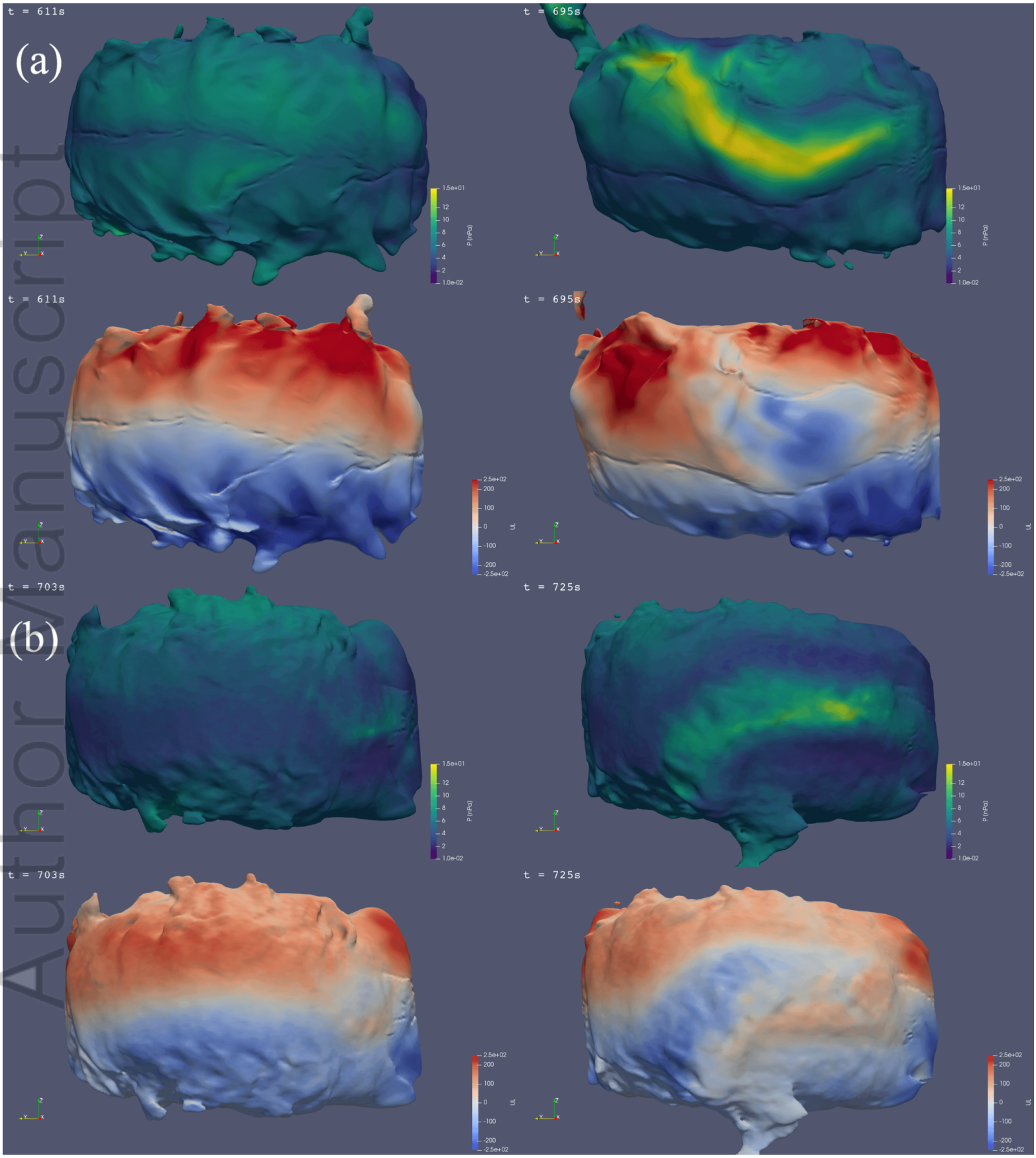


2020JA028162-f04-z-.png

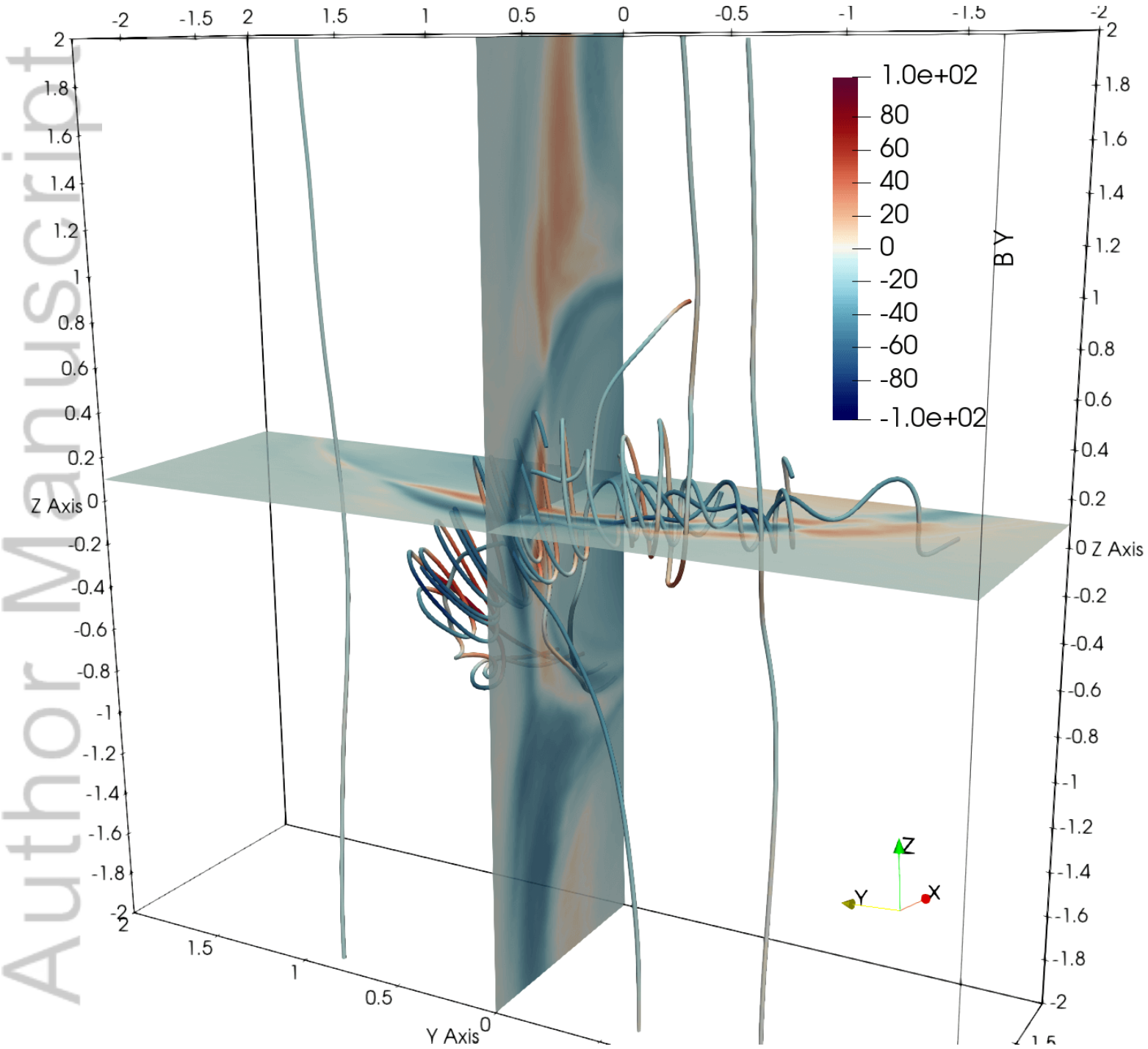


2020JA028162-f05-z-.png

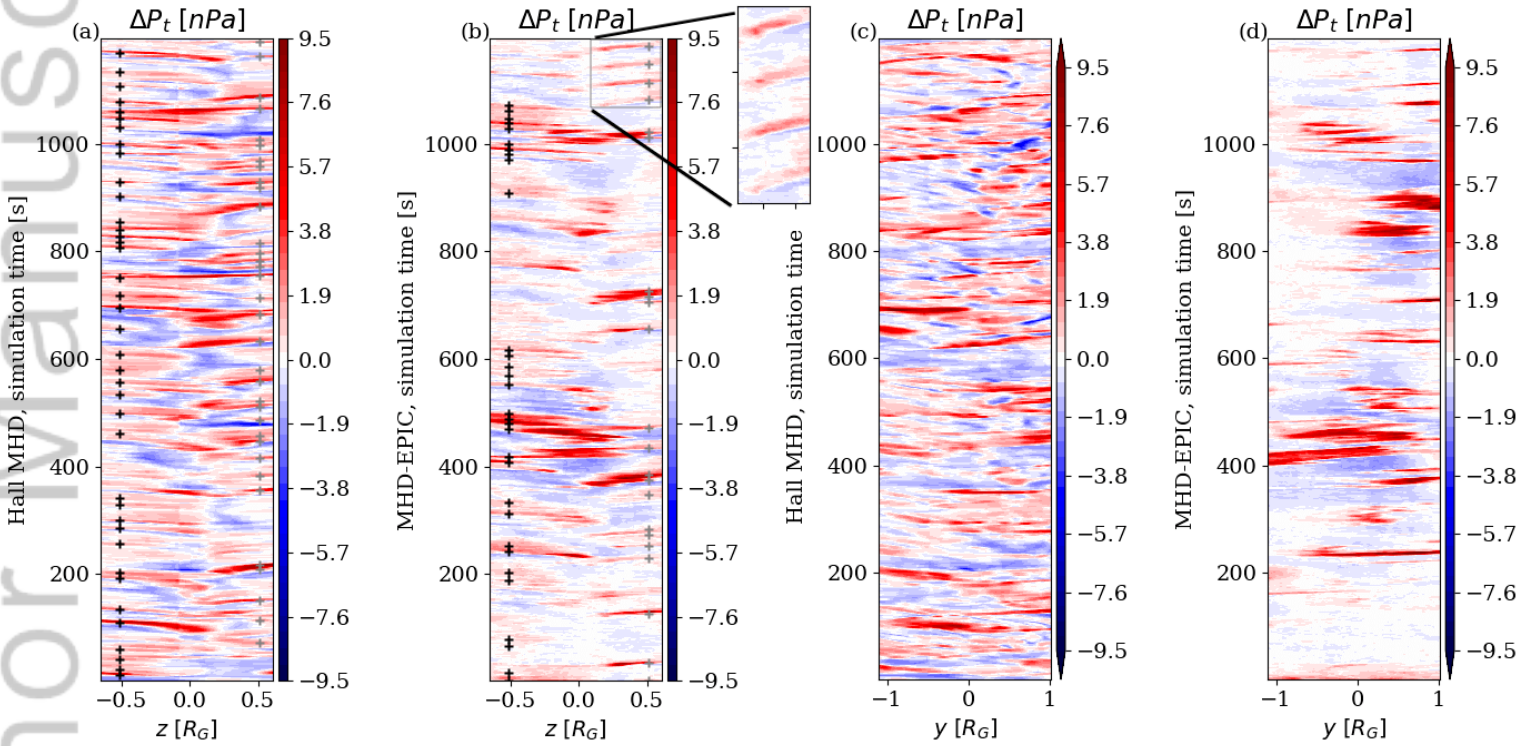


2020JA028162-f06-z-.png

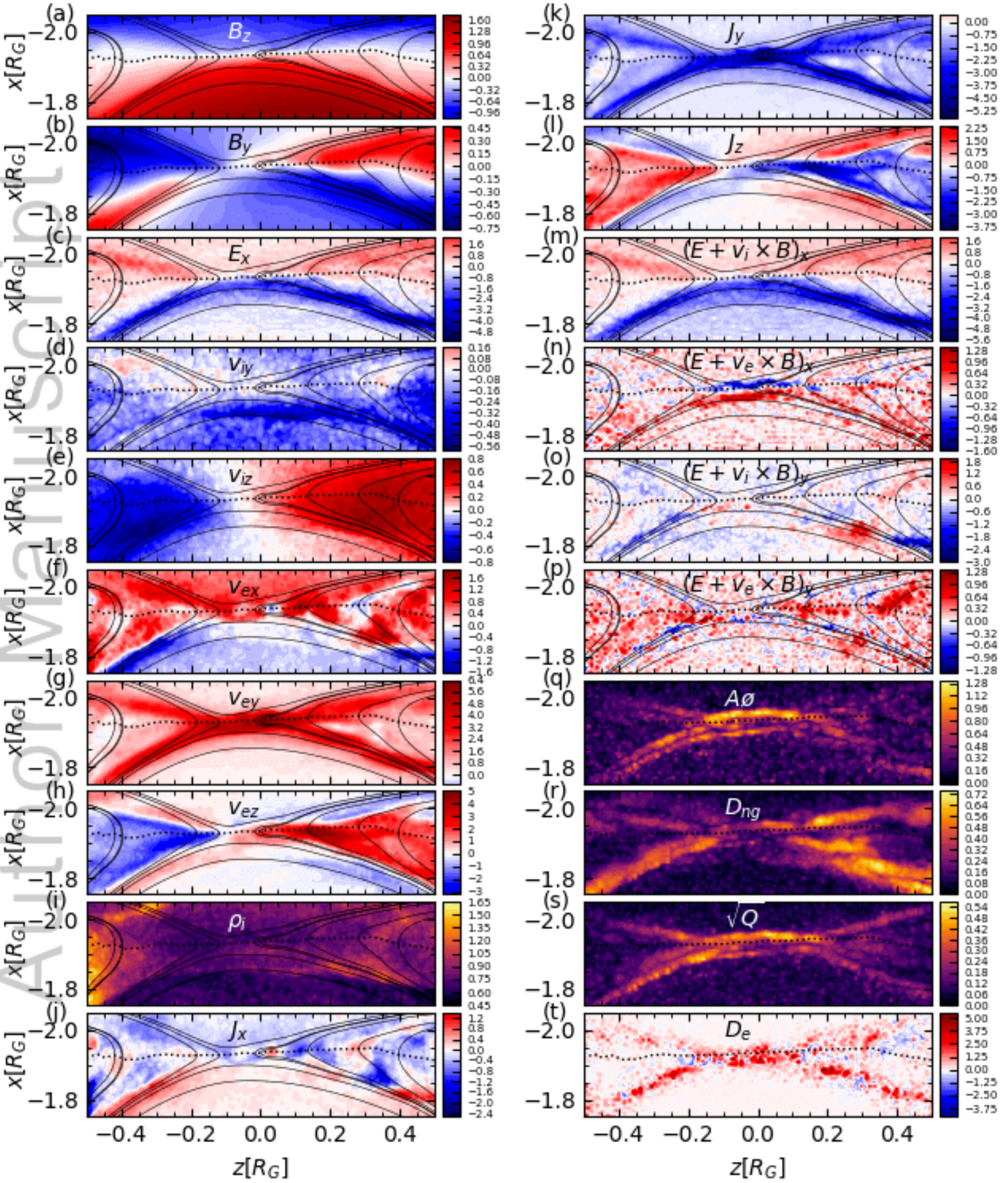


2020JA028162-f07-z-.png

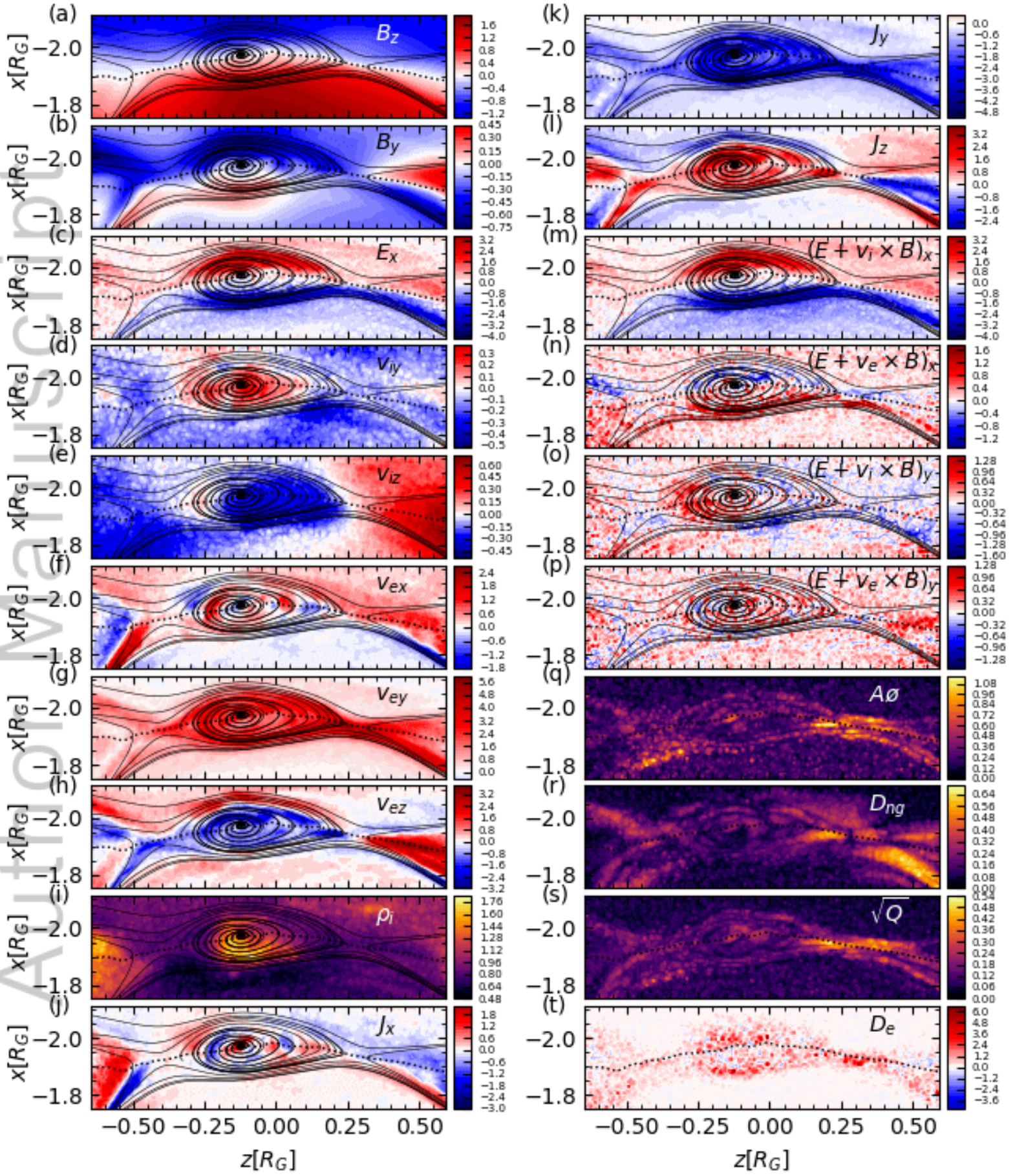


2020JA028162-f08-z-.png

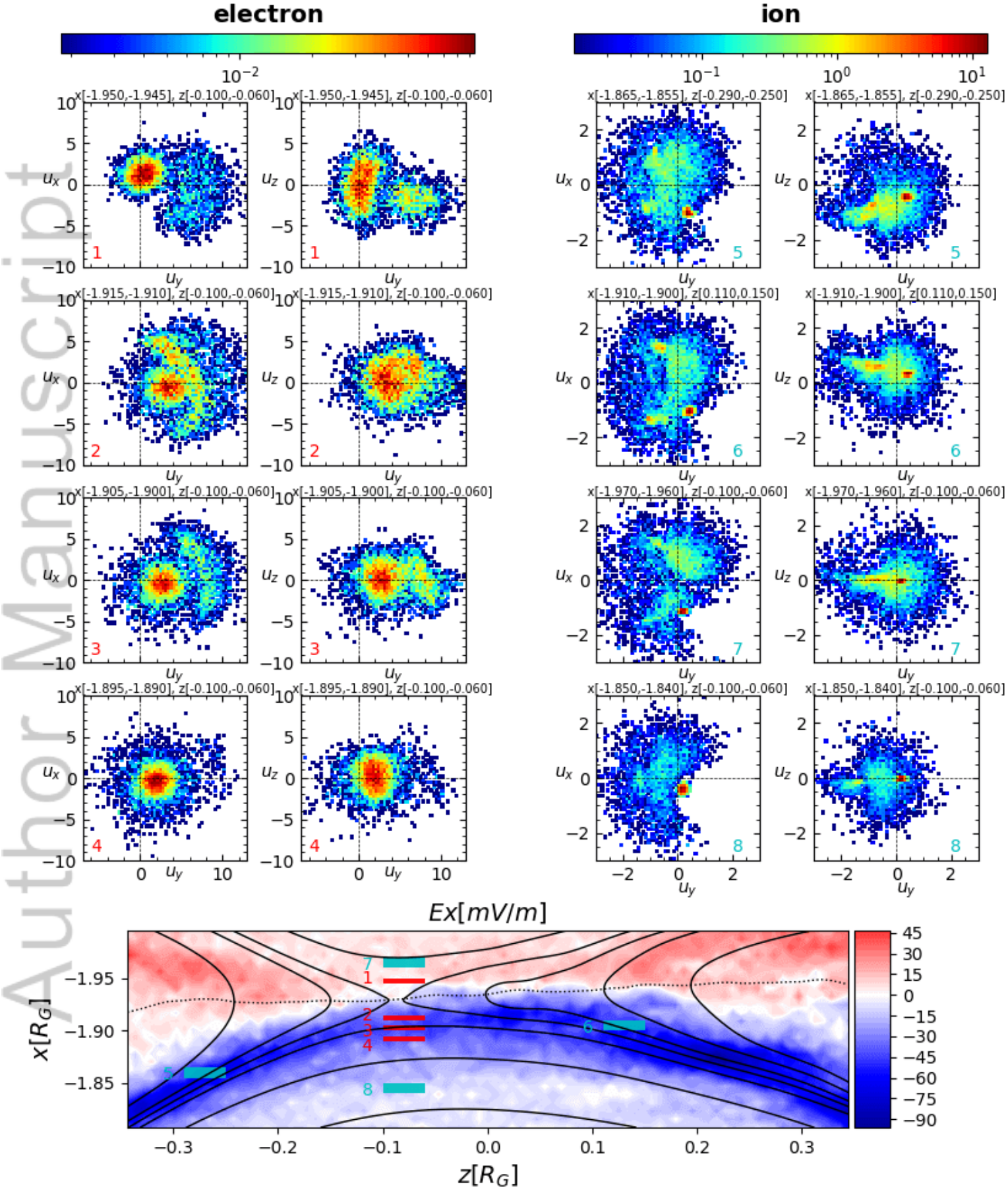





2020JA028162-f09-z-.png

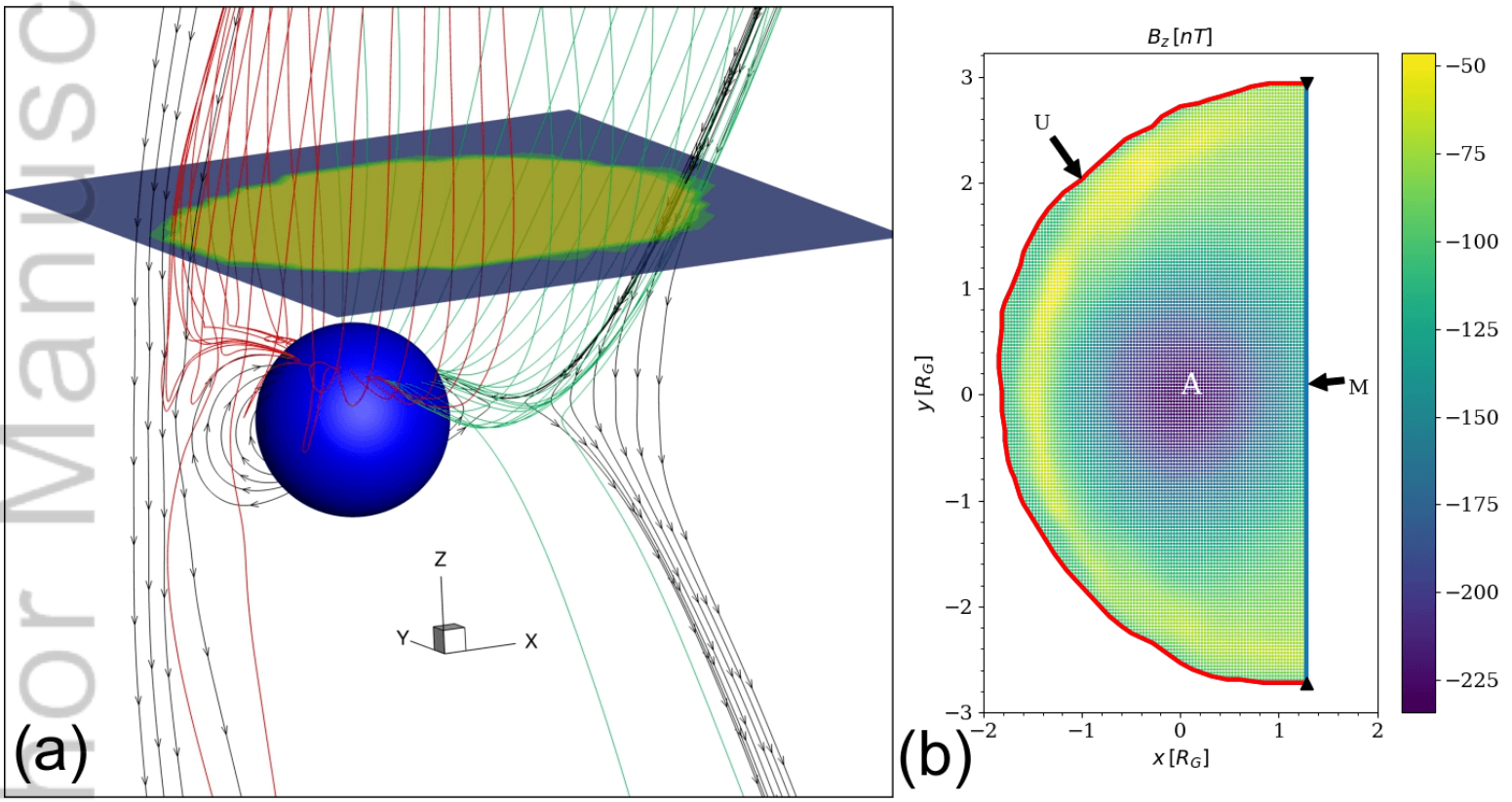


2020JA028162-f10-z-.png

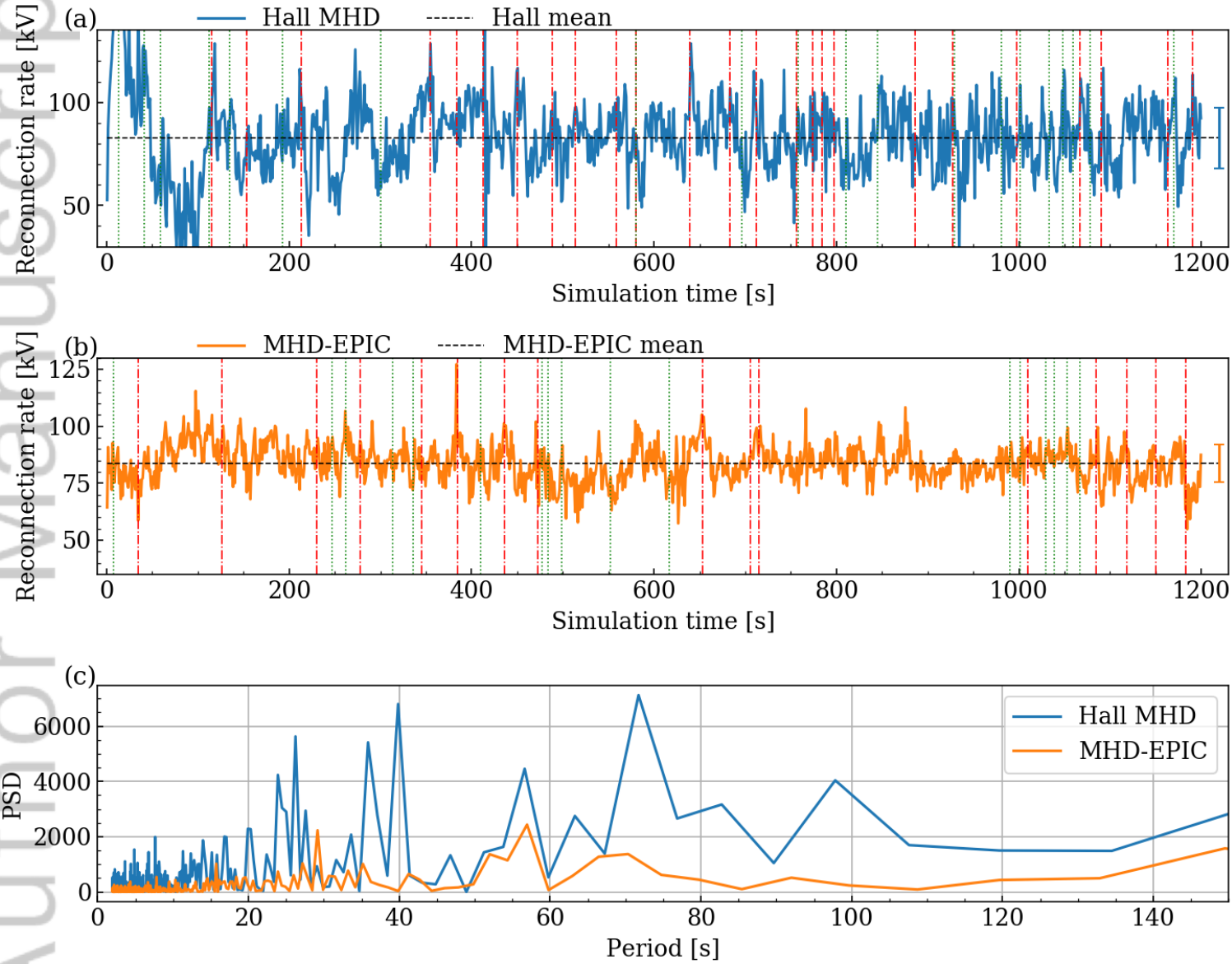


2020JA028162-f11-z-.png